



Inlet Design for a Propulsive Fuselage Concept

Exploring and evaluating geometrical inlet features based on a numerical approach

MSc Thesis
Ahmet Barış

Inlet Design for a Propulsive Fuselage Concept

Exploring and evaluating geometrical inlet features based on a numerical approach

by

Ahmet Barış

to obtain the degree of Master of Science
at the Delft University of Technology,
to be defended publicly on Tuesday April 30, 2023 at 12:30 PM.

Student number: 4877861

Thesis Committee	Dr. -Ing. A. Heidebrecht	Supervisor
	Dr. Ir. A.G. Rao	Chair
	Dr. Ir. A.H. van Zuijlen	Examiner

Date: Tuesday 16th April, 2024

An electronic version of this thesis is available at <http://repository.tudelft.nl/>.



Cover: *Aurora Flight Sciences by NASA* URL <https://www.kdcresource.com/insights/aurora-flight-sciences-wins-another-nasa-contract>

Preface

I would firstly like to thank and praise Allah (God), Lord of mankind, for giving me success in finishing this thesis and allowing me to complete my studies, and decreeing this outcome which I did not achieve on my own behalf. To Him (alone) we belong, and to Him (alone) we return. I would also like to thank my family, especially my father, for their support throughout my educational career. I cannot pay back what he did for me. I would of course also like to thank my supervisor Alexander Heidebrecht for his help during the project. The time and enthusiasm that he put into our meetings are much appreciated.

As I look back, I realize that I have learned a lot during this project. As always, adversities were countered but those define the learning points. Overall, I hope my contributions in- and outside of the APPU project are valuable. As you embark on reading this report, I hope you find it an interesting and engaging experience!

*Ahmet Barış
The Hague, April 2024*

Summary

The novel aircraft that is explored in this study is a propulsive fuselage concept, where boundary layer ingestion technology is implemented at an open rotor engine configuration mounted at the rear-fuselage. Boundary layer ingestion is a propulsion concept where the slow moving boundary layer of a body is ingested into a propulsive element and accelerated; this promises an increase in propulsive efficiency.

Recently, many boundary layer ingesting concepts have been explored in literature. However, its implementation on open rotor designs have been considered very limitedly. Furthermore, there is a lack of research dedicated into intake design for the engine core of such propulsion units. As such, the goal of this thesis is to design an intake to the engine core and thereby aerodynamically evaluate geometric parameters that impact the flow field. In that regard, it has been discussed that a submerged inlet would be the most suitable design choice. This objective promises more certainty into the feasibility of submerged intakes for rear-fuselage mounted boundary layer ingesting engines and assists in appropriately sizing relevant shape parameters to optimize the intake performance.

To obtain the thesis objective, a 3D CFD methodology has been employed. A multitude of geometries have been designed in CAD software, where the entrance thickness, duct shape (including, among others, intake length), lip shape, entrance azimuthal range and sidewall corner radius are varied and shaped and altered in accordance with the findings of the simulation results. The so-called rolling-ball method has been implemented to determine the cross-sectional area distribution at specified axial positions inside the duct. Total pressure recovery, drag coefficient and distortion coefficient have been mainly used as grading criteria to evaluate the designs with respect to each other. Furthermore, (shear) streamlines, Mach, pressure and wall shear contours are visualized as well.

The results of this thesis show that the total pressure recovery in all cases could not exceed 80% due to the low-energy content of the thick boundary layer, but losses, confined to the inside of the duct, of lower than 1% could be achieved.

The effects of the various shape parameters are as follows; the intake performance is heavily dependent on the entrance thickness. A trade-off has been encountered, where this parameter plays a significant role in the converging nature of the duct, the separation that takes place at the entrance and consequently the total pressure ingestion that takes place. Moreover, decreasing the azimuthal intake extent shows an increase in total pressure ingestion, but simultaneously an increase in curvatures inside the duct, leading to higher pressure losses. In that regard, a longer duct significantly reduces the strong curvatures and helps the flow to remain attached for longer, with only a small increase in viscous drag. Moreover, a smooth corner helps eliminate the vortex that forms at the corner of the sidewall. At sea-level static, the round corner displays a case of a large vortex, but this vortex helps the flow to orient towards the sidewall and decreases the distortion coefficient. Finally, the significance of lip shape is most evident at sea-level static conditions, where a circular lip with a radius 50 % larger than that of the standard NACA lip demonstrates optimal performance, in which case smooth continuity with the duct is crucial to eliminate the separation aft of the lip.

Furthermore, it has been shown that the axial area distribution plays an imperative role in shaping the duct, where particular attention must be paid on achieving full convergence. In this regard, the rolling-ball method proves to be a valuable approach for determining the area distribution.

Contents

Preface	i
Summary	ii
Nomenclature	viii
1 Introduction	1
2 Literature Review	3
2.1 Theoretical Background	3
2.1.1 The BLI Phenomenon	3
2.1.2 Inlet Design Considerations	4
2.1.3 Inlet Types	7
2.2 Research Motive	10
2.2.1 Research Gap	11
2.2.2 Research Question	12
3 Methodology	13
3.1 Geometry Creation	13
3.1.1 Description of Geometry	14
3.1.2 Geometry Definition	15
3.1.3 Overview of Geometries	16
3.1.4 Rolling-Ball Method	17
3.2 Mesh Generation	18
3.3 Simulation Set-up	20
3.3.1 Turbulence Modelling	21
3.3.2 Computational Domain and Boundary Conditions	21
3.4 Overview of Test Conditions	23
3.5 Performance Evaluation Metrics	23
4 Model Verification	25
4.1 Sources of Uncertainty	25
4.2 Grid Convergence Index	26
4.3 Comparative Analysis of Mesh Resolution	27
4.4 Alternative Differential Scheme	33
5 Results & Discussions	34
5.1 Overview of Quality Metrics	34
5.2 Area Distribution	36
5.3 Effect of Geometric Parameters	36
5.3.1 Entrance Thickness	37
5.3.2 Azimuthal Extent	39
5.3.3 Duct Shape	42
5.3.4 Corner Radius	44
5.3.5 Lip Shape	45
5.4 Geometry Definition	46
6 Conclusions & Recommendations	47
References	53
Appendices	54

A: Geometry	54
A.1 Geometry Close-up	54
A.2 Axial Development of Shape	56
A.3 Measurement of Engine Alignment	56
B: Mesh	57
B.1 Overview of Mesh	57
B.2 Mesh Comparison	58
B.3 Boundary Layer Assembly	59
C: Verification	61
C.1 Convergence	61
C.2 Extra Contours of Mesh Resolution Differences	62
C.3 Clarification of Error Estimation Method	62
C.4 GCI of Alternative Settings	63
D: Explanatory Figures	65
D.1 Propeller Surface	65
D.2 Sign Convention	65
D.3 Boundary Layer Thickness	66
D.4 Lip Shape	66
E: Supplementary Contours	67
E.1 Contours at Cruise	67
E.2 Contours at SLS	69

List of Figures

2.1	BLI working principle	4
2.2	A typical subsonic inlet with a representative stream tube at cruise condition	5
2.3	Comparison of a sharp and blunt lip	6
2.4	Contours of Mach number in the tailcone region.	6
2.5	Vortex roll-up at the ramp walls & geometry of the NACA inlet	7
2.6	Influence of flight conditions on the ram recovery ratio.	8
2.7	An example of a scoop inlet type	9
2.8	Comparison of inlet types on a canard type aircraft.	9
2.9	DisPURSAL BLI engine layout	10
2.10	Layout of the APPU tailcone	10
3.1	G1- and G2-continuity	14
3.2	Parametric model to design a submerged inlet entrance.	15
3.3	Definition of the half-annulus geometry	15
3.4	Overview of all geometries	16
3.5	Illustration of rolling-ball method.	18
3.6	Mesh topology around tailcone region.	19
3.7	Mesh around the sharp ramp corner.	20
3.8	Sketch of the computational CFD domain	21
3.9	Boundary conditions at the tailcone.	22
4.1	Scatter plot of y^+ -values	25
4.2	Illustration of mesh convergence	27
4.3	Difference between mesh iii and mesh i: C_f	28
4.4	Difference between mesh iii and mesh i: $C_{p,t}$	29
4.5	Difference between mesh iii and mesh i: Mach number	29
4.6	Error estimation method for $C_{p,t}$ applied at the compressor face	32
4.7	Error estimation method for C_f applied at the tailcone region	32
4.8	Mach contours for the two types of solver settings	33
5.1	Overview of σ	34
5.2	Overview of C_D	35
5.3	Overview of DC60	35
5.4	Area distribution graph	36
5.5	Effect of D : symmetry plane	37
5.6	Effect of D : 3D view	38
5.7	Effect of θ : symmetry plane	39
5.8	Effect of θ : inner surface	40
5.9	Effect of θ : outer surface	40
5.10	Effect of θ : $C_{p,t}$ at compressor	41
5.11	Effect of θ : propeller plane	41
5.12	Effect of duct shape: view I	42
5.13	Effect of duct shape: view II	42
5.14	Effect of duct shape: $C_{p,t}$ at compressor	43
5.15	Effect of duct shape: non-axial flow at compressor	44
5.16	Effect of C :cruise	44
5.17	Effect of C : SLS	45
5.18	Effect of lip shape: SLS	46

A.1	Close-up view on geometries	55
A.2	Axial development of duct towards compressor face	56
A.3	Estimation of engine alignment h	56
B.1	Mesh of the entire domain	57
B.2	Mesh of the tailcone region	57
B.3	Surface mesh comparison FA & HA	58
B.4	Mesh comparison at compressor face	59
B.5	BL mesh of FA & nozzle mesh topology	59
B.6	BL mesh of HA	60
C.1	Plot of residuals	61
C.2	Standard deviation of P_t (a) and C_D (b) at the compressor surface.	61
C.3	ΔM at the wake of the vertical tail plane	62
C.4	ΔC_f the nozzle region between fine and coarse mesh	63
C.5	Close-up view of $\Delta C_{p,t}$ at outer edge of the compressor	63
C.6	Mesh convergence plots for alternative solver settings	64
D.1	Propeller surface definition	65
D.2	Sign convention	65
D.3	Boundary layer edge	66
D.4	Curvature combs of the various lips	66
E.1	Effect of D : $C_{p,t}$ profile	67
E.2	Effect of vertical tail: streamlines	68
E.3	Effect of C : vortex formation at corner (cruise)	68
E.4	Effect of C : vortex formation at corner view II (cruise)	69
E.5	Effect of C : vortex formation at corner(SLS)	69
E.6	Effect of θ : P_t ingestion	70
E.7	Effect of θ :Mach	70
E.8	Effect of duct shape (SLS): view I	71
E.9	Effect of duct shape (SLS): view II	71
E.10	$C_{p,t}$ at compressor plane (SLS)	71

List of Tables

3.1	Overview of all designs	17
3.2	Simulation test conditions	23
3.3	Evaluation Metrics	23
4.1	Overview of grid refinement study	26
4.2	results of grid refinement study	27
4.3	Estimation of error	31
5.1	Performance metrics for FA-V1 and FA-V2	36
C.1	results of convergence study for alternative solver settings	64
C.2	Comparison of $P_{T,gauge}$ data between the different solver settings	64

Nomenclature

Abbreviations

Abbreviation	Definition
AR	Aspect Ratio
BL	Boundary Layer
FA	Full Annulus
HA	Half Annulus
MFR	Mass Flow Ratio
SLS	Sea Level Static

Subscripts

Subscript	Definition
∞	ambient
<i>cor</i>	corrected
<i>d</i>	duct
<i>E</i>	Entrance
<i>in</i>	domain inlet
<i>out</i>	domain outlet
<i>p</i>	propeller
<i>pres</i>	pressure
<i>t</i>	total
<i>visc</i>	viscous
<i>x</i>	axial direction

Symbols

Symbol	Definition	Unit
<i>C</i>	sidewall corner radius	[mm]
<i>D</i>	Entrance thickness	[mm]
<i>h</i>	fraction of duct aligned with engine	[mm]
<i>L</i>	Intake length	[mm]
<i>R</i>	Lip radius	[mm]
θ	Azimuthal angle	[°]
<i>A</i>	Area	[m ²]
<i>C_D</i>	Drag coefficient	[kg/s]
<i>C_f</i>	Skin friction coefficient	[-]
<i>C_p</i>	Pressure coefficient	[-]
<i>DC60</i>	Distortion coefficient	[-]
\dot{m}	Mass flow rate	[kg/s]
<i>M</i>	Mach number	[-]
<i>p</i>	Pressure	[Pa]
<i>Re</i>	Reynolds number	[-]
<i>v</i>	Velocity	[m/s]
<i>V_{planar}</i>	Planar velocity component	[-]
<i>y⁺</i>	First wall distance	[-]
δ	Boundary layer thickness	[m]
ρ	Density	[kg/m ³]
σ	Total pressure recovery	[%]
τ	Wall shear stress	[Pa]
ϕ	Field variable	varying

Introduction

The aviation industry is responsible for an important mode of transport that connects people across continents and has surpassed the growth rate of any other industry. Airbus predicts that demand for passenger flights will increase by 3.6% annually over the next 20 years [1].

Consequently, the design of fuel-efficient aircraft has been the largest concern in recent years. As a result, much research is aimed at designing novel aircraft concepts as realizing significant changes within the current design is hardly possible without considering a remarkably different model. Although electric technology has proven to be very successful in the automotive industry, with the current state-of-the-art technology, many complications arise with its application in the aviation industry, such as the low energy density property of onboard batteries. Hence, a short-term solution in this direction is difficult to achieve [2]. In that regard, the **Advanced Propulsion and Power Unit (APPU)** project comes in useful, as it builds a promising concept that can comply with the relatively short-term EU Flight Path 2050 Goals. This project focuses on modifications solely aimed at the APU (Auxiliary Power Unit) of the already existing Airbus A321neo: the APU is replaced with the APPU. This APPU is a highly relevant innovation in the academic industry, as it combines the use of an open rotor engine design with a technology called boundary layer ingestion (BLI). In conjunction, they promise a more energy-efficient aircraft. These favourable improvements along with proportionally small modifications required make the APPU project highly relevant to explore.

The open-rotor engine configuration is an uncommon design choice as the bulk of all passenger aircraft employ turbofans. Besides, little to no examples of BLI implementations on open rotor designs are available in literature, since most evaluated concepts use turbofans or turbo-electric fans. For this reason, it is expected that the APPU will greatly contribute to providing information on the feasibility of this limitedly explored design choice.

Though the aim is to reach the market by 2035, the APPU project is currently in the preliminary design stage and faces various challenges, including the design of the aft-fuselage mounted engine inlet. Currently, the inlet of the engine core remains unmodeled. The intake plays a crucial role in providing high quality flow to the compressor, in turn affecting the engine cycle efficiency: a 1% pressure loss in the intake causes a 2 % reduction in power ¹. On top of that, the air intake has a significant impact on the surge margin, operability and performance of the engine core. Besides, the intake affects the downstream located propeller, and depending on the inlet geometry, either adversely or positively affects this airframe component.

Therefore, it is imperative to design a suitable inlet and critically analyze the flow field around the inlet to investigate the impact of the APPU on the aerodynamic performance of the aircraft. Iterating towards the 'perfect solution' however, is considered beyond the scope; an optimization study is not performed in this thesis. Alternatively, the objective of this study is to: **Design an inlet for the BLI open rotor engine of the APPU and evaluate key inlet shape parameters that affect the aerodynamic performance of the aircraft.**

Modelling an inlet and aerodynamically assessing differently shaped inlets will bring about important conclusions that will provide a building block for drawing an inlet that is located in similar surroundings, i.e. for aft-fuselage mounted intakes. Altogether, it allows for a proper investigation of the benefits of BLI, which along with data on the propeller, provides more reliability into the propulsive efficiency. This, in turn, provides soundness for research into other components of the APPU aircraft that require accurate input for the propulsive efficiency. Furthermore, it will significantly contribute to providing more academic knowledge about BLI implementation on an open-rotor engine and whether this is a favourable design option for future BLI concepts.

This report is organized as follows. Chapter 2 presents a background on the subject of BLI and a recap of the literature review, finishing with the research motive of this project. The methodology that is employed in this thesis is explained in detail in Chapter 3. Then, Chapter 4 presents a verification study. Afterwards, the findings of this thesis are elaborated upon in Chapter 5 and include a technical discussion. At last, main conclusions and future recommendations are provided in Chapter 6.

¹Rao, A. G., & Yin, F. (2021, July). The APPU Engine Preliminary Design [Slide show; PowerPoint Presentation].

2

Literature Review

This chapter is divided into two sections. The first section provides summarized findings of the literature research that was conducted at the start of the thesis. Then, based on the findings of the literature study, the research motive is provided in the second section. First, the research gap and afterwards, the goal of this research is presented accordingly in the form of a research question.

2.1. Theoretical Background

In this section the BLI concept is explained, inlet design considerations are elaborated on and lastly different inlet types as found in practice are presented.

2.1.1. The BLI Phenomenon

The A321 APPU utilizes an interesting and promising concept which emerged especially in later years called wake filling, often referred to as BLI. BLI is a propulsion concept where the slow moving boundary layer (BL) of a body is ingested into a propulsive element and accelerated as compared to the conventional way of passing into wakes [3].

The most prominent effect of BLI on aerodynamic performance can be explained by considering Figure 2.1. In a conventional engine configuration, the engine provides a momentum excess that must equal the momentum deficit of the body wake of the aircraft caused by viscosity. As can be seen from the top sketch, a large velocity deficit is realized. The propulsive efficiency loss is caused by kinetic energy left in the wake, which can be characterized by non-uniformities in the flow. These non-uniformities in the velocity profile result in fluid friction and therefore dissipation of energy. BLI reduces these non-uniformities by filling the wake. When considering an ideal BLI model, the wake is accelerated using the propulsive unit up to freestream velocity, such that the velocity profile is uniform. In that case, no losses due to dissipation occur. In practice, the wake is not perfectly filled, but the momentum excess is reduced nevertheless allowing for an efficiency increase [4].

Due to the fuselage being the largest contributor to wetted area on an aircraft, it is considered the most attractive region to apply the wake filling concept. The propulsor is then attempted to be placed more aft to benefit from more wake filling [5].

Due to a less obvious distinction between thrust and drag, it is more useful to consider the power balance method, where a kinetic energy equation is set up instead [6]. From this point of view, the effect of BLI can be explained from the perspective that the propeller reduces the kinetic energy of the wake flow, thereby reducing the power required to generate an equivalent thrust at the same flight condition [7]. This leads to a reduction in fuel consumption.

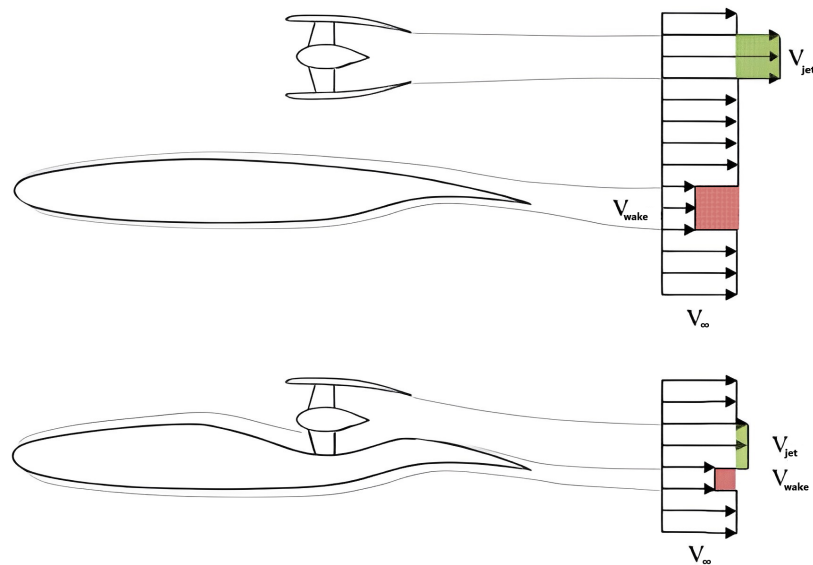


Figure 2.1: BLI working principle [4].

2.1.2. Inlet Design Considerations

An inlet has many functions, but the following three main functions may be recognized:

1. Provide an adequate amount of **uniform flow**. Distortion, characterized by varying distributions of total pressure, temperature and velocity, ought to be minimal. Distortion has an adverse effect on a stable compression, making it more susceptible to stall or surge. In case of stall, a total loss of thrust occurs which is even more dangerous [8].
2. Next, the inlet must **diffuse**¹ the flow. The velocity of the air must be slowed down for the fan to have an acceptable amount of flow at which no separation occurs at the blades [9]. This diffusion must happen with a **high total pressure recovery**, defined as the average total pressure at the compressor divided by the total pressure at free stream as presented in Equation 2.1.

$$\eta_i = \text{inlet efficiency} = \frac{p_{t,2}}{p_{t,1}} \quad (2.1)$$

These losses are associated with either BLs or flow separation. Although shocks also reduce the total pressure recovery, for subsonic flights these are disregarded [8, 10]. Sometimes the term 'ram recovery' is mentioned instead (mainly in reports published by NACA), which is defined as the ratio of dynamic pressures.

For under-wing podded engines, it is also common practice for a large portion of the diffusion to take place upstream of the inlet. Was it not for the former inlet function, the diffusion could take place completely externally and the need for a nacelle would be removed. The presence of a nacelle or cowling then brings another key design consideration into play:

3. Lastly, an efficient **design for the external inlet geometry** should be facilitated. Although this term is not directly caused by the intake itself, the key point is that drag should be minimized. Whilst it could be opted to increase the cross-sectional area of the intake such that most diffusion takes place externally as pointed out in the previous point, this would increase weight & drag and increase the turning angles at low thrust settings. On the other hand, it could be opted for a thin inlet, where (almost) no diffusion takes place externally. But, that would imply that the inlet must be excessively long in order to diffuse internally, since the flow would approach the throat at higher speeds. Furthermore, this would result in separation at the inner side of the lip at take-off. Instead, as visible in Figure 2.2, in practice it is a combination of both; the nacelle is well aligned with the stream tube such that the drag is minimal. With this design, part of the diffusion is internal and the other part is external, in order to not fall into the extremes of either

¹Considering a conventional intake

end. Another point of view is to consider 'spillage' drag. Spillage drag occurs when air is spilled around an inlet instead of passing through the compressor. As the inlet is designed to suck in the maximum airflow possible, i.e. designed for the highest throttle setting or mass flow rate, in all other flight conditions the actual mass flow is not equal to this maximum airflow. The difference is then spilled towards the exterior of the lip. A lower mass flow rate would result in an increased local incidence angle at the lip, but a thicker lip would facilitate turning of the flow.

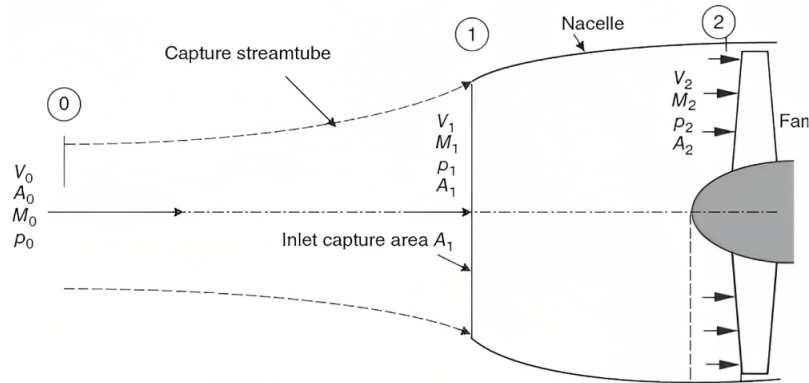


Figure 2.2: A typical subsonic inlet with a representative stream tube at cruise condition showing both internal and external diffusion [10].

Based on the provided design functions, the following points play a key role in designing an inlet:

- **Length of the inlet duct.** A longer duct results in a more developed and thicker BL. On the other hand, the flow has more space to develop a uniform profile, so there is a trade-off [11]. In case of the APPU, not much room is available as a considerable amount of space is reserved for the storage tank².
- **Inlet capture ratio:** the ratio of the area at the exterior of the inlet to the area at the lip of the inlet, see Figure 2.2. Also called the Mass Flow Ratio (MFR) or velocity ratio, this parameter incorporates the diffusion that takes place externally and describes the amount of mass flow captured. The MFR is dependent on the flight speed. At low speed, the MFR is high. At cruise conditions, the MFR is low because of a slim stream tube [12]. Besides, the MFR is a function of throttle setting; a low throttle setting corresponds to a low MFR and vice versa.
- **Lip contraction ratio.** This is defined as the ratio between the highlight, which is the tip of the intake lip, and the throat of the lip. The throat Mach number, M_{th} , is fixed at a maximum value of $M \approx 0.75$, since flow accelerates at the inlet lip and M_{max} should be less than one [10]. A large inlet contraction ratio, resulting in a blunt lip, can accommodate for high angles of attack and side slip angles without separation. At high-speed flight however, a blunt lip is not desired as extensive acceleration at the external cowl lip takes place, which creates sonic regions and causes shock formation. On the other hand, a low contraction ratio (sharp) inlet lip performs worse at low speed due to distortion towards the engine face but at the same time performs well at high speed owing to a low nacelle external drag. As a general remark, a too bunt lip increases the surface area which adds to the drag. Figure 2.3 graphically displays the discussion above.

²A layout of the APPU tailcone will follow later

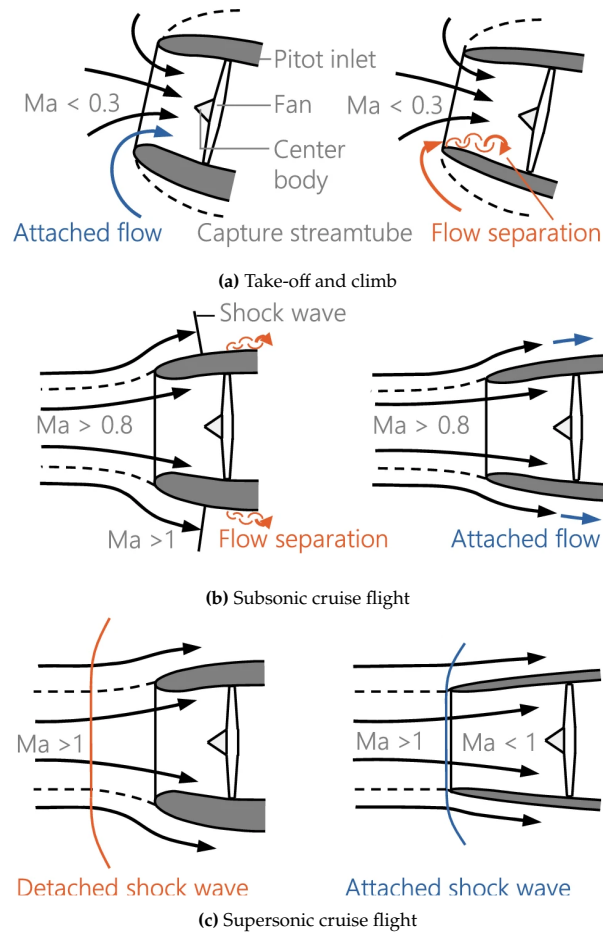


Figure 2.3: Comparison of a sharp and blunt lip at different flight conditions [13]. It should be noted that at subsonic cruise at lower thrust settings, Figure 2.3b does not hold. Rather, in that case the stream tube is more slim and the sharp lip will perform worse due to flow separation, as opposed to the blunt lip that allows for attachment at higher local incidence angles.

It becomes apparent from the discussions that to cope with a low MFR either the inlet cross-sectional area may be reduced or the lip contraction ratio may be increased, resulting in a short inlet with large maximum diameter. Regarding design for high-transonic flight however, a low contraction ratio with a slender nacelle design is favored to minimize the wave drag. This signifies an important trade-off in inlet design.

Lastly, The inlet design of the APPU is unlike the conventional inlet design of under-wing podded engines. There are some additional design considerations:

Duct shape Since the core of the engine is positioned at the center line of the fuselage and air must be drawn in from (above) the surface of the fuselage, the use of a curved duct is unavoidable. In a classical S-shape design, the flow inside the duct gets distorted as a result of the formation of a big vortex pair at the second bend of the duct. This vortex pair is formed since the low momentum BL easily separates as a result of an adverse pressure gradient and forms a region of recirculation. The flow in the upper part of the S-duct accelerates and causes a low static pressure due to a favorable pressure gradient. This lifts the low momentum BL air which causes the formation of a vortex pair, which in turn causes distortion and vibrations leading to fan blade stall. On top of that, cyclic loading is introduced on the fan causing a fatigue problem [10, 15]. The total

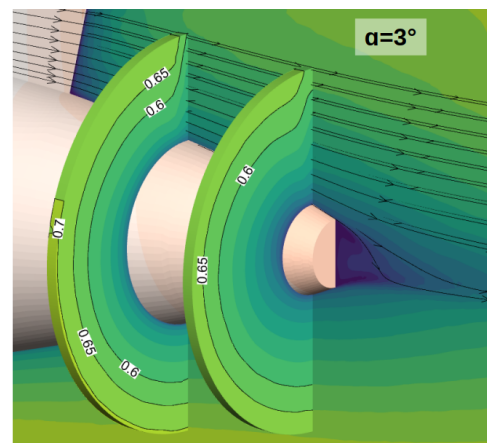


Figure 2.4: Contours of Mach number in the tailcone region. While the left disk does not by definition represent the location of the inlet, it is a good approximation. The disk on the right represents the location of the propeller [14].

pressure recovery is negatively influenced as well. Some important design variables in determining the performance are the inlet length and curvature of the S-duct which affect the formation of these vortices [15]. Another type of secondary flow in an S-shaped duct is the formation of horseshoe vortices at the intake lip where the thick BL does not hold enough energy to reach a full stagnation [16, 15].

Regardless, an S-duct may not be necessary in the case of the APPU. That is, because the engine is placed in a region of slower moving air as depicted in Figure 2.4. Since the engine is in a region of an adverse pressure gradient, the diffusion already takes place externally, i.e. without the presence of the inlet. Hence, it is apparent that the Mach number slows down from $M_\infty = 0.78$ to $M \approx 0.65$. So, the engine fan will experience an acceptable Mach number even without diffusion of the inlet. On top of that, the air inside the bottom part of the BL will be even slower. The duct may therefore not be required to have a classical S-shape, but could be parallel or even required to be convergent considering the slower moving BL air, which could ultimately suppress the adverse effects described above.

Amount of BL captured This is determined by the frontal shape of the inlet: a wider and lower inlet captures more BL than a slim and high inlet. So in order to exploit the benefits of BLI, a high width-to-depth or Aspect Ratio (AR) is desired. Besides, the distortion factor for a high AR inlet is lower since there is less variation in the velocity profile. Moreover, according to Dennard [17], a low AR ratio also results in adverse effects on the performance of a duct bend.

Fuselage integrated design As the inlet of the APPU is integrated into the fuselage, the air passing over the outside of the inlet must not be adversely affected by the presence of the inlet, especially since the BL is fully developed and thick at this location. In other words, flow separation must be minimized. This is especially important as the propeller will be influenced by this flow. On the other hand, as (part of) the BL is ingested, the BL surrounding the inlet will be reduced in size and hence is less prone to separation. Another important note is that the wake of the vertical tail influences the intake. Part of this wake, depending on the inlet parameters, could be ingested into the engine. As a result of both, the propeller faces a higher quality flow so the blades carry less structural loads.

2.1.3. Inlet Types

This section discusses various inlet designs of fuselage mounted engines that have been discovered in literature.

Submerged Inlets

A type of a flush integrated design is a submerged inlet, which is designed as a low-drag engine intake [18]. In the aviation industry it is often used at the APU. With this type of inlets, form drag is reduced due to streamlining of the surface, leading to an increase in overall efficiency of the aircraft. Moreover, the axial distance from the inlet to the compressor is also reduced, resulting in lower weight and drag. A drawback however is caused by the thick BL on the fuselage that can easily separate when disturbed by pressure gradients or shocks within the inlet. Even at subsonic Mach numbers separation at the curved duct poses an issue [9, 19]. Apart from the BL, another factor contributing to pressure losses is the vortex roll-up at the ramp walls [19, 20]. This vortex roll-up is only present in converging or diverging submerged inlets.

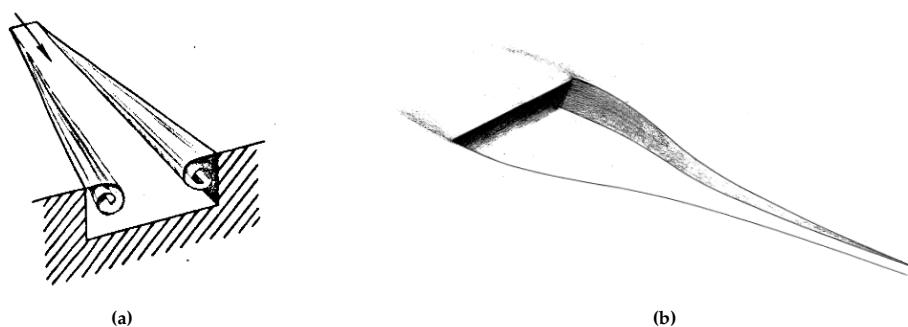


Figure 2.5: Vortex roll-up at the ramp walls due to non-parallel sidewalls [21] (a) & geometry of the well known NACA inlet [22] (b).

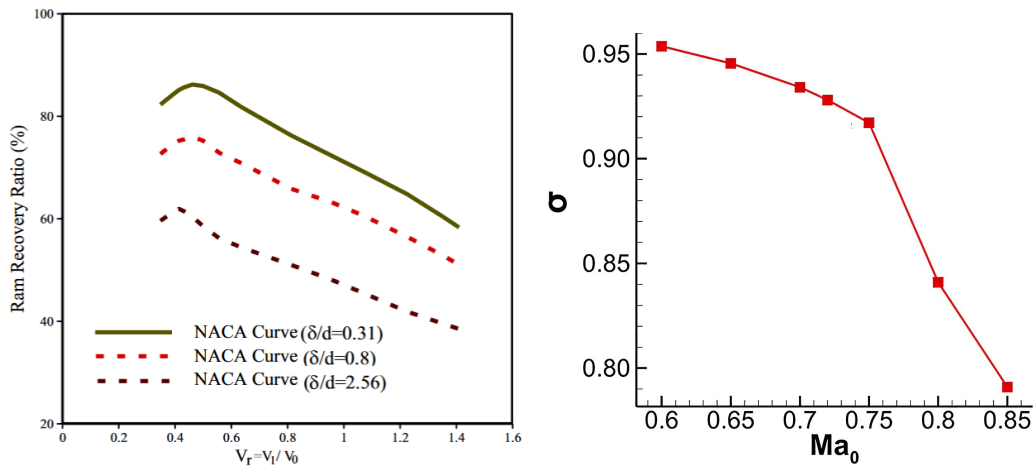
Three types of ramp configurations are possible: parallel, diverging or converging walls. For non-parallel wall configurations, a vortex sheet forms as the air must flow over the walls into the inlet. The vortex filaments will move into the ramp, since each filament is free to move and will hence move in accordance to the velocities induced upon it. According to Hime et al. [23] these vortices cause a thinning on the BL ramp floor, but cause total pressure losses. Divergence of the walls has a positive impact on the BL growth [21, 9]. Frick et al. [22] found that diverging walls which match the diverging streamlines show better pressure recovery of 8-10 % compared to parallel walls at low MFRs as spillage is detected in that case. A better improvement was introducing curvature to the divergent walls [24]. These are called NACA inlets. Concerning the drag characteristics at subsonic Mach numbers, this ramp plan form surpassed the parallel ramp configuration for higher MFRs, but for lower MFRs ($M < \pm 0.4$) higher drag values were observed. [25].

Frick et al. [22] discuss that the ramp angle has a notable effect on the ramp plan form. This is a more important parameter than the wall angle itself. They concluded that the ramp angles should not exceed 10° to prevent incurring excessive losses. Above this value, the effectiveness of diverging the ramp angle shows little effect and pressure losses increase significantly. Increasing the ramp angle increases the adverse pressure gradient.

Dennard [17] investigated the effect of the entrance AR on the total pressure recovery by comparing configurations with an AR of 1/4, 1 and 4. He found that a low AR was more favorable, but the difference was less pronounced at lower MFRs. A lower AR entrance draws in more air from the free stream (or upper part of the BL), causing higher total pressure recovery than a high AR entrance. Furthermore, the divergence effect decreases as the AR decreases, as the BL then is a smaller percentage of the total air. Hence, the the BL diverting mechanism caused by the diverging walls is then reduced [26].

For a low MFR, some air will spill to the outside of the inlet around the lip. As the direction of the vortex pair is dictated by the flow, the vortex pair is not (completely) swallowed but passes over the lip outside of the inlet resulting in a high recovery. Near the duct lip, in order to move away from the ramp floor it must leave the ramp walls at increasing angles, which induces a region of secondary flow and in extreme cases a secondary pair of vortices, introducing additional losses. These losses decrease for increasing divergence angle and increasing MFR. After some point, the vortex pair is sucked into the entrance and becomes the main source of pressure losses [27]. Figure 2.6a shows that for increasing BL thickness, the shape of the curve remains the same, but a significant drop in ram recovery ratio of about 15 % is visible for each increase in BL thickness.

For increasing free stream Mach number, the pressure gradient upstream of the lip is more adverse (due to compressibility effects), which gradually increases the BL separation and the vortex pair vanishes [28]. The result is that the total pressure is decreased as shown in Figure 2.6b.



(a) Effect of BL thickness on ram recovery ratio. Each line corresponds to a 160 % increase in BL thickness. The BL thickness ratio is defined as the thickness of the BL divided by the depth of the inlet entrance [27]. (b) Variation of pressure recovery for free stream Mach number [28]. Note that the geometry of the inlet is trapezoidal and not a basic NACA inlet, but the behavior is similar. The symbol σ is defined as the total pressure recovery.

Figure 2.6: Influence of flight conditions on the ram recovery ratio.

Scoop Inlets

Unlike the previous inlet type, scoop inlets protrude the fuselage surface as shown in Figure 2.7. Scoop inlets are favourable due to their partly buried cowl enhancing drag characteristics compared to underwing engines, but require turning of the flow by use of an S-duct which introduces non-uniformities. Scoop inlets often use a BL diverter to remove the BL and ingest higher total pressure. The main disadvantage of these inlets compared to NACA inlets is related to their protuberance into the flow, creating additional drag and a weight & structural penalty [29].



Figure 2.7: A scoop inlet mounted on the NACA research aircraft YF-93A [30].

Scoop inlets can either have a circular, elliptic or rectangular cross-sectional area. Semi-circular scoops show slightly better pressure recovery and drag characteristics than rectangular scoops [31]. Circular scoops in turn show higher pressure recoveries and lower drag than elliptic scoops [29]. Contrary to submerged inlets, scoops show very high drag due to excessive amounts of flow spillage at low MFRs but gradually perform better at a higher MFR. Dennard [17] discussed that a large length-diameter (L/D) ratio allows for re-attachment after separation. Although not defined accurately, the optimum L/D ratio lies in the range of 3 - 7.5.

Below, Figure 2.8 shows a comparison between a NACA and elliptic & circular scoop type intake based on a CFD study.

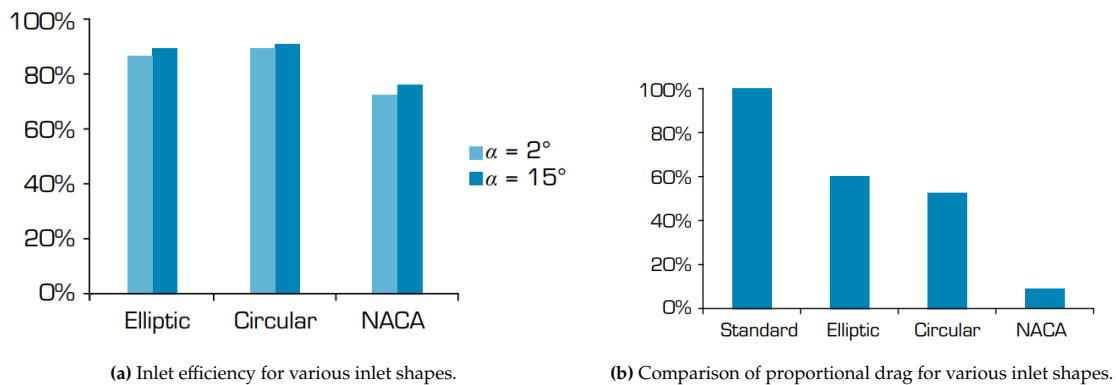


Figure 2.8: Comparison of inlet types on a canard type aircraft using a numerical approach [29].

Full Annulus Inlets

This type of inlet could not be found historically but has been explored in some recent novel propulsive fuselage projects. These full annulus inlets encircle the fuselage cone but are similar to scoop-type inlets. The difference lies in the much lower intake height and better streamlined body; the fuselage is further reduced in cross-section to prevent a big protrusion, resulting in a more aerodynamically streamlined body. Full annulus inlets also allow more flexibility in shaping the intake duct, since the duct does not need to turn at sharp angles to face the fan. Moreover, as this type of inlet encircles the fuselage completely, a relatively small discontinuity or gap is required on the fuselage surface, minimizing drag

mainly at low MFRs. On the other hand, the surface area is higher and there is a higher risk of foreign object damage. Figure 2.9 presents such an inlet.

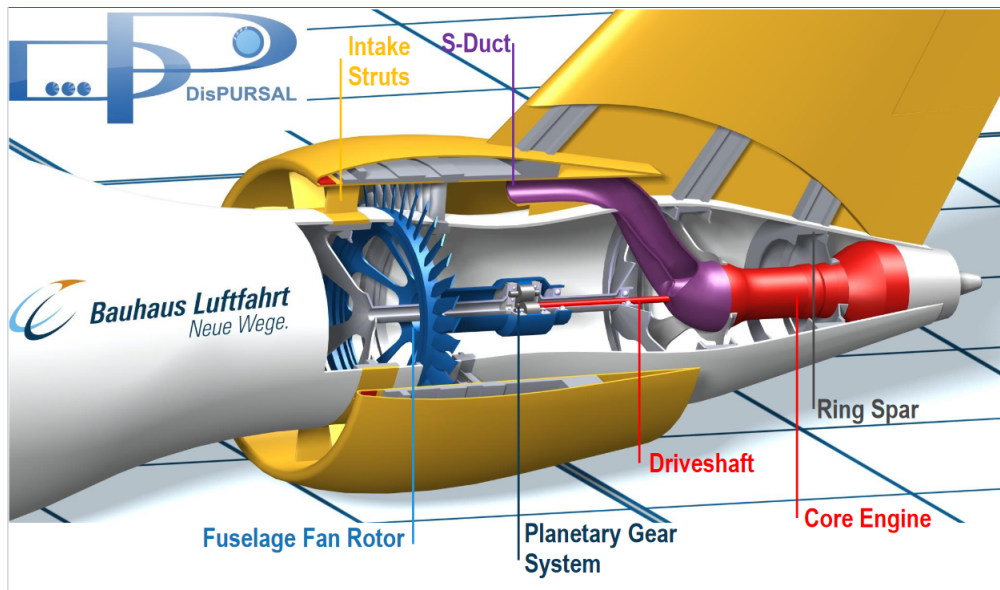


Figure 2.9: DisPURSAL BLI engine layout [32].

2.2. Research Motive

Before presenting a discussion on the intake, it is useful to consider the APPU engine layout. As such, the layout is presented in Figure 2.10.

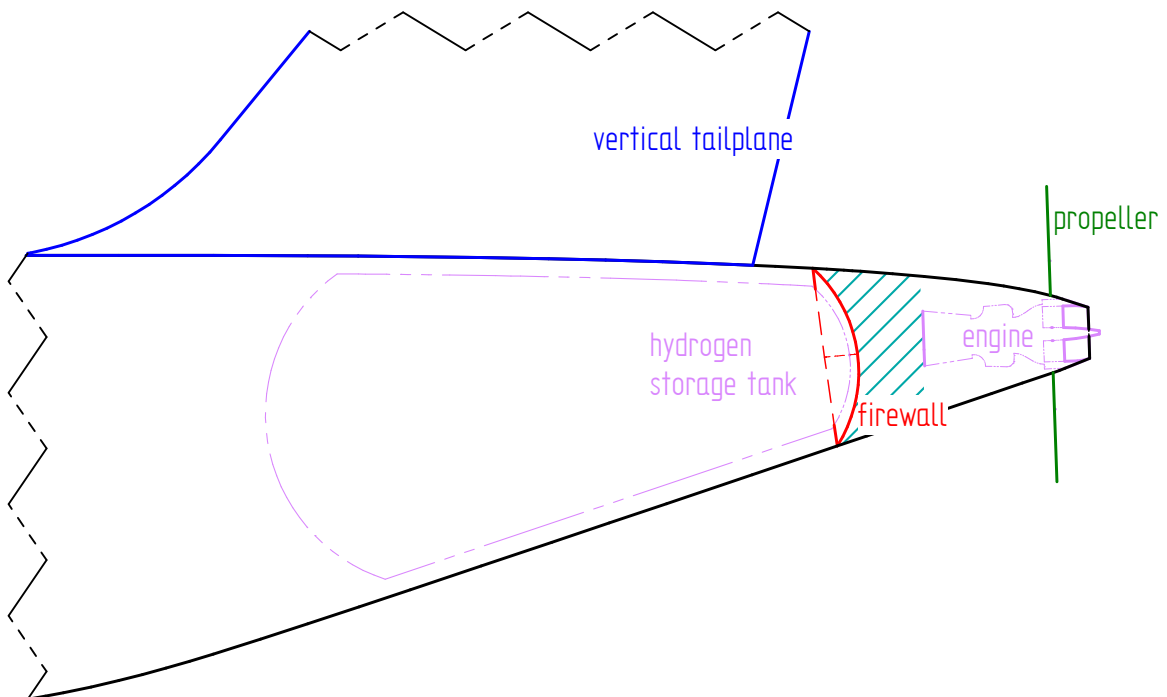


Figure 2.10: Layout of the APPU tailcone

It is apparent that **scoop inlets have a higher drag & pressure recovery than NACA inlets** [31]. It is also clear that scoops are favored when high mass flow engines are required with large pressure recoveries and NACA inlets are preferred as small inlets where pressure recovery is of less importance. However, it is not very clear, quantitatively, at which values which design option is superior.

Many recent papers have focused on eliminating the detrimental BL effects. Xie et al. [33] gave a quick summary of recent improvements on NACA inlets and showed that this is done by either distancing the engine from the body wake, creating a 'slot' which diverts away the BL, or by creating a vortex using an obstacle upstream of the intake that is also diverted away from the inlet. These methods however lead to an increase in weight and drag [9]. Additionally, these solutions would defeat the purpose of BLI. Therefore, the historical scoops and NACA inlets would be more suitable within the context of this project.

It is more appropriate to move away from the classical scoop design and focus on submerged inlets instead, as implementing scoops would imply the following:

- Even if a superior total pressure recovery is acquired, the BLI effect must then counteract the higher drag regardless, which especially poses a problem at higher flight speeds.
- As an open rotor engine design is utilized, the scoop poses a problem to the quality of the flow faced by the propeller, particularly when the MFR is very low, or when the engine is turned off. In that case, a high spillage drag is observed and the flow may separate before facing the propeller.

In opposition, it seems like NACA inlets are not the most suitable option either due to the following reason:

- As stated by Mossman et al. [26]: "at velocity ratio's below 1.0 the boundary layer outside the ramp would have a tendency to flow away from the inlet." This statement is confirmed in a numerical study conducted in 2016 by Pignier et al. [34]. Although the option exists to round off or fillet the top edge of the walls, the divergence effect would then be greatly reduced.
- Sacks [21] argued that there is a certain trade-off in NACA inlet design: that which increases the pressure recovery due to diverting the vortex sheet away, appears as external drag instead. In view of BLI this behaviour is unwanted. As the vortex sheet mixes the BL air with the free stream air and transports it away from the inlet entrance, the BLI impact will be reduced. The vortex sheet also causes distortion on the propeller.
- Additionally, upon inspection, a NACA inlet with regular dimensions does not fit into the available inlet space. As a solution, either the width-to-depth ratio of the entrance must be extremely large³, or a distribution of NACA inlets must be utilized. The former introduces uncertainty, since an AR of such high value, as well as a NACA inlet that is (highly) curved (to be able to match the fuselage curvature) have not been tested before, whereas the latter would result in a large amount of vortex formations influencing each other downstream.

Next, although no research could be found comparing the performance of full annulus inlets to the other designs, it could be argued that this type of inlet is satisfactory due to its proven performance in recent research, but upon inspection, geometrically this inlet might not be applicable. A reduction of the cross-section of the fuselage at and upstream of the location of the nacelle would be difficult to achieve due to space constraints on account of the hydrogen storage tank as previously.

Alternatively, a new type of design may be considered which combines the full annulus inlets and submerged inlets. The low drag properties of submerged inlets along with the benefits of full annulus inlets could prove to be a great solution.

2.2.1. Research Gap

Particularly in recent years, lots of projects have focused on exploiting the benefits of BLI on modern-day passenger aircraft. Most research focuses their work on the application of BLI on either turbofan engines or turbo-electrically powered propulsors. In these PFC concepts, use has been made of full annulus inlets, featuring a nacelle encircling the fuselage circumferentially. It is possible to design a similar inlet for the APPU. While it would be harder to do so, with the help of some modifications it would not be considered impossible. As an alternative, a scoop type inlet could also be investigated. The third and last option is to explore the feasibility of submerged inlets. The open rotor design of the A321 APPU as a choice for the auxiliary BLI engine is something that is either non-existent or very limitedly explored in literature. Therefore, all three inlets could be evaluated; there is a high amount of freedom in the design choice of the inlet configuration for the propulsive BLI engine.

³which, considering the limited axial space, also implies a large divergence angle well beyond standard NACA dimensions

Advances in both scoop type inlets as well as submerged inlets are directed towards diverting away or eliminating the BL, either by way of numerical or experimental simulations. However, there is a lack of research dedicated towards the use of these inlets in the context of BLI. The full annulus inlet type is an exception to this, but even this type of inlet is still relevant to investigate, as this thesis aims to design an inlet to the engine core, contrary to common practice where the bypass-air is the main focus of the project.

To sum up, it is believed that regardless of which type of inlet is selected, the findings of the thesis are expected to provide greater certainty regarding the suitability of the respective intake in the context of BLI and aid in closing the research gap.

2.2.2. Research Question

Based on the research gap, there are several ways to define the thesis topic. To limit the scope, designing the most efficient inlet that minimizes losses is not considered. Whilst it could be opted to investigate both the scoop and submerged inlet type in order to conduct a comparative study, it would be necessary to iterate in both designs in order to perform a meaningful comparison. Due to time constraints, this option is also overlooked. Hence, through the discussion provided earlier, it has been decided to design a submerged inlet type instead and alter geometric features of the inlet to investigate the effects of the applied changes on the flow field. Accordingly, the research question is:

- **What key parameters are most significant in designing a submerged inlet to a boundary layer ingesting engine that minimizes detrimental flow behaviour both internally and externally of the intake?**

The thesis aim is thus two-fold: to systematically alter the inlet geometry & investigate its impact on the flow field, and draw conclusions on how to determine the shape of the intake.

This research topic would not only provide material for the feasibility of submerged inlets in the context of BLI, but investigating its geometric parameters would provide useful academic information into the shaping of such an inlet at the same or similar conditions.

3

Methodology

The approach of this thesis to answer the main research question is by utilizing Computational Fluid Dynamics (CFD). CFD is a widely used technique to predict flow properties by solving the governing equations. In CFD, a set of governing equations capture the physical system. These partial differential equations are called the Navier-Stokes equations and describe how the velocity, temperature, density and pressure of a fluid are related to each other. Compared to wind tunnel tests, CFD has several advantages [35]:

- It is much cheaper to simulate designs, while on the other hand experimental tests require extensive design and data points [36].
- It takes a significantly shorter time to obtain results.
- It gives the ability to acquire results on any point on the object with high detail. In the case of experimental tests, results are only available at probes/sensors.
- It gives the ability to simulate (at) many different conditions.

As the governing equations are too difficult to solve analytically, the flow domain is discretized into cells, whereby the equations are approximated numerically instead [37]. Accordingly, three key steps are involved in a CFD simulation [38]:

1. pre-processing: generating the mesh
2. simulation: solving the governing equations
3. post-processing: analysing the results

Correspondingly, the methodology of this project is defined in four major steps. In sequence, these are to create the inlet geometry, generate a mesh of the domain, perform a simulation and analyse the results. These steps are elaborated on in the upcoming sections.

3.1. Geometry Creation

All figures from this chapter onwards illustrate only half of the geometry. As will become apparent in Section 3.3.2 a symmetry plane is present at $Y = 0$ (see Appendix A for an orientation axis). However, when describing the azimuthal extent of the intakes, the full geometry is considered. I.e., when a 360° intake is mentioned, the figure will display a geometry with a range of 180° . For convenience, most figures are oriented with the positive Z-axis pointing upwards.

All important components located at the tailcone were previously shown in Figure 2.10. It is clear that there should be a high emphasis on shaping the inlet correctly, as turning angles are expected to be high due to a limited amount of available space.

3.1.1. Description of Geometry

Duct shape For aerodynamically efficient design, the following should hold when shaping the duct:

- The changes in cross-sectional area should be kept small. Sudden/sharp area gradients can result in excessive diffusion of the flow, which can cause separation due to the positive pressure distribution ($dp/dx > 0$) that follows.
- Sharp changes in increases in cross-sectional area, i.e. the derivative of cross-sectional area, should be kept minimal. A typical bad example would be a circular bend connected with a straight line [39], referred to as an elbow bend. Even though the two elements may be tangent with respect to each other, the flow experiences a sudden change in the magnitude of the curvature, which causes separation. A solution to this would be to apply curvature-continuity instead wherever possible & convenient. Here, both the sign and the magnitude of the curvature are kept equal across multiple sketch elements, see Figure 3.1 for a visual representation.

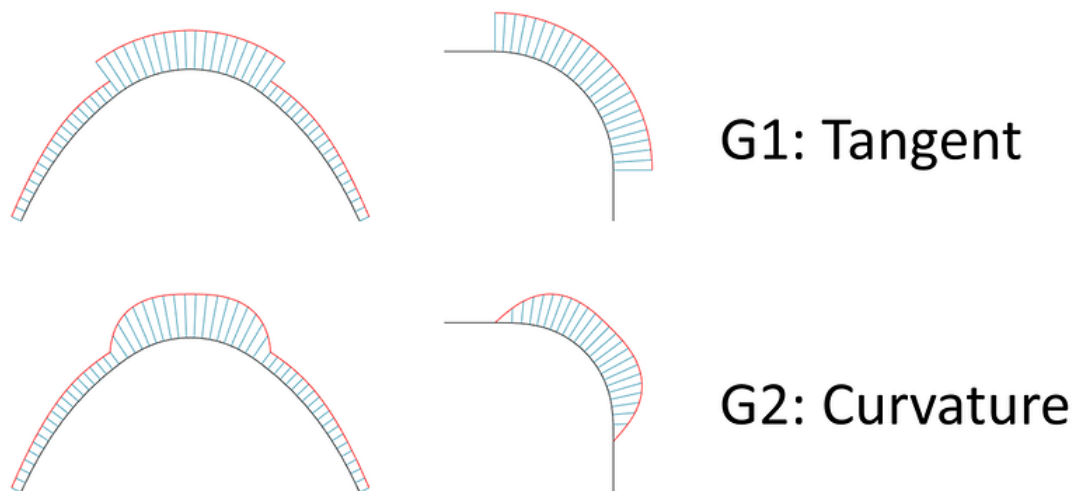


Figure 3.1: The two types of continuity connection of two curves [40]. Note that G3 also exists, where the rate of change in magnitude is kept constant, but unfortunately is not integrated into the software environment that is employed in this thesis.

- Ideally, the duct must ensure that the flow faces the compressor as axially aligned as possible, that is with a vertical component that is not too large. This, in order for a better performance of the compressor.

Lip Although the typical NACA lip as shown by Pignier et al. [34] has proven its effectiveness in literature, it was realized that designing such a lip would require excessive turns in the duct due to the innate shape of the lip. Hence, it was decided to solely model the circular part of the lip, highlighted in red in Figure 3.2b, where the radius is specified according to the duct entrance thickness D : $R_{NACA} = 0.094 * D$, corresponding to 100%. For the first design, a lip radius of 150% was employed.

Entrance Area As an initial estimate for the first design, the entrance area was determined by inspecting the simulation case of the base aircraft. A disk surface was created at the estimated position of the inlet (similar to Figure 2.4), with a thickness that was adjusted to match the required mass flow rate. The thickness of this tube was then used as the entrance thickness of the duct.

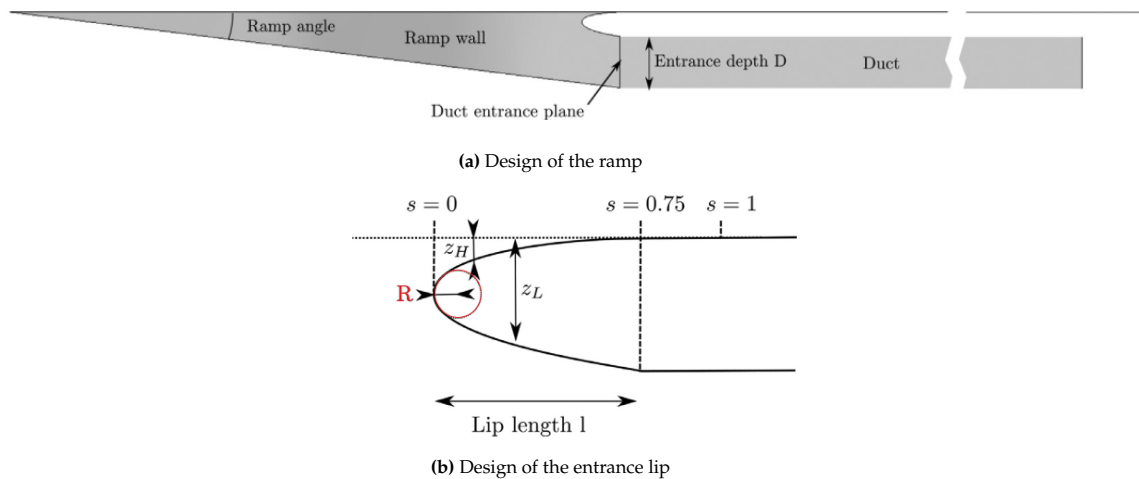


Figure 3.2: Parametric model to design a submerged inlet entrance. Provided by Pignier et al. [34].

Compressor Area As mentioned in Chapter 2, the maximum Mach number at the compressor is limited by compressibility effects at roughly $M \approx 0.6$. Because the mass flow rate is constrained by engine thrust requirements, the area ought to be increased/decreased in case the observed Mach number is too high/low respectively. For the first design, the compressor area provided by a simulation run in Gasturb was utilized.

3.1.2. Geometry Definition

The software Solid Edge [41] has been used to construct the geometry. Solid Edge is an industrial and widely used 3D Computer-aided Design (CAD) software that is developed by Siemens. Solid Edge allows the user to model a geometry for engineering purposes in a variety of different ways by offering several distinct parametric design features. The geometry consists of two segments; the inner and outer duct surfaces are generated separately. For the 'Full Annulus' (FA) design, a sketch of the top and bottom sections were made on the symmetry plane. The duct faces were generated using the sweep command by using the fuselage circumference as upstream and the outer edge of the compressor as downstream guide curves. In-between sections are not specified for this design, as it was noticed that the geometry is well-defined and hence guide curves were not necessary. As for the 'Half Annulus' (HA) Design, due to its complex 3D shape, the duct is generated in two successive parts and presented in Figure 3.3.

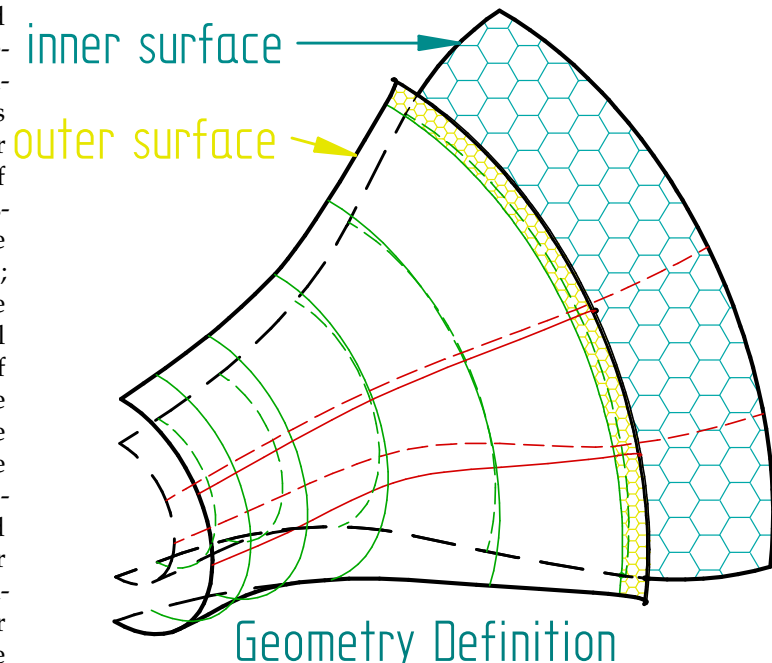


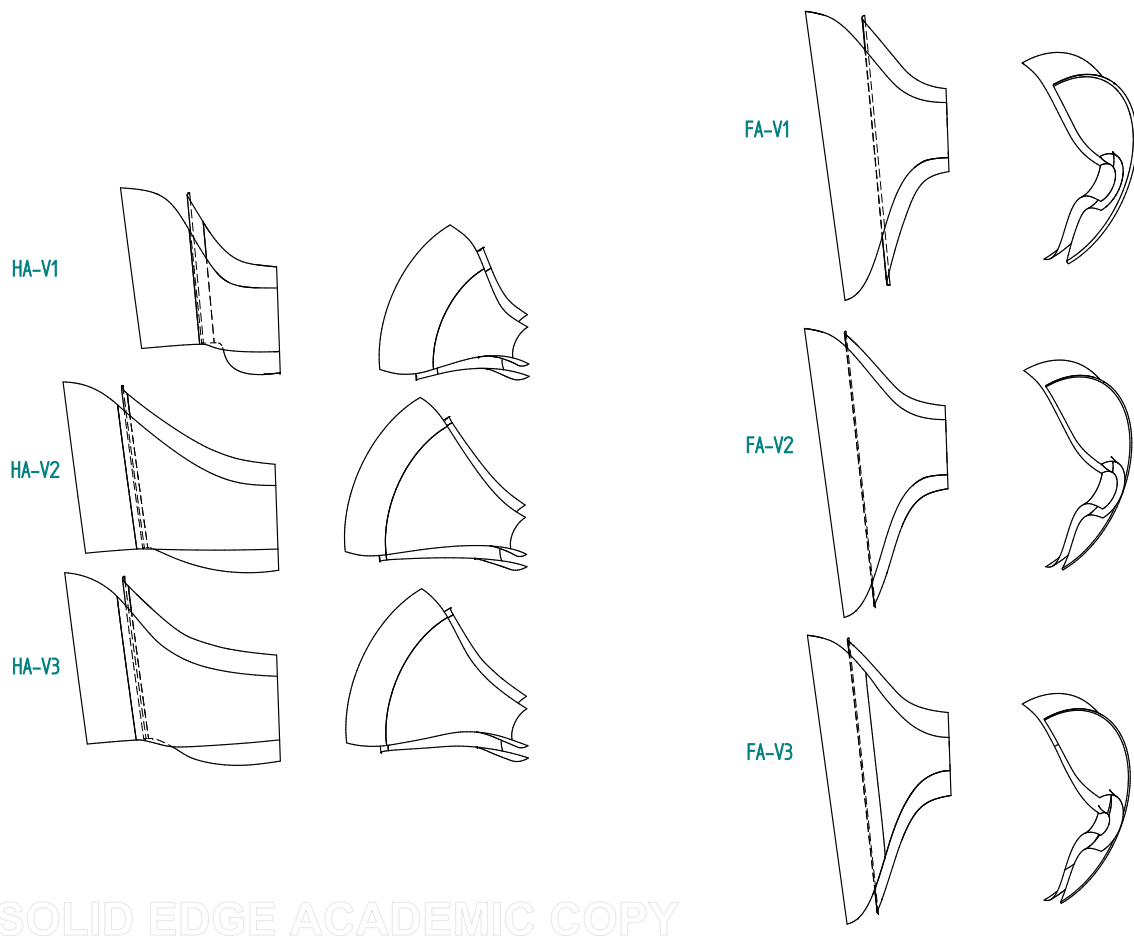
Figure 3.3: Definition of the HA geometry. Part I is shown in a honeycomb pattern. The red lines show longitudinal sections and the lines in green present cross-sectional sketches. Curves belonging to the inner surface are dashed.

- **part I:** Entrance. A swept surface is generated using sketches on several azimuthal positions: the symmetry plane, 90° plane, 135° plane and 180° plane (or: side plane). The surface is constructed in a similar fashion to the FA design.
- **part II:** duct. This part is generated adjacently to part I. The shape is now out-of-plane, since the 180° ranging surface must connect to the 360° compressor face. Similarly as before, multiple cross-sections and guide-curves were defined beforehand¹ to give more robustness & better definition to the duct shape. However, on this occasion 3D -instead of planar- curves are used for the longitudinal sections on the 135° and 180° extent.

Furthermore, the surfaces were made tangent/curvature continuous to the upstream fuselage surface & downstream engine surface wherever possible in order to maintain a smooth transition.

3.1.3. Overview of Geometries

Figure 3.4 shows a front and 3D view of the investigated models.



SOLID EDGE ACADEMIC COPY

Figure 3.4: Overview of all geometries

The methodology in determining the geometries is as follows. Each iteration is built on the simulation results of the previous iterations. I.e., after performing the simulation and inspecting the results, detrimental flow is first identified and afterwards, changes are made to the next iteration that are believed to diminish these adverse flow characteristics. For the very first design (FA-V1), an initial guess for the lip shape and duct entrance D were made and were explained previously in Section 3.1.1. In

¹The longitudinal sections were defined first, defining the trajectory of the cross-sections. For the HA-V3 design, however, the longitudinal sketch on the symmetry plane was created first, then the cross-sections were generated and finally, the remaining longitudinal sections were constructed to ensure circular cross-sectional sections.

specific, the changes with respect to each iteration are elaborated upon in more detail in Chapter 5. Due to time constraints, multiple changes have been applied to each updated geometry. This makes it more difficult to couple the cause and effects, but through reasoning using aerodynamic fundamentals, academically relevant conclusions can be drawn nevertheless. The reader is referred to Appendix A for a more detailed illustration of the HA and FA designs in Appendix A.

Lastly, geometric features of all tested designs including major changes are listed and described in Table 3.1, where D is the entrance thickness, R is the lip radius, C is the corner radius, L is the intake length and θ represents the entrance azimuthal range. A visual representation of the parameters can be found again in Appendix A.

	\dot{m} [kg/s]	Comp. Area [m ²]	D [mm]	R [mm]	C [mm]	L [mm]	θ [°]	Extra description
Base	-	-	-	-	-	-	-	<ul style="list-style-type: none"> • No inlet present • Simulation data provided for at start of thesis.
FA-V1	4	0.07	88	12.27 (150% ^a)	-	680	360	<ul style="list-style-type: none"> • Full-annulus design
FA-V2	4	0.07	45	7 (150%)	-	680	360	-
FA-V3	5	0.106	45	7 (150%)	-	680	360	<ul style="list-style-type: none"> • mass-flow continuity compressor-nozzle
HA-V1	5	0.106	75	9.87 (150%)	0	680	180	<ul style="list-style-type: none"> • Half-annulus design
HA-V2	5	0.106	70	6.11 (100%)	0	920	180	<ul style="list-style-type: none"> • smoother lip/duct transition • Smoother area distribution
HA-V3	5	0.106	70	8.18 (150%)	25	920	180	<ul style="list-style-type: none"> • fully converging Area distribution • longer horizontal part: $\frac{h}{L} = 21\%$ vs 13%^b • circular cross-sections^c

Table 3.1: Overview of all designs presented in this thesis. Text highlighted in color defines changes that are also present in the iterations below.

^aLip radius of 100% corresponds to NACA lip with $R = 0.094 \cdot D$, refer to [34].

^bRefer to Appendix A for an illustration.

^cThe cross-sections were previously splines with varying curvature.

3.1.4. Rolling-Ball Method

In order to determine the axial area distribution, the so-called rolling-ball method has been employed. The use of this technique is illustrated in Figure 3.5 in four consecutive steps. First, the axial position of the ball is determined parametrically. This is done by creating a horizontal line from the start to the end of the duct, and afterwards projecting the point vertically up to where the line meets the duct surface. A plane is generated that is tangent to the duct at this position (Figure 3.5a). Then, the rolling-ball is sketched on this plane. Figure 3.5b visually shows the implementation of the rolling-ball in a randomly generated duct. First, a circle is created that touches and is tangent to the duct surfaces. Then, two lines are constructed that are each tangent to the ball and tangent to the duct at the intersection point between the ball and duct. Connecting the end points of the two lines gives a line (green), serving as a representative cross-section at that particular position x . Due to the inherent complex 3D geometry, the sections at the top and bottom of the duct are not equal in shape. Hence, an additional 'ball' is also constructed at the top section of the duct for a more accurate representation. This is shown in Figure 3.5c. The only complication that remains is that the intake is constructed at a certain angle, due to the fact that the engine (α) and the firewall (β) are at an angle with respect to the vertical axis. So, the

position of the ball at the top is determined by creating a plane at an angle φ that is linearly interpolated between the angles α and β . Finally, the surface is generated by connecting the two ball lines after first generating guide curves on the inner and outer duct. These guide curves were created by intersecting planes with an angle of φ with the inner and outer duct surface, see Figure 3.5d. Performing this strategy at multiple axial positions will give an estimation of the axial area distribution of the geometry. The described methodology is implemented in Solid Edge, where the variables are defined parametrically: after inserting a value for x , the steps in a) - d) are performed automatically.

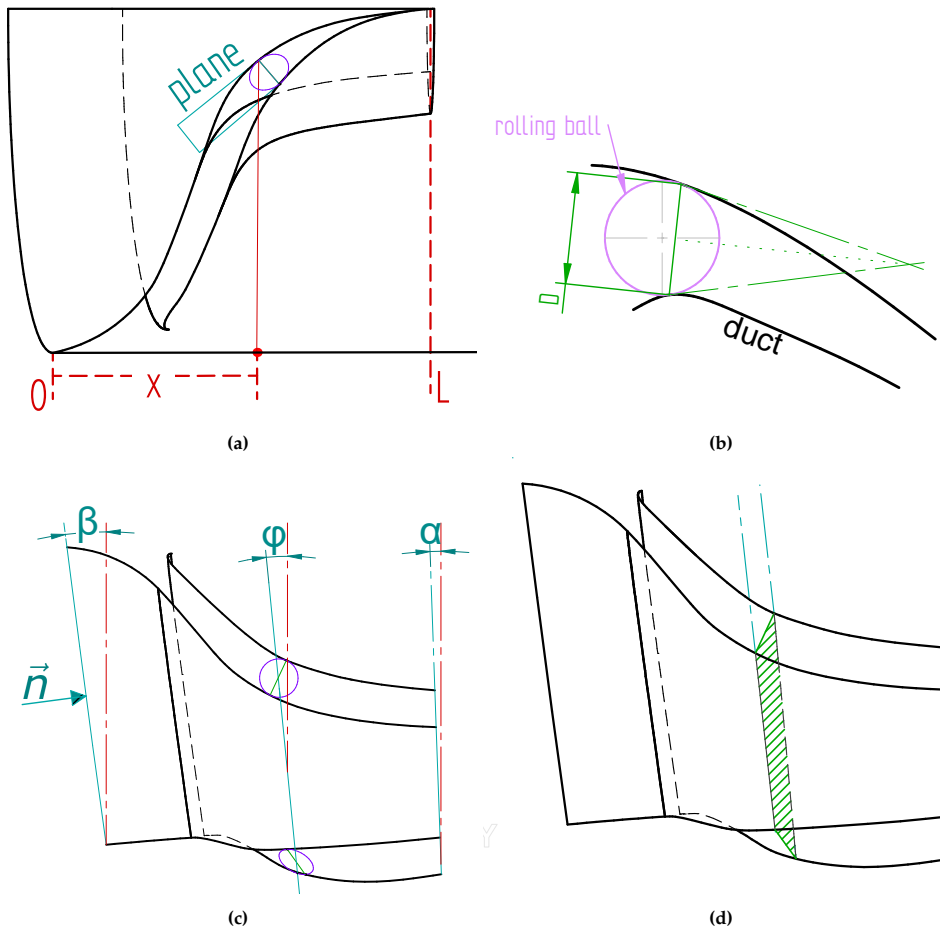
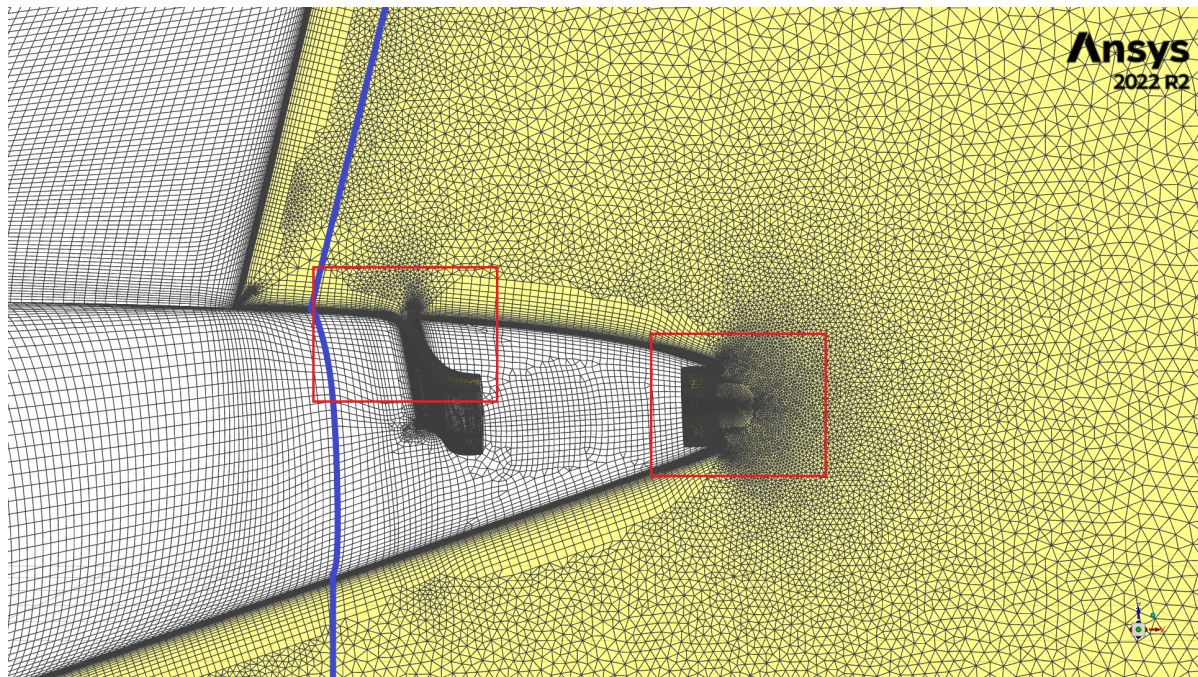


Figure 3.5: Illustration of rolling-ball method. The planes in figures c) and d) are oriented towards the viewer, where the normal direction is shown in c).

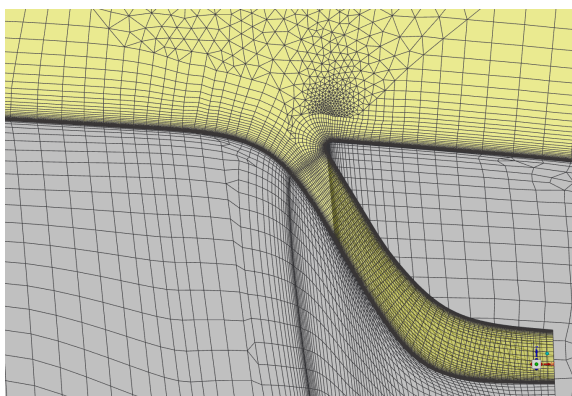
3.2. Mesh Generation

In a CFD analysis, the domain is discretized into control volumes or cells, the collection of which is referred to as the mesh. The mesh has been constructed manually for each design. An emphasis is held on the mesh quality in order to improve solution robustness and accuracy, specifically by constantly examining and ensuring a low area/volume ratio, smooth transition in cell size, and a high orthogonal quality. Due to the complex nature of the geometry, a hybrid between structured and unstructured cells has been employed, though a structured mesh is used in regions where possible due to the high amount of control on quality for this mesh type and other distinct advantages. At regions where this is not possible however, such as triangular-like corners, such as Figure 3.7, an unstructured mesh is used instead. Figure 3.6a shows an overview of the generated mesh at the region of interest. Though dependant on the design, the amount of cells in the tailcone region is roughly 1.5 million². Figure 3.6b and Figure 3.6c show a zoomed in view of the intake and nozzle respectively. More detailed views of the mesh are shown in Appendix B.

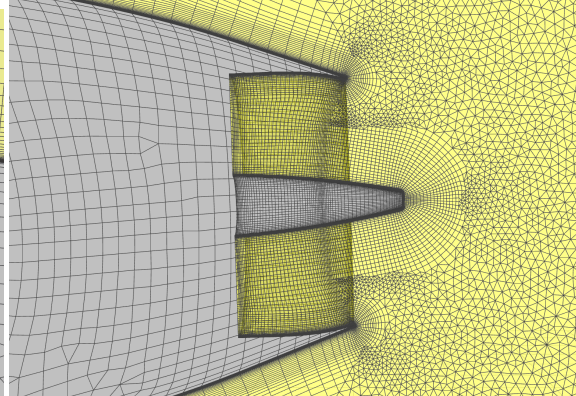
²Accounting for all cells in the near field block of the tailcone, excluding the far field domain



(a) Mesh around the tailcone. The surface mesh is mainly structured, with exceptions of a few areas, whereas the near field and far field domain (out of frame) consist of unstructured cells.



(b) Mesh on the symmetry plane at the location of the intake. Structured cells are built on top of the BL mesh until isotropy is reached, after which the algorithm switches to the formation of unstructured cells. The mesh right of the blue line is modified within this thesis.



(c) Symmetry mesh at the aft region of the tailcone and nozzle. An O-mesh is built around the fuselage trailing edge, where the cone is cut off by a negligible amount to create a blunt trailing edge, allowing the cells to march around the corner with a relatively low skewness angle.

Figure 3.6: Mesh topology around tailcone region.

As visible in Figure 3.7, the front end³ of the duct wall has been slightly modified. Originally, the intake ramp (at the sidewall) was continuous with the upstream fuselage curvature. However, it was realized at the location where the ramp and fuselage meet, this would necessitate slender cells with an extremely high aspect ratio at the triangular-shaped corner (highlighted in red), making it very difficult to blend in the remainder of the surrounding mesh. In that regard, the boundary layer mesh faced even more difficulty due to the particularly small cell sizes close to the wall. Hence, for convenience purposes, as the mesh must be constructed for multiple geometries, it was decided to adjust the geometry by merging the connectors at the ramp, results in a higher angle between the fuselage surface and ramp surface. This facilitates the transition in cell size. As the applied modifications are on a very small degree, the expected effect on the results is considered negligible.

³The same is applied at the rear end. That is, at the junction between the duct sidewall and the intake lip.

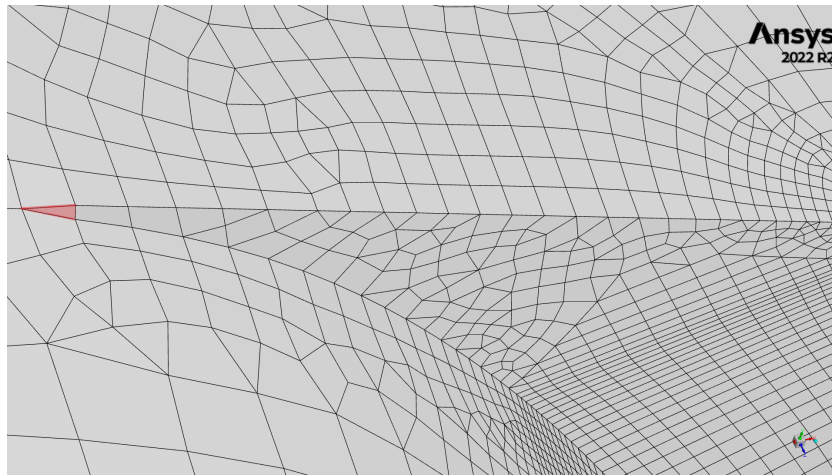


Figure 3.7: Surface mesh at the sidewall. The area highlighted in red is modified, which otherwise would result in the formation of extremely anisotropic triangular cells due to the tangential connection between fuselage and intake ramp. Although this modified cell still has relatively high anisotropy, it is a major improvement compared to the original shape.

Another important aspect of mesh quality is mesh refinement at regions of high expected flow gradients, including most prominently the boundary layer. In that regard, it is important to consider the non-dimensional cell distance to the wall: y^+ . The wall y^+ must, depending on the turbulence model and utilization of wall functions, lie within specified bounds. In this case, as the boundary layer will be fully resolved and given the turbulence model, the y^+ must ideally be close to 1⁴ More on this will be provided in 4. The following formula has been used to approximate the correct grid spacing to obtain this y^+ value [42]:

$$\Delta s = \frac{y^+ \mu}{U_{fric} \rho} \quad (3.1)$$

Equation 3.1 stems from flat plate boundary layer theory as derived by White [43].

Figure 3.6b visualizes the boundary layer mesh close to the wall. The boundary layer has a size of 40 cells with a growth rate of 1.2. The computed Δs is equal to 10^{-5} . The boundary layer mesh is generated by creating an extrusion in normal direction of the surface mesh domains. An unstructured volume mesh is generated on top of this block, where the software switches to the unstructured format in case isotropy is reached.

The program Pointwise [44] is used for mesh generation. It should be noted that the entire mesh upstream of the tailcone, see Figure 3.6a, was available beforehand. Hence, during the course of the thesis, that section of the mesh was not modified⁵. For the various iterations, most of the mesh had to be reconstructed from scratch, but connector information (i.e. distribution type and node count) were shared between iterations. The nozzle region however did not have to be adapted and remained unaltered after the correct mass flow rate was obtained.

3.3. Simulation Set-up

Due to the inherent complex geometry of the model, a (steady) 3D simulation is required to accurately capture the flow physics. The program Fluent [45] developed by ANSYS is employed to perform the simulation. Fluent uses the finite-volume method to solve the governing equations. The simulations are run on the High Performance Cluster (HPC) department of TU Delft as high CPU power is required to simulate the high cell count case file. Compressibility effects are accounted for by using the density-based solver. A second order upwind scheme is used for increased numerical accuracy. Below, some important simulation settings are further elaborated upon. It is worth noting that the simulation settings (excluding the additional boundary conditions) were not implemented by the author. Rather, those were formerly applied and executed by the supervisor for the base aircraft simulation. The same settings were used in this thesis, as it allows for more accurate comparisons with the base configuration and as these settings are considered to be compatible with the thesis scope, which will become apparent in the next section.

⁵With two exceptions: 1) during the refinement study and 2) for the last two designs, where the surface mesh upstream of the intake had to be modified due to the longer intake length

3.3.1. Turbulence Modelling

Laminar flow is completely described by the governing equations used to solve the system. At high Re numbers, turbulent flow becomes more important. Turbulence is characterized by fluctuating velocities, which cause the mixing and fluctuation of other transported quantities such as energy and momentum. So, it is essential to accurately capture turbulence in the simulations in order to get reliable results.

There are different methods that deal with turbulence. Despite the fact that turbulence can be directly resolved on all time-scales with direct numerical simulation, this is extremely computationally expensive. And although a large Eddy simulation resolves only large scale turbulence by using a filter and including the effect of the small-scale eddies on the resolved flow by means of a sub-grid scale model, the amount of computational resources required in this case is also still too high [35, 46].

Instead, Reynolds-Averaged Navier Stokes (RANS) equations govern the mean flow properties by time-averaging the Navier-Stokes equations. The appearance of fluctuations on these time-averaged Navier-Stokes equations cause additional stresses on the fluid called Reynolds stresses and must be modelled. There are different models that deal with these extra stresses [35], and each introduces a different amount of additional transport equations. For this thesis, the $k - \omega$ SST [47] RANS model is used, as it combines the advantages of the $k - \omega$ model (close to the wall) and $k - \epsilon$ model (away from the wall). Furthermore, it has been proven reliable for external aerodynamics with reasonably high accuracy [34], and has been applied in multiple similar research [29, 33, 27, 48, 49].

3.3.2. Computational Domain and Boundary Conditions

The computational domain consists of a hemisphere with a radius of $500m$, which is roughly 10 times the length of the aircraft. Figure 3.8 illustrates the domain.

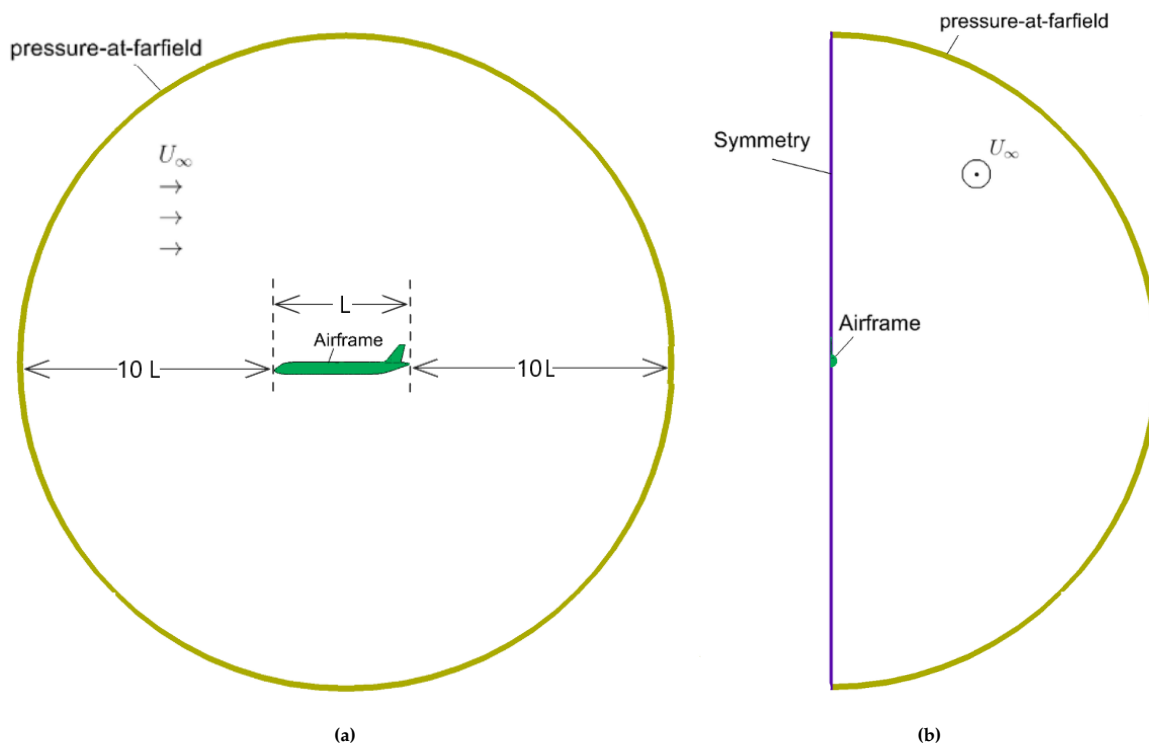


Figure 3.8: Sketch of the computational CFD domain with a) front view and b) side view with relevant boundary conditions. Note: the drawings are out of scale.

The **pressure-at-farfield** boundary condition is applied at the edge of the hemisphere where (static) ambient conditions (p and T) are specified. Since the model is symmetric about this plane, a **symmetry** boundary condition is applied at $Y = 0$ to reduce the computational costs by half.

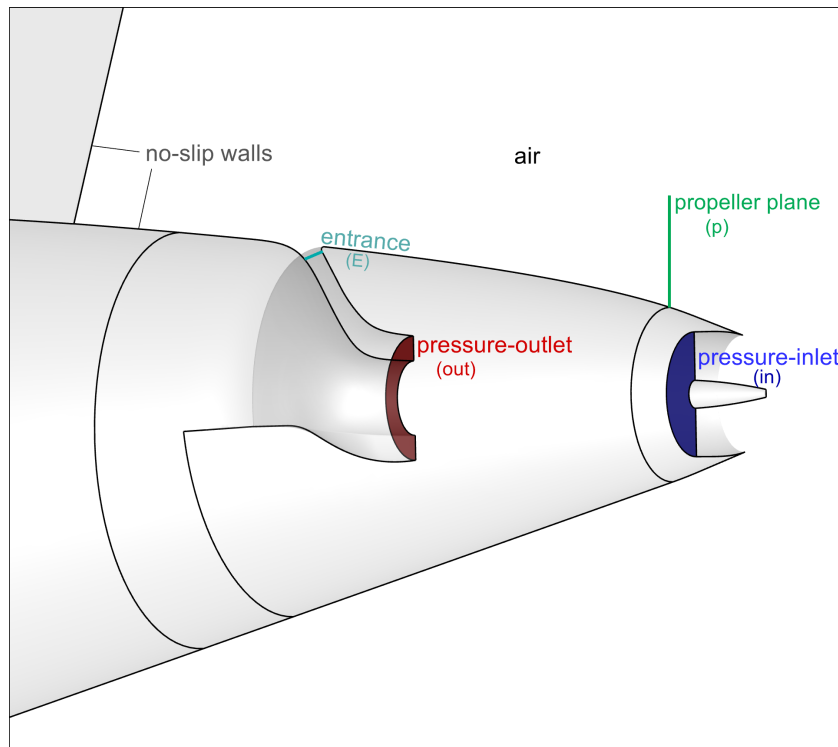


Figure 3.9: Boundary conditions at the tailcone.

Figure 3.9 shows the remainder of the applied boundary conditions. Since the engine interior is not modeled, a pressure-outlet & pressure-inlet boundary condition have been applied at the compressor and domain inlet⁶, respectively. At the **pressure-outlet**, an initial guess for the static pressure is given as input and a target mass flow rate is set, after which the pressure data is calculated to match this flow rate. At the **pressure-inlet**, the total pressure is specified, after which the velocity and other field variables are calculated using the surrounding flow field. This total pressure is estimated at a given 10.484 kPa. To ensure continuity between the two boundaries, the area of the pressure-inlet boundary has been adjusted to achieve a mass flow rate (nearly) equal to that at the domain outlet⁷. Note that this procedure has been performed for FA-V3 only, but the mass flow continuity has been valid for the upcoming iterations as well since the engine mass flow was not altered hereafter. The remaining small mismatch in mass flow rate is accounted for, which will be explained shortly after. Finally, the air frame consists of **no-slip walls**.

⁶the inlet boundary is located between the turbine exit and nozzle plane, see Figure 2.10

⁷This means that the nozzle geometry as visible in the sketch is not representative of the APPU, it is merely adjusted to obtain the correct mass flow rate. However, this will not pose a problem to the obtained results, since the nozzle shape will not affect the inlet performance.

3.4. Overview of Test Conditions

Two flight conditions have been considered: cruise and Sea Level Static (SLS). The intake has been designed for cruise, but its performance has been verified at SLS as this is also regarded as an important flight condition, particularly since one of the design requirements of the aircraft requires the APPU to deliver the required thrust to take off. Unless specified otherwise, the specifications provided in Table 3.2 are consistent throughout all design iterations.

Property	Condition	
	Cruise	SLS
mass flow rate \dot{m} (kg/s)	5 ^a	20 ^a
Altitude h (m)	11582 ^a	0
Temperature T (K)	216.7	288.15
density ρ (kg/m ³)	0.3363	1.225
Pressure p (Pa)	20916	101325
Viscosity μ (kg/(m * s))	1.421884e-05	1.7894e-05
Velocity v (m/s)	230.18	17.15
Mach Number M (-)	0.78	0.05 ^b
angle of attack α (°)	3 ^a	0
Reference Area A_{ref} (m ²)	122.6	

Table 3.2: Test conditions

^aThese values are still uncertain/changed during the project, so are not fully representative of the APPU aircraft.

^bTo avoid convergence problems for the density-based solver in Fluent, a Mach number slightly higher than 0 was adopted.

3.5. Performance Evaluation Metrics

In order to assess the different designs and subsequently apply changes for next iterations, it is imperative to either qualitatively or quantitatively grade the designs with each other. Hence, performance criteria are set up in order to do so in a systematic manner. These are listed in Table 3.3.

Metric	Symbol	Assessment method
Pressure Drag coefficient	$C_{D,pres}$	Integral of gauge pressures on walls
Correction term	$C_{D,cor}$	see main text below
Viscous Drag coefficient	$C_{D,visc}$	Integral of viscous stresses on walls
Total drag coefficient	$C_{D,t}$	$C_{D,pres} + C_{D,visc}$
Total pressure recovery inside duct	σ_d	$\frac{\bar{P}_{t,out}}{\bar{P}_{t,E}}$
absolute total pressure recovery	σ_t	$\frac{\bar{P}_{t,out}}{\bar{P}_{t,\infty}}$
Total pressure recovery at propeller	σ_p	$\frac{\bar{P}_{t,p}}{\bar{P}_{t,\infty}}$
Distortion coefficient	DC_{60}	$\frac{\bar{P}_{t,out} - \bar{P}_{t,60min}}{\bar{q}_{out}}$
Separation	[-]	negative values of wall shear stress in x direction: τ_x

Table 3.3: Evaluation metrics. The subscripts are shown in Figure 3.9 in parentheses.

where:

- \bar{P}_t is the mass-flow averaged total pressure.
- The correction term $C_{D,cor}$ is added to the pressure drag, because the integration of the pressure terms happen exclusively on wall boundaries (which neglects the forces acted on at the domain in- and outlet). The correction term is then equal to:

$$C_{D,cor} = [\text{pressure term}] + [\text{momentum term}]$$

$$= \sum \int_A p \cdot \vec{n} dA + \sum \int_A \rho v_{\perp} \vec{v} dA$$

where the integrals on the domain in- and outlet are computed and summed up⁸. The equation can be further simplified to:

$$C_{D,cor} = \sum \int_A p \cdot \vec{n} dA + \sum \dot{m} \cdot \vec{v}$$

where p and v are the mass-flow averaged quantities. Since the gauge pressure is used for $C_{D,pres}$ and $C_{D,visc}$, the gauge pressure is also used for this term⁹.

- In the equation above, the mass flow rate \dot{m} at the nozzle is equal to m_{cor} , which is a term that originates from a very slight in-continuity in mass flow between the compressor and nozzle. This introduces an inaccuracy in the drag component that would not exist in reality¹⁰. This is accounted for by adjusting both correction terms at the domain inlet based on the percentage difference in mass flow rate:

$$\dot{m}_{cor} = \frac{\dot{m}_{out} - \dot{m}_{in}}{\frac{\dot{m}_{out} + \dot{m}_{in}}{2}}$$

- The entrance is defined as the start of the duct, slightly downstream of the lip as shown in Figure 3.9.
- The 60 ° section of the DC60 metric is equal to any 60 ° section that has the lowest total pressure [48]. This section is determined after calculating the averaged total pressure for the entire annulus with an increment of 10 °.
- It is not convenient to compute σ_p over the entire propeller surface, as the propeller has a radius that is almost equal to one meter and the effect of an inlet on the outer layer would be very small. Therefore, the inner 25 % of the radius is considered instead. Appendix D shows a visualization of this surface.

It should be noted that providing a comprehensive comparison for all provided metrics across all iterations would be considered too extensive. Hence, only notable & relevant differences will be addressed in Chapter 5.

Finally, post-processing plots and contours were generated in either Fluent or Tecplot 360 [50]. Cross-sectional surfaces were generated using the rolling-ball method to illustrate the flow inside the duct.

⁸the sign convention is implemented in the normal vector. Hence, a negative sign will automatically appear when the flow leaves the domain. This is illustrated in Appendix D

⁹note that this does not mean that the correction term, which results in a forward force, and the drag term associated with the walls become comparable, since this is a simplified model where the distinction between thrust and drag are not considered as doing so would be too complicated and meaningless in context of BLI.

¹⁰It has been observed however that the contribution of this term is very small

4

Model Verification

It is imperative to verify the results in order to draw reliable conclusions. In this chapter, a verification study is presented.

4.1. Sources of Uncertainty

The geometry is verified by inspecting curvature combs of the b-splines to ensure smooth transitions and by visualizing zebra stripes in Solid Edge to check for G1/G2 tangency relations with respect to adjacent faces.

The quality of the mesh is verified by examining the Jacobian, area/volume ratio, skewness angle and y^+ value. Figure 4.1 shows that the y^+ -value of the cells on all surfaces lie within an acceptable range ¹

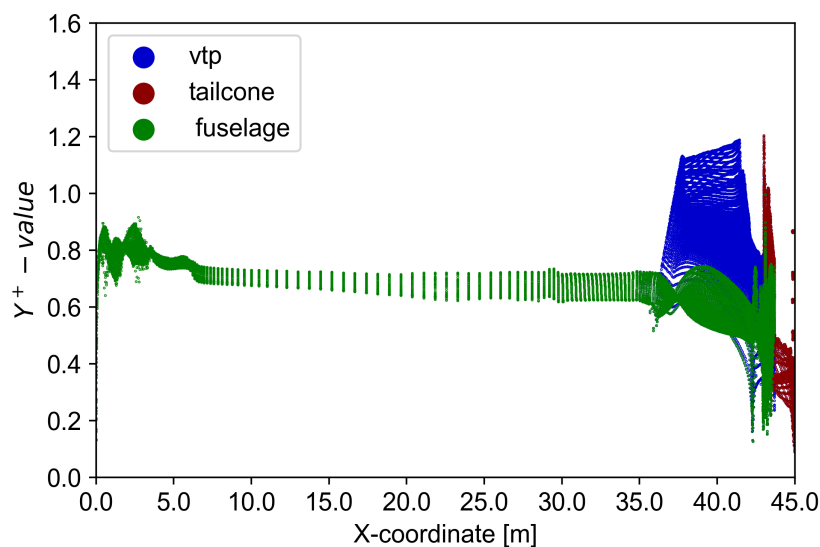


Figure 4.1: Scatter plot of y^+ values for HA-V3.

Multiple sources of errors exist in a CFD simulation, but round-off errors, iterative errors and discretization errors are the primary components of numerical inaccuracies in CFD [51].

Round-off errors are caused by computers when rounding off floating numbers. Though dependent on the machine, this type of error is not significant compared to the other types, because double precision

¹Although a value lower than one will not harm the simulation, other than over-resolve and increase computational costs, a value slight higher as seen in Figure 4.1 is also acceptable, as long as the y^+ value does not exceed two. Otherwise, the boundary layer is resolved with a too coarse mesh.

is enabled in Fluent for increased accuracy.

Iterative errors are introduced as the set of algebraic equations is solved iteratively. The simulation is cut off at a certain point once convergence criteria are met, but this solution differs from the fully converged solution. In order to minimize this error, the residuals of the equations are plotted and the solution is considered converged once all residuals are settled at a sufficiently low value. Thereafter, to determine the convergence with more certainty, important flow variables such as P_t at the compressor and C_D are monitored for the last 500 iterations, and the respective standard deviations are verified to be less than 1 %. An example is shown in Appendix C.

Discretization errors are the largest error in CFD which arise from discretizing the flow domain into a finite amount of cells as the set of algebraic equations is approximated. A finer mesh, particularly at high flow gradients, decreases the numerical error and approximates the precise analytical solution of the system better. In that regard, a grid convergence study has been performed and will be presented in the next section in order to approximate the discretization error.

4.2. Grid Convergence Index

In the grid convergence study a total of three successive meshes were constructed with a refinement ratio of 1.5. The surface domains were refined using a script provided by Pointwise [52], which automatically refines all connectors uniformly whilst maintaining node distributions. The unstructured domains and blocks were further refined wherever necessary by decreasing the maximum cell size in order to closer match the global refinement ratio of 1.5². The procedure that is recommended by Celik et al. [53] is used to determine the discretization error of the simulation results. For convenience, the study has only been carried out for the last geometry. Table 4.1 shows the mesh parameters.

Mesh	Number of cells N (10^6)	Refinement ratio	grid size h	$C_{D_{raw}}$ ^a [counts]	σ_t	
i	coarse	8.99	-	3.07	47.82	0.782
ii	medium	30.42	1.5	2.05	47.39	0.783
iii	fine	103.21	1.5	1.36	47.13	0.780

Table 4.1: Three grid resolutions with the corresponding values. The coarse grid (highlighted in color) is used as the base mesh for all iterations in the thesis.

^athe subscript *raw* highlights that the correction term has not been implemented yet; the drag term consists of the pressure and viscous terms on all walls.

Table 4.2 shows the results of the grid refinement study. The associated plots are demonstrated in Figure 4.2. the approximate error e_a and extrapolated error e_{ext} are defined as [54]:

$$e_a = \left| \frac{\phi_1 - \phi_2}{\phi_1} \right|$$

and

$$e_{ext} = \left| \frac{\phi_{ext} - \phi_2}{\phi_{ext}} \right|$$

It becomes evident that there exists a large discrepancy between the theoretical and apparent order of the method. This may be caused by non-uniform grid refinements locally, or inaccurate implementation of the order of the scheme due to settings such as choice of boundary conditions and numerical model [55]. The Grid Convergence Index (GCI) is a measure of how far the value is off from the 'accurate' solution³ which is achieved with an infinitely small mesh where discretization errors are eliminated. The accurate solution in turn is calculated using Richardson's extrapolation which estimates this value

²This means that the refinement for unstructured domains is not entirely uniform. Also, in some cases the desired refinement could not be achieved, such as for the near field blocks, because decreasing the maximum cell size by too much resulted in a deteriorated mesh.

³which eliminates discretization errors, but there may still be an error of some amount that exists with respect to the true physical solution.

by observing the rate of change of the variable between two grid sizes whilst accounting for the apparent order p_{app} of the method. As the grid is refined, the value approaches this solution asymptotically. Observing Table 4.2, although at first a low GCI is visible, which indicates that the solution is well approximated, the ratio of GCIs is not close to 1, which means that the solutions do not lie within the asymptotic range. Furthermore, Figure 4.2 shows non-monotonic convergence, where σ_t shows oscillatory convergence. This can be problematic, as it suggests that the mesh used in the thesis might not yield accurate results. Therefore, it is imperative to investigate the root cause of this issue.

	C_D	σ_t
Theoretical order p	2	
Apparent order p_{app}	1.26	4.39
exact value (h=0)	46.75	0.780
e_a [%]	0.55	0.3
e_{ext} [%]	0.82	0.05
GCI_{fine} [%]	1.02	0.07
GCI_{coarse} [%]	1.7	0.01
ratio of GCIs	2.77	1.29

Table 4.2: Grid Convergence Parameters. The values given are calculated for the fine mesh (subscript 1)

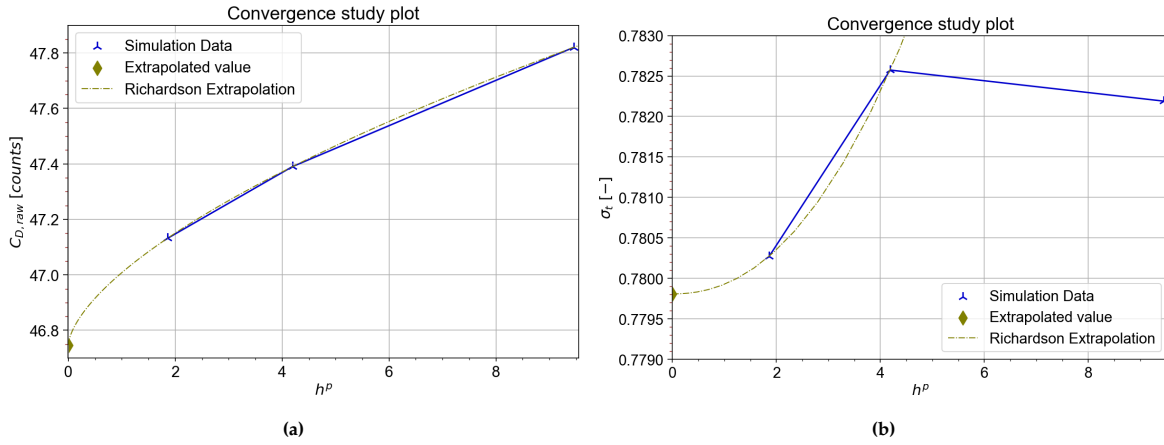


Figure 4.2: Plots of mesh convergence with Richardson extrapolation using the apparent order p_{app} . The horizontal axis uses the theoretical order p . As p_{app} is significantly different to p , the extrapolation is (highly) curved.

4.3. Comparative Analysis of Mesh Resolution

In case the difference of a certain flow variable is shown, the coarse solution is subtracted from the fine solution as follows: $\Delta\phi = \phi_{fine} - \phi_{coarse}$

Figure 4.3 shows contours of difference in skin friction coefficient ΔC_f between the fine and the coarse mesh. The contours are generated by interpolating the coarse mesh (mesh i) onto the fine mesh (mesh iii) in Tecplot, and afterwards calculating the difference in flow variable (in each cell) between the fine and interpolated mesh. Figure 4.3a shows regions around the stagnation point that show a considerable difference between the fine and coarse grid. Surface shear lines of the coarse mesh are superimposed. While the streamlines stem from the coarse mesh solution, both resolutions demonstrate the same stagnation line, so the differences are not caused by a shift in the stagnation point, but rather a difference in magnitude of the shear stresses. The streamlines show a high amount of transverse movement. Observing the coarse mesh that is overlaid in Figure 4.3a, the spacing appears too large in this direction, which explains the high differences that is observed close the stagnation line. Figure 4.3b supports this argument, as the increased grid spacing appears to reduce the disparity.

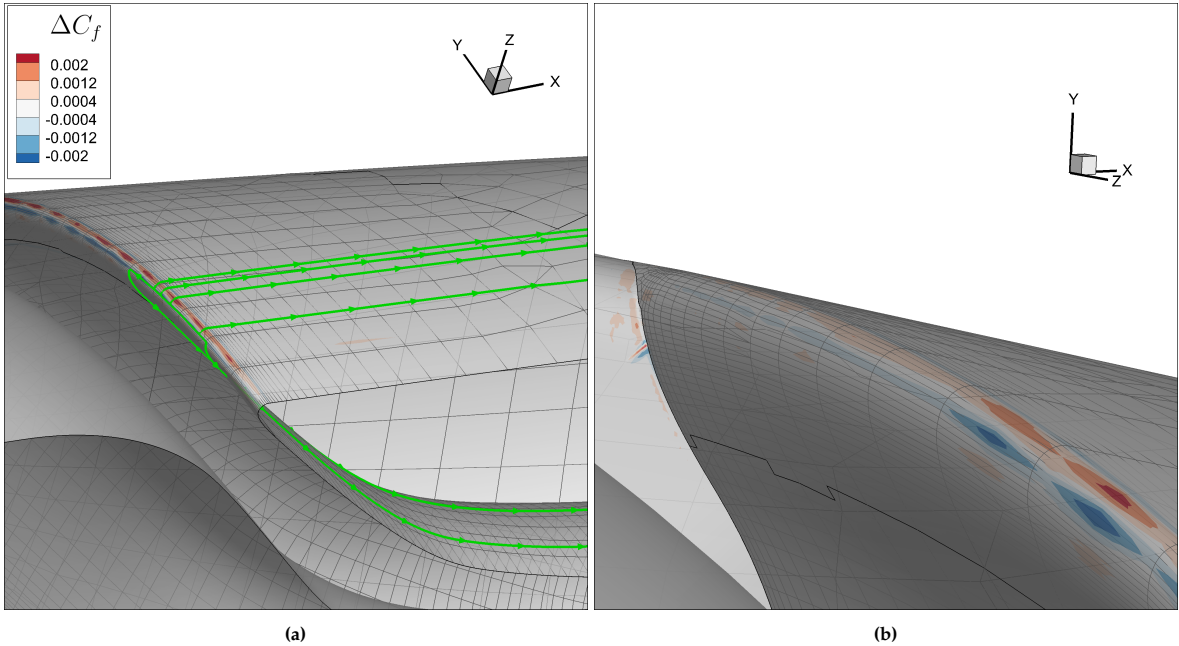
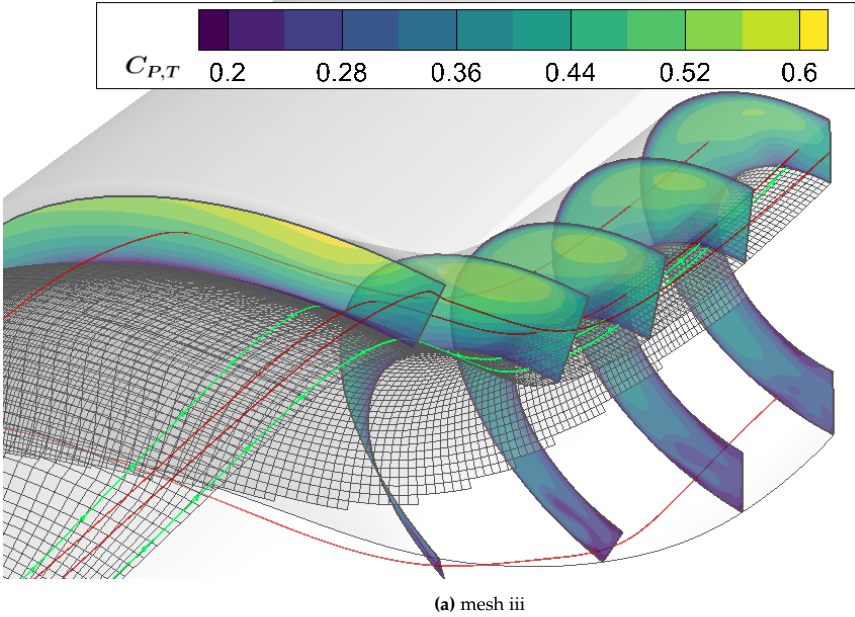


Figure 4.3: Contours of ΔC_f between mesh iii and mesh i for HA-V3. Negative values indicate a lower C_f for the finer mesh ⁴

The same procedure is followed for the total pressure coefficient and is illustrated in Figure 4.4. The most remarkable difference is the accumulation of the boundary layer that develops on the inner duct surface.



⁴The disparity on a small region on the sidewall in b) is due to a geometry deviation of the mesh. Later on in the thesis, it was noticed that smoothing out this part had a minute effect on the results.

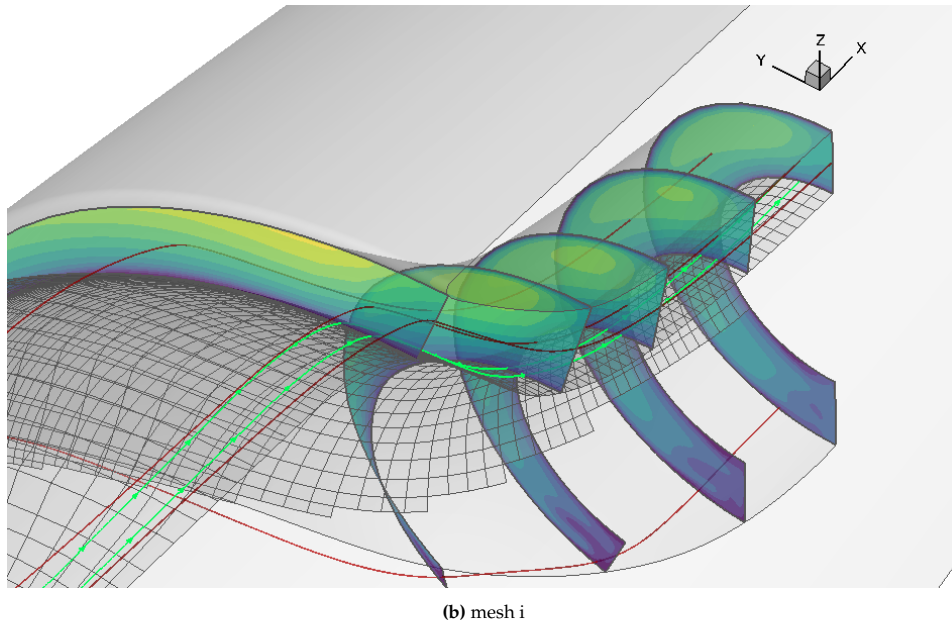


Figure 4.4: Contours of total pressure coefficient. Streamlines very close to the surface are displayed in green, while the ones in the interior are shown in red.

The streamlines show a distinct difference between the extent of cross-flow that occurs: the fine mesh better resolves the flow in this direction. The streamlines at higher azimuthal angles show a much higher amount of similarity between the two cases, where the cross-wise grid spacing is tighter.

Lastly, another difference originating from an increase in mesh resolution is displayed in Figure 4.5. Figure 4.5 reveals that there is a notable difference in the wake of the vertical tailplane. At a distance of $Y = 30\text{mm}$, where the wake is less in magnitude, the finer mesh shows a smaller difference.

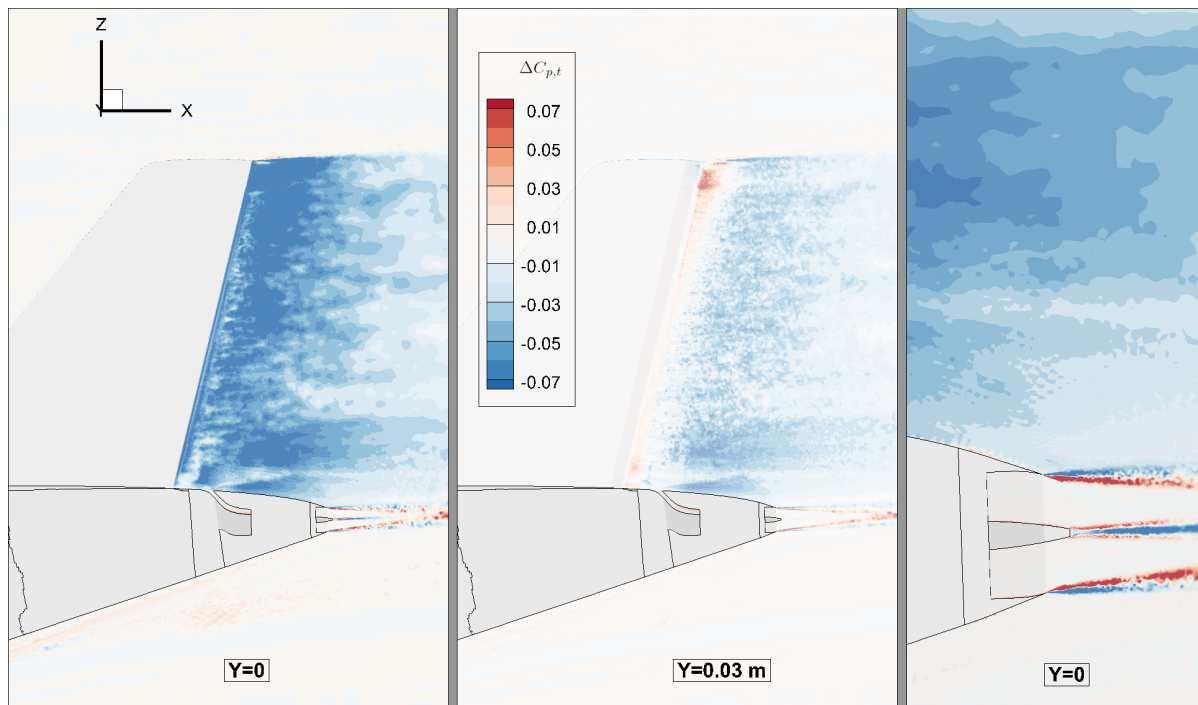


Figure 4.5: Differences in total pressure coefficient at the symmetry plane (left) and a slice at $y = 0.03\text{ m}$ (right).

The findings and their impacts can be summarized below:

- The wake of the vertical tailplane along with the azimuthal direction of the duct surface are meshed too coarsely, resulting in the fact that the flow is insufficiently resolved, which presumes that the cross-flow that happens due to the velocity difference between the wake of the vertical tail and the surrounding faster-moving air is not captured by the coarse grid spacing, causing an inaccuracy in P_t readings.
- For the same reason, the skin friction coefficient C_f is remarkably different on a thin section slightly upstream and downstream of the stagnation line of the lip. Since the drag is proportional to the friction coefficient, this causes an inaccuracy in C_D readings.
- The region near the trailing edge of the tailcone is insufficiently meshed as well, which is caused by the mixing that occurs in flow, stemming from the large velocity difference between the jet air and surrounding wake of the tailcone. However, this will not have an impact on the intake performance.

As the discrepancy that is perceptible is manifest within the duct, this unfortunately signifies that the total pressure recovery is also affected. Hence, it must be noted that the results shown in the next chapter contain systematic errors. The GCI provided in Table 4.2 must be taken carefully into consideration. However, this does not necessarily mean that the results provided in this thesis are invalidated. This is further supported by the fact that the contours shown in this section, which highlight the causes of inaccuracy, were similar in all iterations. As an example, the boundary layer accumulation in Figure 4.4 was not observed for any of the design iterations, which means that the error is affecting all designs. This is most likely because the mesh is constructed roughly in the same manner for all designs⁵.

Estimation of Error

In this section, a method is demonstrated to estimate the error of the results. The goal is to determine how much of the differences that were observed in the previous section are due to non-systematic deviations, and to assess how significant these deviations are.

The following methodology has been employed:

1. As before, interpolate the coarse on the fine data and compute the difference: $\Delta\phi = \phi_{fine} - \phi_{coarse}$ where ϕ is the flow variable C_f or $C_{p,t}$.
2. filter the data. Since the interpolation described in the point above contains large errors at certain parts of the domain, it is necessary to remove or filter away the corrupted data. Section C.3 clarifies the reason and region where this procedure has been performed.
 - The following three steps divide the data into three types, where each type is given a symbol: $\Delta\phi_{nom}$, $\Delta\phi_{tol}$ and $\Delta\phi_{exceed}$, where the first two categories represent the data range where differences are considered acceptable, whereas the last one signifies differences in flow variable that are due to non-systematic errors. A thorough explanation for each is provided below.
3. Determine the nominal change in flow variable: $\Delta\phi_{nom}$. That is, as the mesh is refined and assuming an initial mesh that is within the asymptotic range, the flow variable is expected to increase/decrease homogeneously throughout the region of interest, which is explained by the reduction in discretization error. Since the mesh in this study, however, does not lie within the asymptotic range, certain regions may show an abundant increase/decrease. Therefore, $\Delta\phi_{nom}$ consists only of the part or section of the region of interest where the contours of the fine and coarse mesh look similar, i.e. where the sources of inaccuracy are absent and the coarse mesh is sufficiently fine, such that an increase in mesh resolution does not lead to a different flow field. Consequently, this region is determined by inspecting the solutions of the fine and coarse mesh of the respective domain and identifying a region where the contours appear (very) similar. E.g., in Figure 4.6a the value of $\Delta\phi_{nom}$ is determined close to and around the midplane, since this part shows reasonable agreement between the two mesh sizes.

⁵That is, the cells in azimuthal direction (and in the wake of the tail plane) are meshed in the same method for all HA designs. The only exception is the FA design has a tighter grid spacing in this direction, which means that there exists an inconsistency in the comparison between FA and HA design.

4. Determine the part of the domain where the deviation on each cell exceeds this nominal value, and hence is larger than $\Delta\phi_{nom}$, but is still considered 'tolerable'. So, a certain tolerance $\Delta\phi_{tol}$ is applied that acts as a relaxation factor, meaning that not all data that exceeds the nominal value is immediately considered to be non-systematic, but the tolerance increases the margin of $\Delta\phi_{nom}$ by some acceptable amount. This amount is defined as follows:
 - for $C_{p,t}$ it is determined as .5% of the ambient total pressure, since a value too low would have a minimal effect, whereas at the same time Figure 5.1 depicts that the designs exhibit very similar values.
 - for C_f , the tolerance is not applied, since the differences between designs are extremely close in Figure 5.2, which would make it difficult to pick a sensible value for the tolerance.
5. Determine the portion of the total domain where the difference in flow variable is 'excessive': $\Delta\phi_{exceed}$. In other words, determine where the differences in flow variable simply exceed the tolerance (step 4) of the nominal difference (step 3), i.e. where $\Delta\phi_{exceed} > (\Delta\phi_{nom} + \Delta\phi_{tol})$. The total area where this equation holds, A_{exceed} , consists of an area where differences in the flow variable are due to a too coarse mesh, representing a non-homogeneous or non-systematic deviation from the nominal change (plus the tolerance). To account for the weight of each cell, $\Delta\phi_{exceed}$ is the area-averaged deviation of the flow variable on A_{exceed} , which is a measure of the deviation with respect to the tolerance of the nominal difference. As area-weighting has been performed, the deviation is as a result a single value.
6. Report the fraction of the total domain that consists of non-systematic deviations: $A_{ratio} = \frac{A_{exceed}}{A_{total}}$
7. Calculate and report the extent of the deviation, by comparing the area-averaged deviated values to the nominal difference: $\delta = \frac{\Delta\phi_{exceed} \cdot A_{ratio}}{\Delta\phi_{nom} + \Delta\phi_{tol}}$. So, δ is measure of how much of the differences between fine and coarse mesh are due to a non grid-convergent mesh that will affect the accuracy of the results negatively.

The above procedure is applied at the compressor face for P_t and at the tailcone surface⁶ for C_f . Table 4.3 shows the results.

	$C_{p,t}$	C_f
$\Delta\phi_{nom}$	$[0, -1.2 \cdot 10^{-2}]$	$[0, 8 \cdot 10^{-4}]$
$ \Delta\phi_{exceed} $	0.016	$6 \cdot 10^{-4}$
A_{ratio}	0.22	0.1
δ	20.5 %	10.1 %

Table 4.3: Estimation of error

The procedure is illustrated in Figure 4.6. The largest discrepancy is the earlier described phenomenon at the top section of the compressor. Although a deviation of 20.5 % is not negligible, the data filtering process (described in step two) does not completely eliminate all defective data. Therefore, this number is likely an overestimation.

⁶which consists of the outer duct surface and fuselage skin connected to it downstream. Figure 4.7 illustrates the tailcone domain.

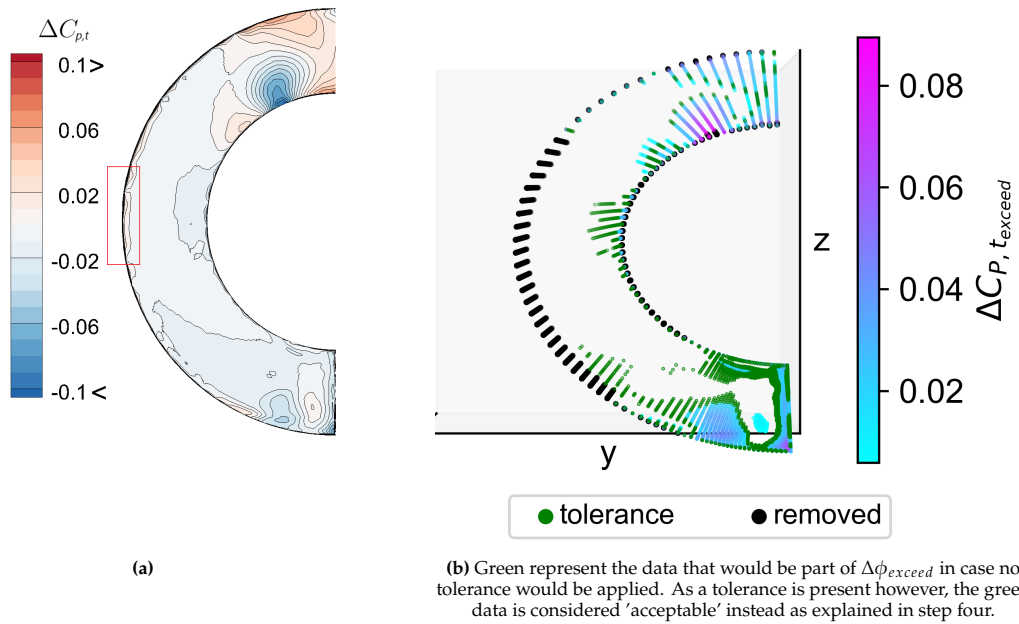


Figure 4.6: Illustration of error estimation method. The data is filtered in b) to minimize the impact of corrupted data on the study, refer to Appendix C for an elaboration, where Figure C.5 provides a close-up of the red box in a).

The results for C_f are shown in Figure 4.7.

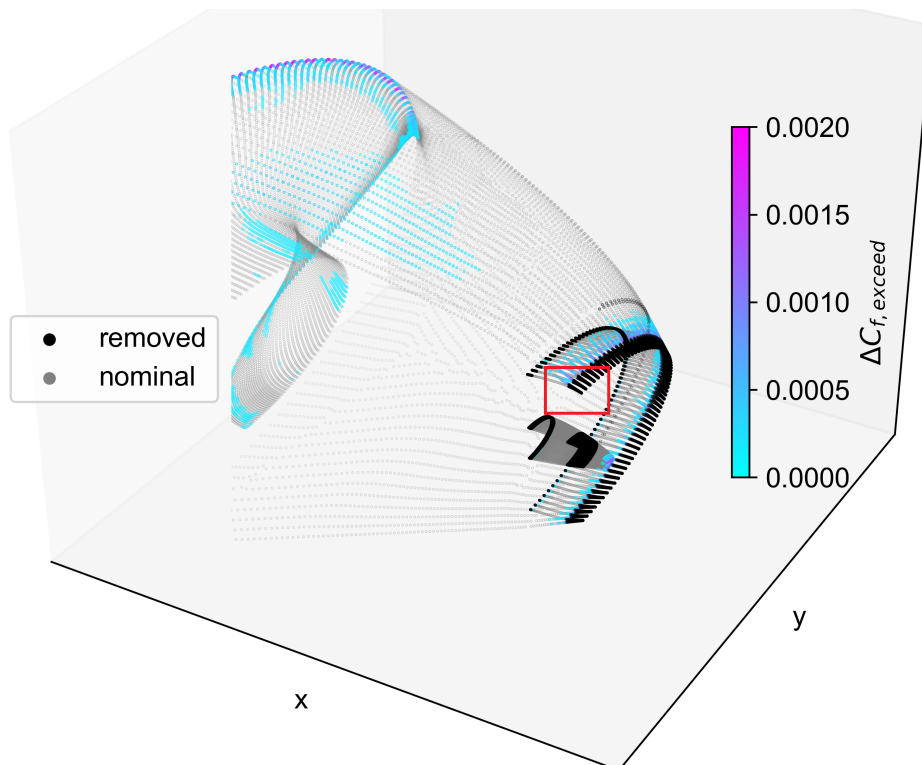


Figure 4.7: Figure C.4 provides a magnified view on the rectangular zone in red which clarifies the rationale behind filtering out this part prior to implementing the error estimation method.

In summary, in this section an attempt is made to quantify the error that is noticed in the grid convergence study. The estimated error that is calculated for both $C_{p,t}$ and C_D is not a negligible amount: of the total changes, the changes due to increased mesh resolution **caused by non-systematic errors** are

approximately 21% and 10% respectively. Consequently, the results in the next chapter contain a deviation from the accurate solution, i.e. the solution in case the mesh was sufficiently fine, which thus cannot be overlooked. However, as explained previously, the discrepancies are manifest through all designs. Therefore, a comparative analysis is still useful, but for more accurate values the mesh must be refined. Furthermore, flow phenomena that will be shown in the next chapter would still be manifest with a finer mesh, though possibly with (slightly) different magnitude and characteristics. Nevertheless, the implemented geometrical changes show a notable difference in the flow field. Therefore, relevant conclusions can be drawn into how the geometric changes affect the flow field, ultimately allowing to answer the research question.

4.4. Alternative Differential Scheme

At first, it was realized in a simulation within the APPU project, that changing from least-squares cell-based Roe-FDS to a green-gauss cell-based AUSM spatial discretization scheme & flux type in Fluent significantly improved the mass-flow conservation between an actuator disk that was inserted at the location of the propeller. After applying the same modifications in settings to this thesis and monitoring the mass flow rate of two closely placed surfaces for several hundred iterations (after convergence was achieved), it was observed however that the difference in mass flow rate oscillates around roughly -0.0115 kg/s for both cases. As such, the same improvement was not detected in this study. Nevertheless, another notable difference was observed: the pressure recovery decreased from 78.3 % to 78 % for one of the designs. In some cases where separation occurs, the flow field can look different as demonstrated in Figure 4.8.

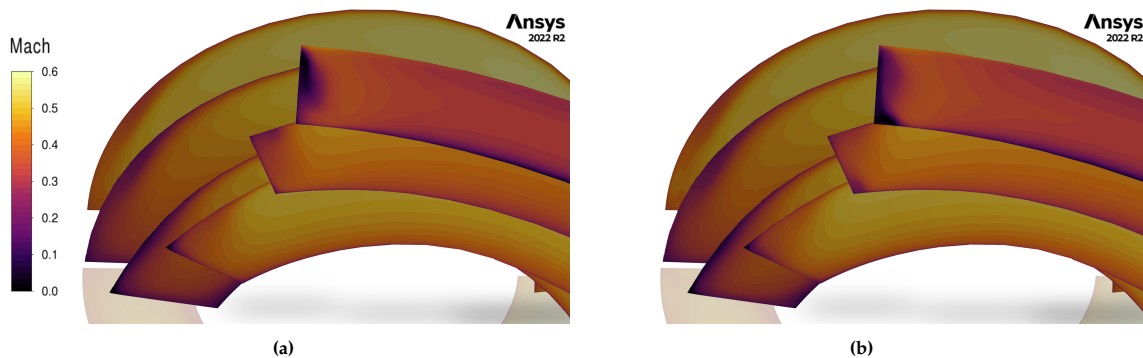


Figure 4.8: Mach contours at cross-sectional surfaces in the duct for Roe-FDS & least-squares (a) and AUSM & Green-Gauss (b). The foremost surface represents the inlet entrance where the most notable change is visible.

The GCI was computed again to check whether a more successful convergence would be achieved. However, the GCI for C_D is now close to 18 %, which is much inferior to the previous computation⁷. So, more investigation is required into which solver settings ought to be used for more accurate results, such as by researching literature or performing a validation study. Nonetheless, it seems that the original settings result in a lower total pressure recovery. From that angle, it is more conservative to implement the original settings.

⁷The reader is referred to Appendix C for a complete overview of the GCI parameters.

Results & Discussions

An aerodynamic analysis of the CFD results is presented in this chapter. At first, an overview of the relevant metrics is provided. Next, the area distribution as discussed in Chapter 3 is presented for each design. Then, the effect of various geometric parameters on the flow field is discussed. Last, a discussion on the practicality of creating the geometry is provided.

5.1. Overview of Quality Metrics

Figure 5.1 shows the total pressure recoveries. As the thick boundary layer carries a low energy content compared to under-wing podded engines, the total pressure recoveries are relatively low. And albeit the HA design shows improvements compared to FA, the values could overall not exceed a value of 80%. Nonetheless, the duct performance is very close to unity even in cruise, achieving losses lower than 1%, which suggests that most losses take place outside of the intake and are caused by the boundary layer air.

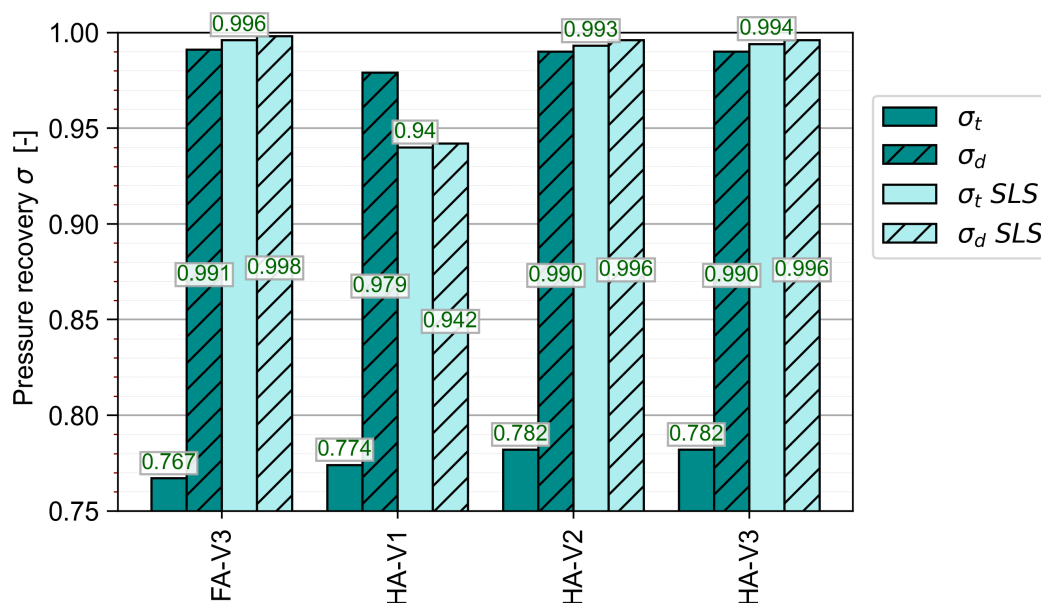


Figure 5.1: Overview of total pressure recoveries at the compressor.

Figure 5.2 shows the drag coefficient of the various designs. Although a clear difference originating from surface wall boundaries is apparent, the largest contributor stems from the correction factor as the APPU core generates a large forward force on the air frame.

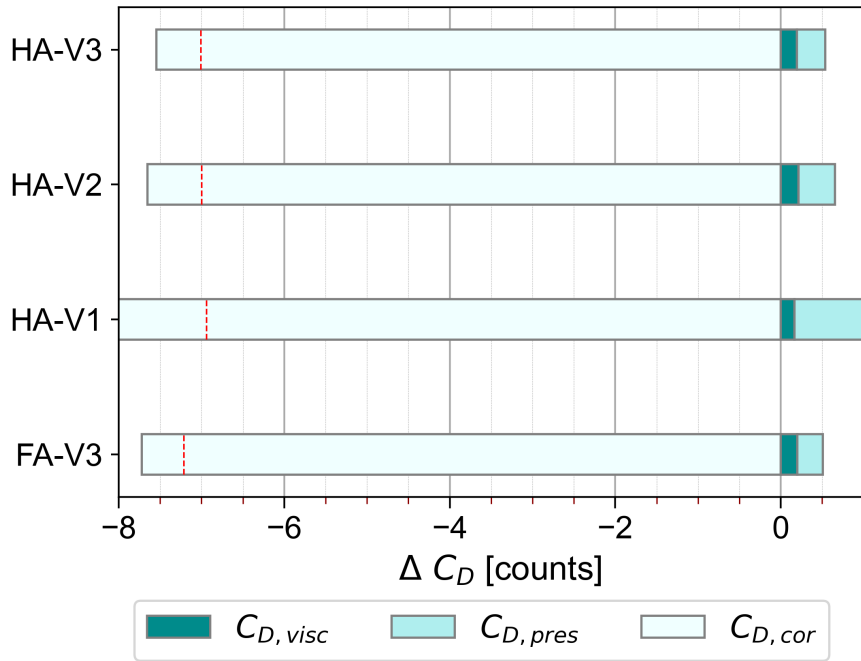


Figure 5.2: Overview of drag coefficients with respect to the base configuration. The red line represents the total drag coefficient $C_{D,t}$.

Figure 5.3 displays the distortion coefficient $DC60$. It is apparent that the distortion coefficient at cruise is around 0.02 and shows little variation with respect to the various designs, with the exception of HA-V1, which displays a case of severe distortion. At SLS, a boundary layer of the incoming air is absent, resulting in a far more uniform profile on the compressor face and in turn a lower distortion factor.

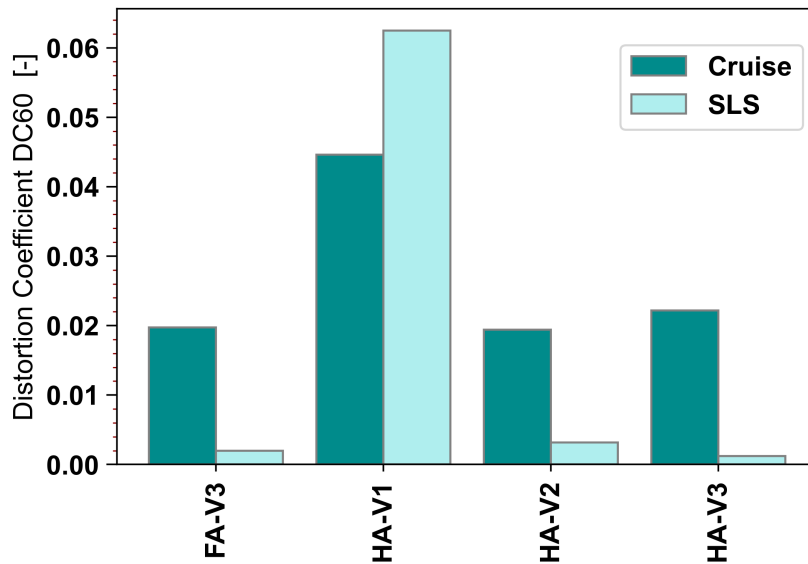


Figure 5.3: Overview of distortion coefficient $DC60$ at the compressor.

Furthermore, since for FA-V1 and FA-V2 the outdated values of mass-flow rate and compressor area were used - and mass flow continuity between domain in- and outlet was not yet achieved - the quantities are displayed separately in Table 5.1.

	FA-V1	FA-V2
$C_{D,visc}$ [counts]	40.37	40.40
$C_{D,pres}$ [counts]	6.73	6.63
σ_d [%]	99.3	99.7
σ_t [%]	77.6	77.0
DC60	0.0224	0.0188

Table 5.1: Values of some performance metrics for FA-V1 and FA-V2 at cruise condition.

Lastly, the boundary layer thickness¹ at the location of the intake is equal to 0.87 meters. An illustration of the BL follows in Appendix D.

5.2. Area Distribution

Figure 5.4 shows the relevant area distributions of designs using the rolling-ball method.

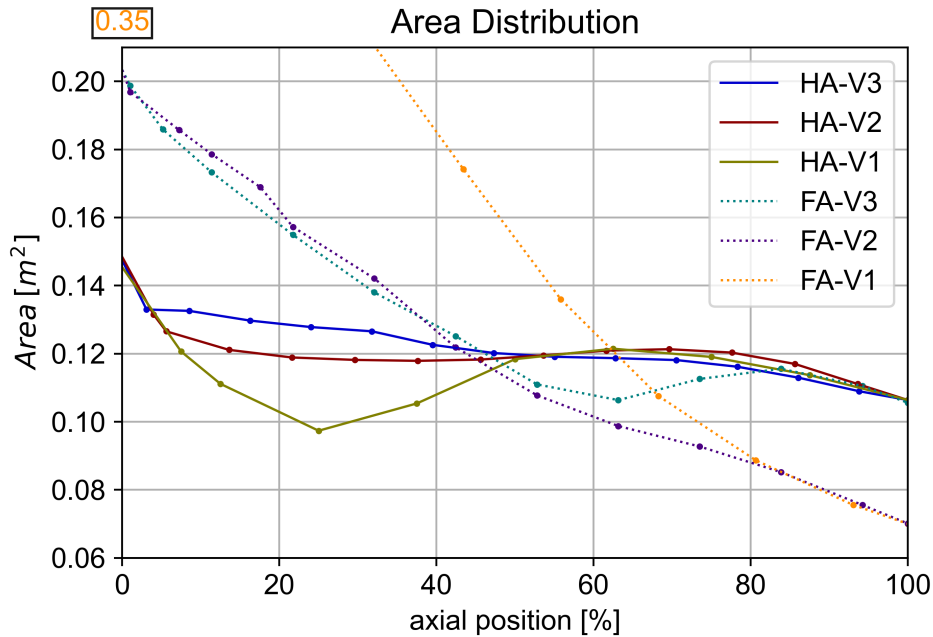


Figure 5.4: Area distribution of the geometries. The value at 0% for FA-V1 is given in the text box to increase readability.

It should be noted that the area distribution has been used as a tool exclusively to design the last two (HA-V2 & HA-V3) iterations. The preceding iterations were not constructed by incorporation this area graph. Nonetheless, the area distribution still proves useful to explain changes in the flow field.

Because the mass flow rate of the engine is specified and fixed and the conservation of momentum (Equation 5.1) holds, this implies that the area distribution is directly related to the velocity distribution; an increase/decrease in area diffuses/accelerates the flow respectively. As will become apparent in the discussions in the next section, this plays an important role in intake design.

$$\dot{m} = \rho v A \quad (5.1)$$

5.3. Effect of Geometric Parameters

Below, each section isolates and discusses the effect of a single geometric parameter on the flow field. As discussed in Chapter 3 each iteration incorporates multiple design changes. So, in order to avoid confusion, it should be clarified that some (or perhaps most) designs may appear in more than one subsections. Moreover, for the sake of clarity each figure in this section is labelled with the corresponding geometry version.

¹the edge of the BL is specified at 99 % of the freestream total pressure

In the explanations below, the terms 'inner' and 'outer' duct surface are often mentioned. The definition of these terms were previously shown in Figure 3.3. Moreover, legends are shared between figures.

5.3.1. Entrance Thickness

Figure 5.5 shows the Mach number contour on the symmetry plane. It is clear that the entrance of the first geometry, FA-V1, is too wide, resulting in excessive diffusion, which in turn leads to separation caused by the high adverse pressure gradient. To reduce this negative effect, the entrance was made smaller for FA-V2. That is, because for a thinner entrance the inlet capture ratio would be lower, resulting in a lower adverse pressure gradient. Figure 5.5 confirms this hypothesis: the separated zone is much reduced. Another observation is that the separated region at the lower section is larger in both cases. This is caused by the non-axisymmetric shape of the fuselage; the vertical distance to the engine middle line is roughly 19% larger for the bottom side. On top of that, the firewall is orientated at a 7.8° angle with respect to the vertical. Both of these factors lead to a reduced horizontal space towards the compressor face. Therefore, the initial bend is stronger, resulting in a higher positive pressure gradient.

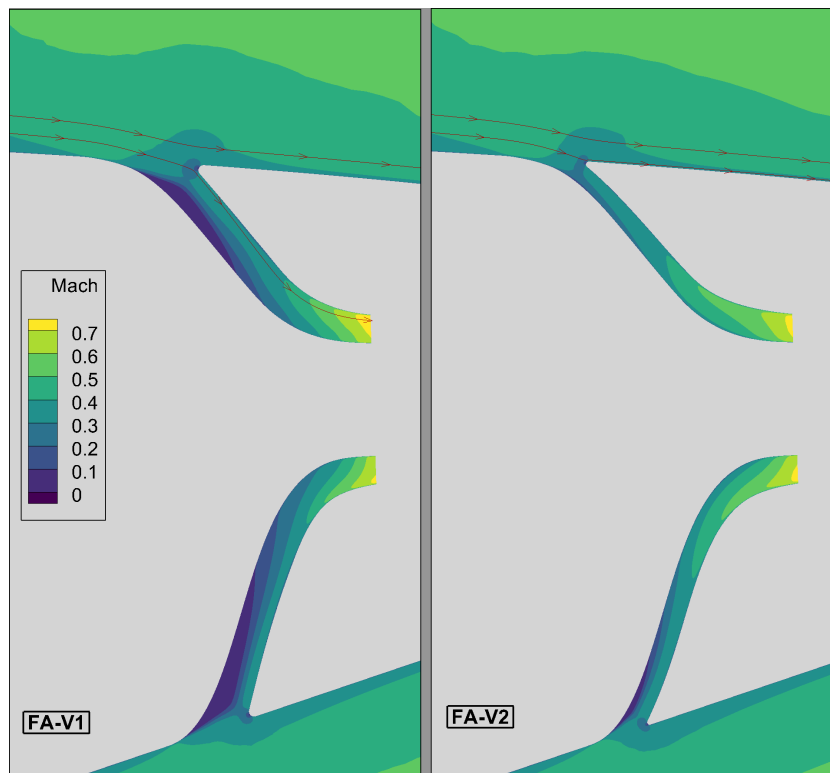


Figure 5.5: Mach contours on the symmetry plane highlighting the effect of varying the inlet thickness. In non-dimensionalized units, FA-V1 corresponds to a $\frac{b}{D}$ of 9.9, whereas FA-V2 has a value of 19.3.

Examining the flow field in Figure 5.6 reveals that there is a high amount of separation present at the midplane for FA-V1. Though Figure 5.5 shows that though there is little separation on the symmetry plane for FA-V2, a significant amount of separated flow is still present, especially close to the midplane. Upstream fuselage sections show that the velocity profile is highly non-uniform; the boundary layer seems to accumulate at the lower segment of the fuselage as the mean velocity at that section is lower. This happens due to the nature of flow over an inverted tail cone at incidence, causing the boundary layer to cross-flow from the top to the lower part of the cone, where the boundary layer eventually accumulates. This takes place due to the tendency of slower-moving air to react stronger to induced pressure gradients than high velocity flow. A reason for the large separation zone could be coupled to this cross-flow of the boundary layer, which causes a non-uniform total pressure profile as shown in Appendix E. At sections where the total pressure is higher, the flow carries more energy content to overcome the adverse pressure gradient. Nevertheless, a thinner entrance with the same engine operating conditions creates a higher suction force downstream of the entrance, which in turn helps the flow to stay attached for longer.

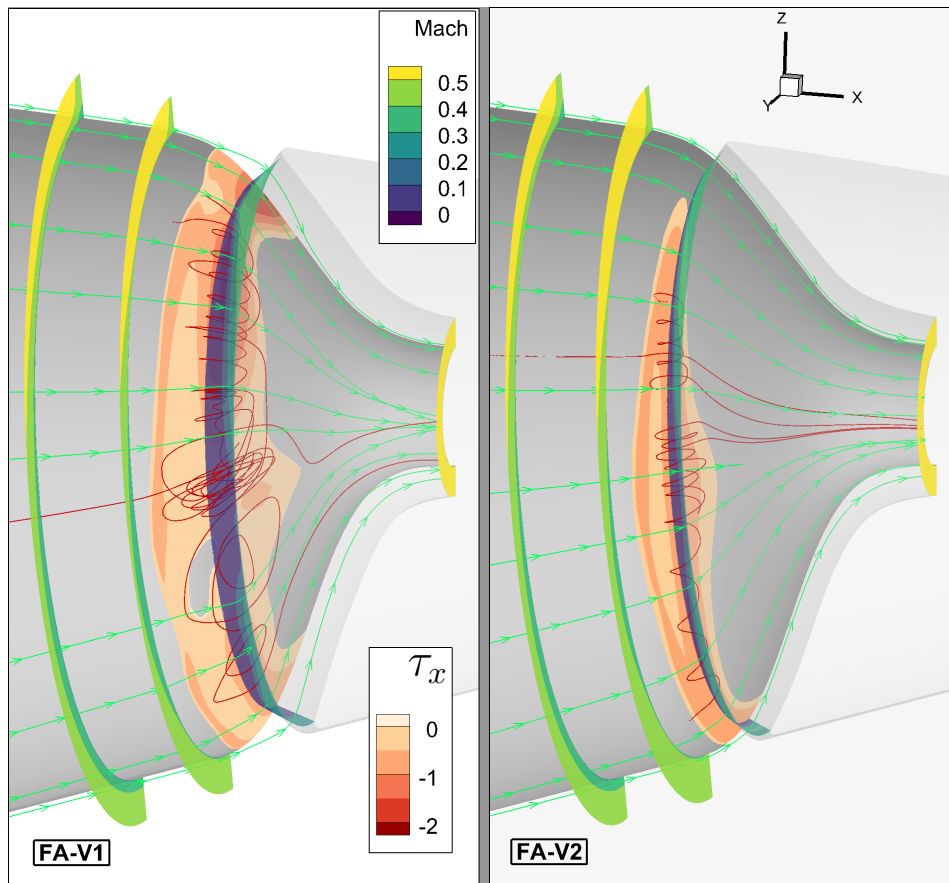


Figure 5.6: Visualisation of the effect of inlet thickness in 3D. Red streamlines show the circulation region, whereas green streamlines show attached flow.

Surprisingly², the losses for FA-V2 up to the intake entrance are 0.46 % higher. This is caused by the fact that a thicker entrance area allows air from higher up in the BL profile to be ingested into the engine, which carries a higher energy content. In theory, this concept would be incorrect as the mass flow rate of the engine is fixed, which means that in both cases the ingested air flow would be the same. The impact of a reduced entrance area would then be reduced to the amount of diffusion that takes place. However, it is shown in the figures above that separation plays a significant role in this diffusion. A large separated region contains flow that recirculates and that is not ingested into the engine, causing air from above it to enter, which does have a higher total pressure. This explains the fact that FA-V1 shows lower losses up to the entrance. This is further supported by observing Figure 5.7; as shown by the streamlines, where previously the bottom streamline would enter the engine, it now flows around the intake for FA-V2. Moreover, the losses inside the duct are only lower by 0.42 % for FA-V2. Considering the higher losses at the entrance, this indicates that the FA-V2 overall performs worse in terms of σ . This phenomenon can be explained by observing the area distribution of both designs. The area ratio $\frac{A_E}{A_{out}}$ is much higher for FA-V1: 5.0 as compared to 2.9. This results in a very steeply converging area distribution. So, the losses inside the duct of FA-V1 with respect to FA-V2 are much less pronounced, as the converging nature of the duct evens out the non-uniformities and improves the quality of the flow.

Hence, it is apparent that there is a certain trade-off in designing this parameter. On the one hand, reducing the inlet thickness greatly reduces detrimental flow behavior. On the other hand, a higher entrance thickness increases the ingested total pressure and results in a more converging duct, partly mitigating its drawbacks. Moreover, the DC_{60} for FA-V2 is at a value of .019, 16 % lower, which means that a reduced entrance thickness is favorable in achieving more uniform flow.

²This is because FA-V2 was expected to show lower losses due to the findings in this section, particularly since the separated region inside the duct is much reduced

5.3.2. Azimuthal Extent

Initially, during the thesis it was argued that a FA design in this context is not a suitable intake due to a hazard at a potential tail strike, where there is a possibility of metal scrap being ingested into the intake. Therefore, the azimuthal 360° range of the FA design was reduced to a 180° HA design, where the intake consists of a slot on the top segment of the fuselage surface. Despite the initial motive for this design change, it also facilitates an aerodynamic investigation of an additional geometric design parameter.

It should be mentioned that the comparison is made with a HA version that has an increased intake length. When comparing to HA-V1, which has the same intake length as FA-V3, it immediately becomes evident that the FA design is far superior³. The HA-V1 design displays much steeper pressure gradients. A cause for this is the aft-moved lip, as the lip was initially moved aft⁴ in axial direction by 50% compared to FA-V3. A side effect of this is a reduced axial distance of the outer duct surface towards the compressor face. Appendix E shows a comparison with HA-V1, and more detail on HA-V1 is provided in Section 5.3.3.

Figure 5.7 shows a comparison on the symmetry plane. As confirmed in Figure E.6, the total pressure ingestion is increased for the HA design as shown by the streamlines. The drawbacks of the lower section, as discussed previously in Section 5.3.1, are eliminated as well. Finally, the boundary layer close to the compressor surface is thinner as the curvature is more gradual, though this is due to the increased intake length.

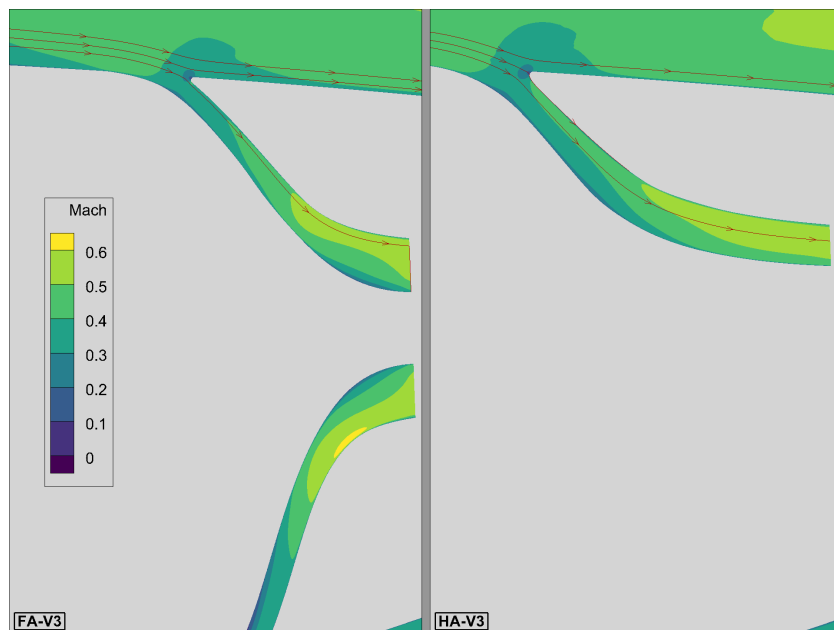


Figure 5.7: Mach contours of the two different intake designs.

Figure 5.8 and Figure 5.9 show pressure coefficient contours on the individual duct surfaces. The FA design displays a much more symmetric contour profile. The streamlines show lower tendency to flow in azimuthal direction and enter the compressor in a much more axially aligned manner. The separated region shown in Section 5.3.1 is characterized by relatively high static pressure values, since the flow slows down completely. On the other hand, the large 'dead zone' of separated flow is fully eliminated for the HA design, which is presumably due to the fact that more air is drawn from the outside layer of the BL air that has more energy content to stay attached. However, particularly close to the sidewall, as the geometry has curvatures in both axial and transverse direction, pressure gradients are stronger in this region. On top of that, as the flow progresses in azimuthal direction, the boundary layer accumulates

³This is not a conclusion that follows by necessity, but rather is only limited to what is observed in this study. As will be discussed later, the geometry definition also contributes to its declined performance

⁴This in order to maintain roughly the same MFR; as the entrance of FA-V3 showed a satisfactory diffusion, the lip had to be moved aft to achieve the same capture ratio, as the upstream air tube would increase in thickness for a decrease in azimuthal extent due to the same mass flow requirement. However, the BL velocity profile is not linear. Therefore, the increase in entrance thickness should be less than the decrease in azimuthal extent.

in this area. This transverse flow is caused by the static pressure variation in azimuthal direction. This phenomenon is in line with the geometry definition, as the shape grows in azimuthal extent (i.e. extends from 180° at the entrance to 360° towards the compressor face), where the flow has to fill up the vacuum that is created. The effect of this is evident in Figure 5.10, where a region of slow-moving air is accumulated. Therefore, unlike the FA design, the pressure contours are more varying as the sidewall is approached.

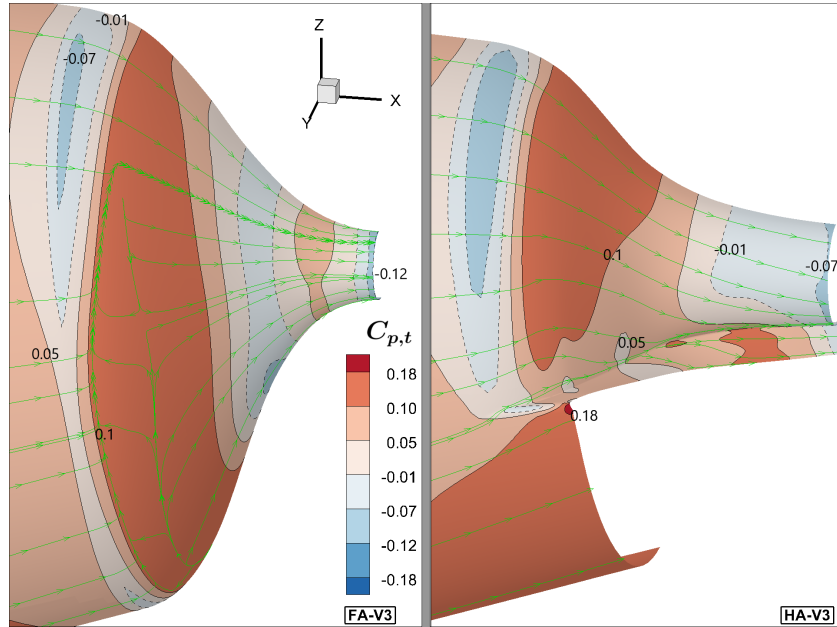


Figure 5.8: Pressure coefficient contours on the inner duct surface.

On the outer duct surface both designs display higher absolute values as this part concerns the faster moving flow. The FA design exhibits more negative C_p values due to the higher curvature of the duct, and like previously shows a more symmetric contour profile.

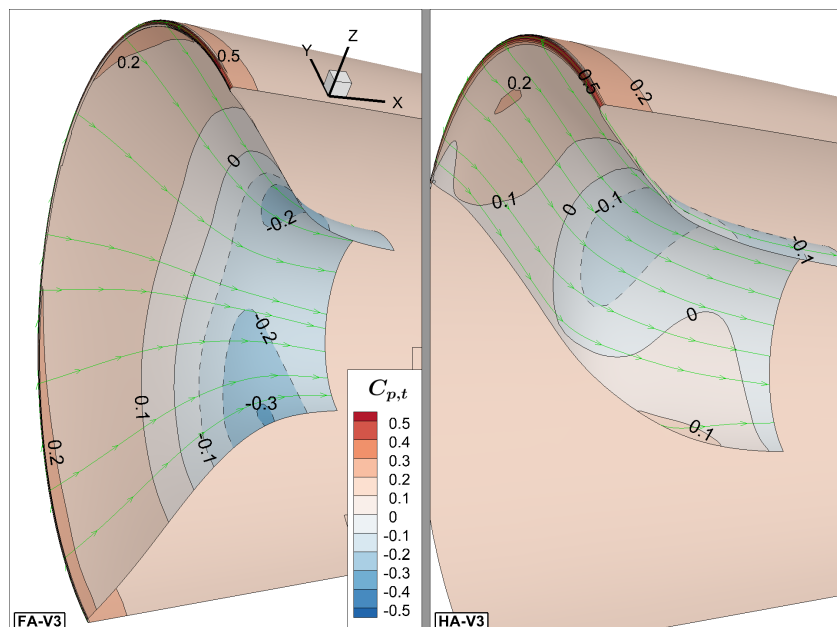


Figure 5.9: Pressure coefficient contours on the outer duct surface.

Effect on Compressor Face

Figure 5.10 shows the impact on the compressor. Note that the thickness of the compressor surface for FA-V3 is relatively large, which implies that the flow will face sections of the compressor blades that are relatively close to the hub. Therefore, since it is common in engine design to allow the air to enter at the outer blade section where rotational velocities are higher, the inner & outer radius of the compressor are increased. Nevertheless, the same area is maintained in order to conduct a consistent comparison. The distortion on the compressor is 9% higher for the HA design. The FA design displays a region of low total pressure at the midplane due to the large recirculation zone shown in Section 5.3.1, but it appears that the deficit is recovered by a great amount due to the fact that this design has a relatively high entrance area, allowing for a highly converging duct that evens out velocity deficits. Consequently, the distortion is much less than initially anticipated. The 60° section with lowest p_t for the HA on the other hand is made up of the bottom segment where the boundary layer is accumulated. Moreover, for both designs, at a roughly 45° angle, a velocity surplus is visible, which is caused by the higher velocity air that enters the intake, stemming from local accelerations of flow around the vertical tail surface as shown in Appendix E. For the HA version this effect is more pronounced as the ingested stream tube is thicker.

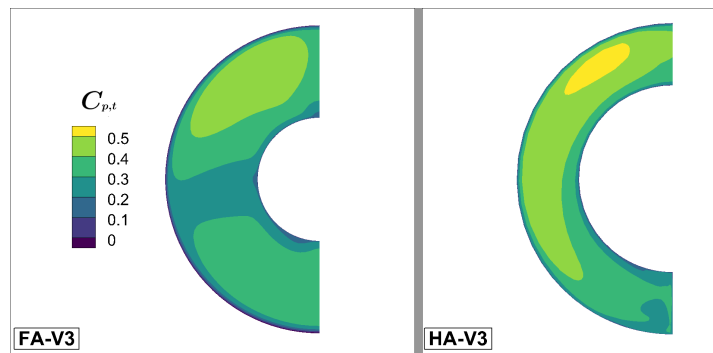


Figure 5.10: $C_{p,t}$ contours highlighting the effect of azimuthal extent on the compressor face.

Effect on Propeller

The effect on the propeller surface is demonstrated in Figure 5.11. The impact of adding an intake is evident, since the total pressure contours depict higher values, caused by the ingestion of (part of) the BL into the engine. The FA design shows a greater BL removal effect as expected, since the intake fully covers the circumference of the tailcone. The HA design on the other hand shows a greater effect for the top 60° section or so, but due to the nature of its design the other fraction remains unaltered. σ_p is increased from 81.3% to 82.6% percent in both designs⁵.

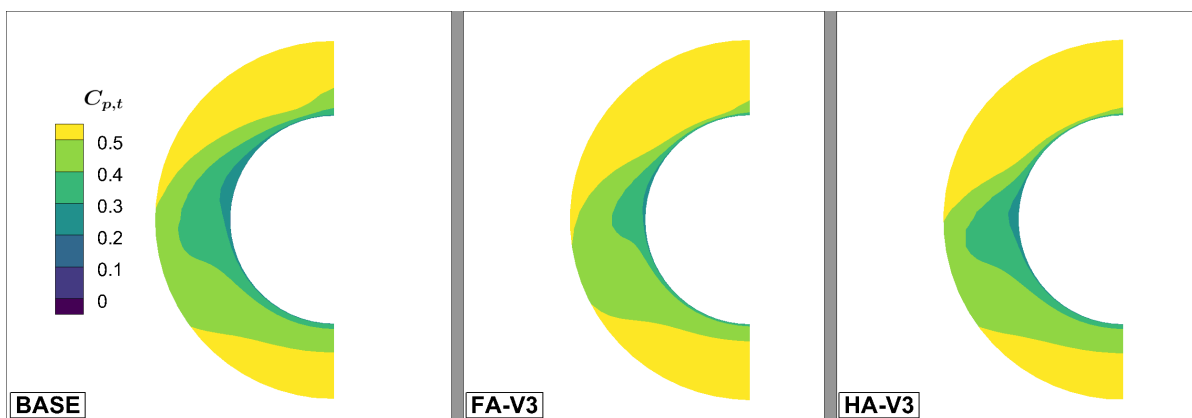


Figure 5.11: $C_{p,t}$ contours on the propeller surface.

⁵the difference lies in the second decimal

5.3.3. Duct Shape

The first HA design, HA-V1, shows a sharp decline in performance compared to FA-V3 as depicted in Figure 5.1. Figure 5.12 and Figure 5.13 show the Mach number distributions of the various designs. The figure on the left shows that the flow has a very high Mach number for a great portion of the duct. The strong bends result in high pressure gradients which excessively accelerate the flow. Another cause for this is that due to the large separated region, the effective area is reduced. With a smaller effective area the flow in the rest of the duct must have a higher velocity magnitude to comply with the mass flow rate requirement of the compressor. The separated zone at the sidewall is unable to recover due to the adverse pressure gradient that it faces along the duct, particularly as the flow curves in multiple directions in this portion of the duct. The area distribution in Figure 5.4 also clarifies this, as it initially show a sharp dip in area, which causes the flow to accelerate by a vast amount. After the minimum point, a high amount of diffusion takes place. The resulting adverse pressure gradient causes to flow to separate where it is most susceptible, namely at the sidewall. A relatively high drag coefficient that is visible in Figure 5.2 is attributed to the high velocity magnitude and separation.

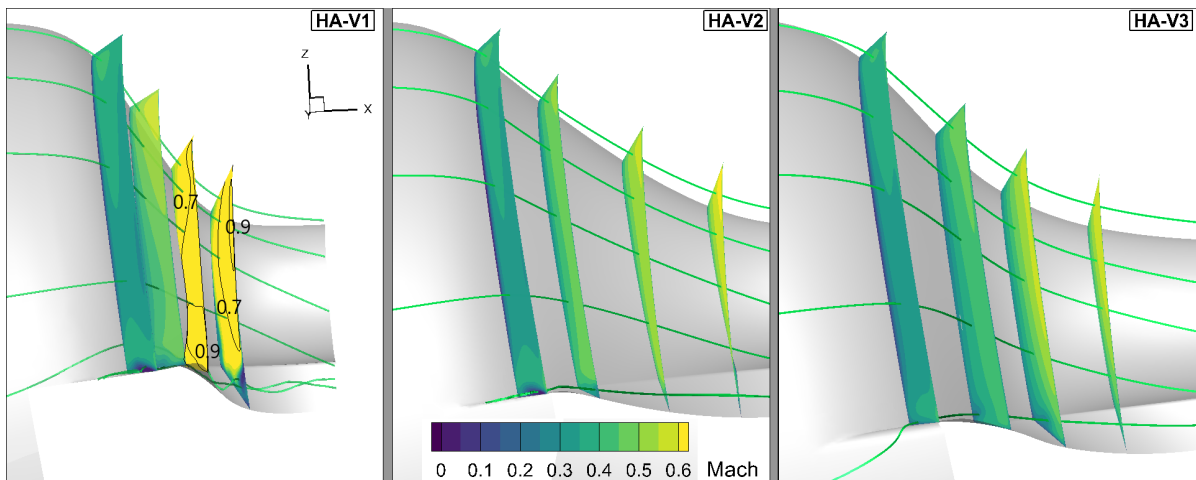


Figure 5.12: Mach number contours showing the effect of duct shape. The legend is shared between all figures.

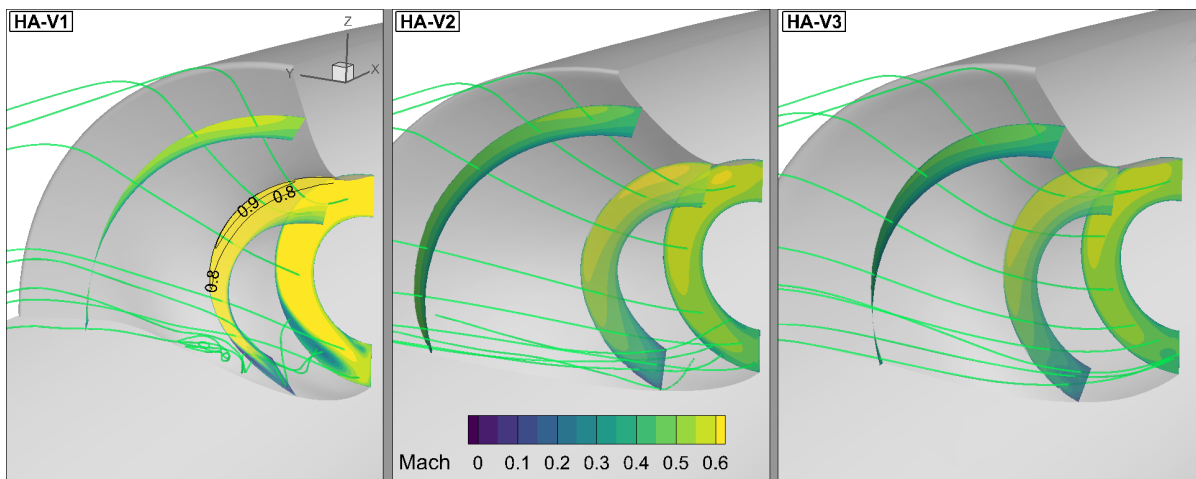


Figure 5.13: Mach number contours at an alternative perspective.

Due to the deteriorated performance of the HA-V1 from the angle of all evaluation metrics, the intake length was increased⁶ as the foremost improvement with an increase of $L = 0.9 Y$ to $L = 1.2 Y$, where Y is the vertical distance from compressor center point to the intake sidewall (as illustrated in Appendix A). This would reduce curvature magnitudes and help the flow to stay attached for longer. Figure 5.12 and Figure 5.13 affirm this hypothesis: HA-V2 outperforms HA-V1 by a large margin. The strong

⁶That is, the firewall was pushed back along the same axis by 200 mm, as the APPU hydrogen storage tank could potentially shrink in size and allow more room for the intake.

rotational flow is reduced significantly for HA-V2 and the maximum Mach number in the duct is kept at roughly 0.6 as compared to 1. The unfavorable area distribution of HA-V1 was also attempted to be made smoother, and although it would be possible to achieve this by maintaining the same length, a longer intake would facilitate in doing so. Figure 5.4 shows a more reasonable distribution, where the minimum and maximum value (in the interior) are closer to each other (vertically). This reduces the excessive acceleration and consequently the diffusion that takes place afterwards, allowing for more favorable conditions particularly close to the sidewall. Moreover, Figure 5.2 shows a significantly reduced pressure drag, but at the same time a slightly higher viscous drag term due to the increased amount of wetted area.

Next, since there is still a large velocity deficit close to the sidewall, the area distribution was further improved for the next iteration by enforcing a fully converging duct. Since $\frac{A_E}{A_{out}}$ is larger than one, it is more plausible to design a duct that completely avoids diffusion as this triggers separation. This change could potentially further improve the velocity deficit close to the sidewall. At the same time, the parameter h representing the alignment with respect to the engine⁷ was increased in order for the air to enter the compressor more axially aligned, which allows for more beneficial conditions at the compressor blades. Figure 5.12 and Figure 5.13 however depict that HA-V2 and HA-V3 show relatively low differences with respect to each other. Although HA-V3 shows a more homogeneous velocity profile particularly at the sidewall of the entrance, this is explained by a rounded corner, which will be discussed in the next section. The velocity deficit at the sidewall increases along the length of the duct nevertheless. Inspecting Figure 5.4, the area distribution of HA-V3 is less favorable for the upstream part of the duct. HA-V2 shows better flow quality due to its more converging nature at this segment of the duct, evening out non-uniformities. HA-V3 on the other hand has a stronger curvature in the first half of the duct, which is a side-effect of increasing h . Although it helps to align the flow axially, hence allowing more favorable conditions for the compressor, the downside is that the upstream part of the duct is negatively affected by sharper bends. Inspecting Figure 5.1, the two designs have an equivalent σ_d . The DC60 on the other hand is worse for HA-V3. Based on the observations, the fully converging area distribution of HA-V3 did not realize a notable improvement, but it could be said that the converging effect was negated by the stronger curve in the upstream part of the duct, caused by implementing another design chance simultaneously. Hence, the ideal solution would be to combine both the smooth duct shape of HA-V2 with the fully converging area distribution of HA-V3.

Similar results are obtained for SLS and are shown in Section E.2.

Effect on Compressor

Figure 5.14 shows total pressure coefficient contours at the compressor face. HA-V2 and HA-V3 show a significantly lower circumferential distortion profile than HA-V1. At high azimuthal angles, HA-V3 shows a thinner boundary layer due to the fact that the amount of diffusion is minimized throughout the entire duct by way of the duct area distribution. However, close to the sidewall a round shaped velocity deficit is formed.

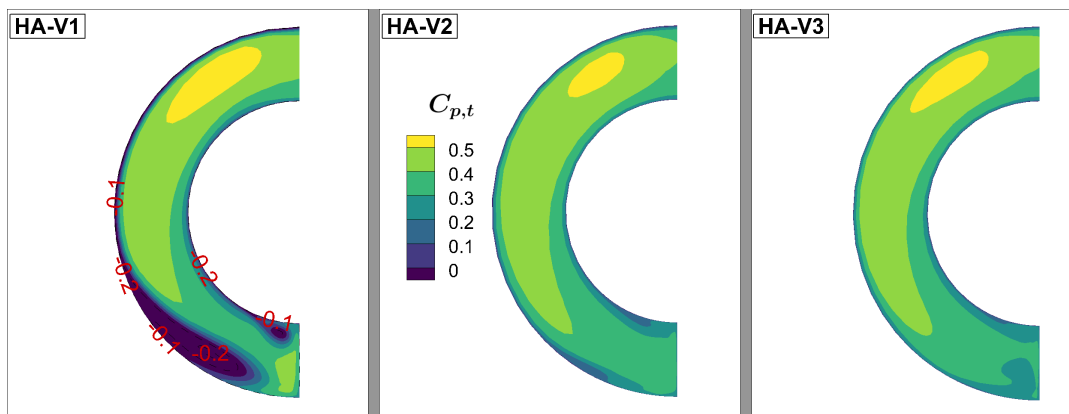


Figure 5.14: Total pressure contours at the compressor face.

⁷refer to Section A.3 for an illustration

Figure 5.15 shows the orientation of the flow at the compressor plane. The amount of planar flow, V_{planar} , that incorporates the radial and transverse velocity components, is defined as:

$$V_{planar} = \frac{V_y^2 + V_z^2}{|V|}$$

The improvement of HA-V2 relative to HA-V1 is clearly evident. HA-V3 further displays a diminished radial flow component, which is achieved by the increase in parameter h .

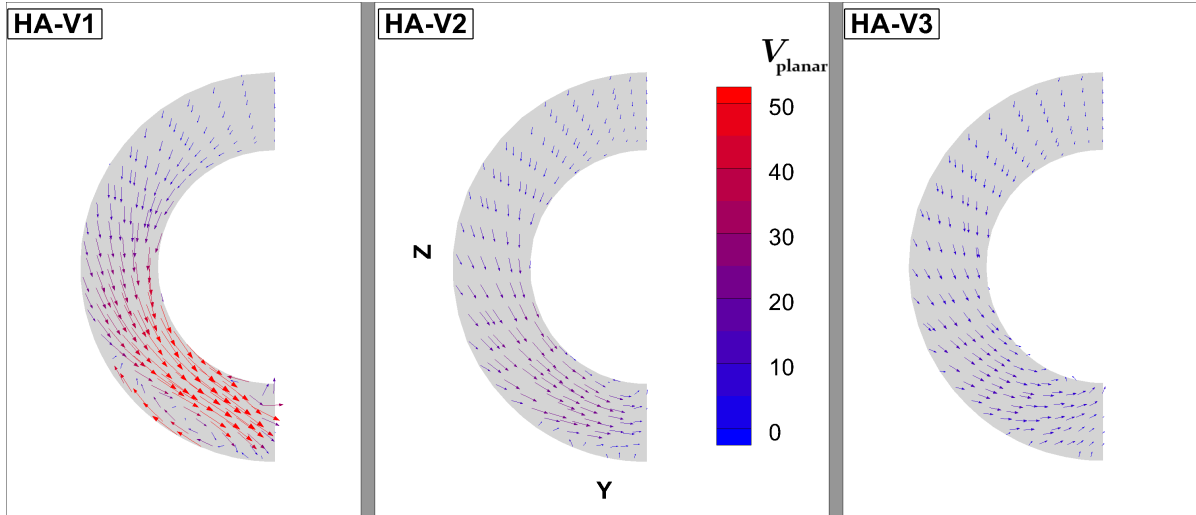


Figure 5.15: The direction of the velocity vectors is as follows: $x = V_y$ and $y = V_z$.

5.3.4. Corner Radius

For the HA designs, a vortex at the corner of the sidewall was detected, see Appendix E. The sharp corner causes a sudden & large difference in pressure on either side of the corner, causing the flow to separate and form a vortex that is, given the path of the surrounding flow, directed inside the duct. Therefore, to eliminate this vortex, it was decided to smoothen the edge of the corner for HA-V3 with a radius of 25 mm. With that, the pressure gradient would be reduced and the flow should be able to stay attached for longer. Figure 5.16 shows the effect of corner radius at the sidewall of the HA inlet. As expected, the wall shear vectors show that the air follows the shape of the intake better for a rounded corner. Where previously the wall shear vectors and streamlines made manifest a separation spot at the corner, the streamlines now show a much lower tendency to accumulate at the corner, but rather flow into the duct in a more undisturbed manner. Finally, although there seems to be a region with a negative wall shear stress in x-direction, which usually suggests a recirculation zone, upon inspection, the surface streamlines do not show a chaotic change in direction. Rather, a smooth and continuous flow is visible towards the interior of the intake. The volume streamlines close to the wall affirm this same behaviour as no vortex formation or recirculation is apparent. It was expected to detect a horseshoe vortex formation at the junction between the duct sidewall and intake lip, where the thick boundary layer does not

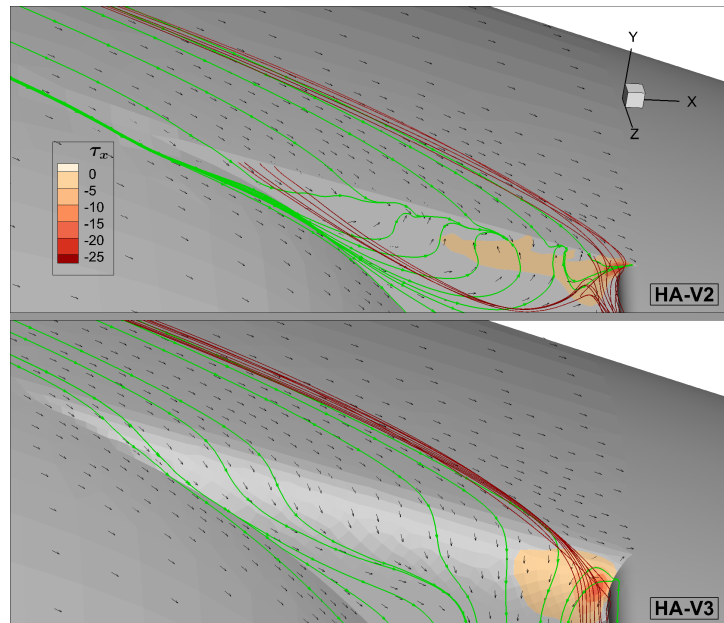


Figure 5.16: Effect of a blended corner on the flow field at cruise.

hold enough energy to reach a full stagnation, but instead forms a vortex that flows in two directions. Figure 5.16 however does not distinctly show this, likely because the inner boundary layer portion is sucked into the engine. The flow that faces the adverse pressure gradient upstream of the stagnation point therefore has higher energy, being able to reach a full stop without separating. Despite the visual improvement, merely a .13% higher total pressure arrives at the entrance for HA-V3. It is presumed that this is because the vortex of HA-V2 mixes in high velocity air with the BL, increasing the total pressure that is faced at the entrance, hence alleviating a part of the detrimental effects.

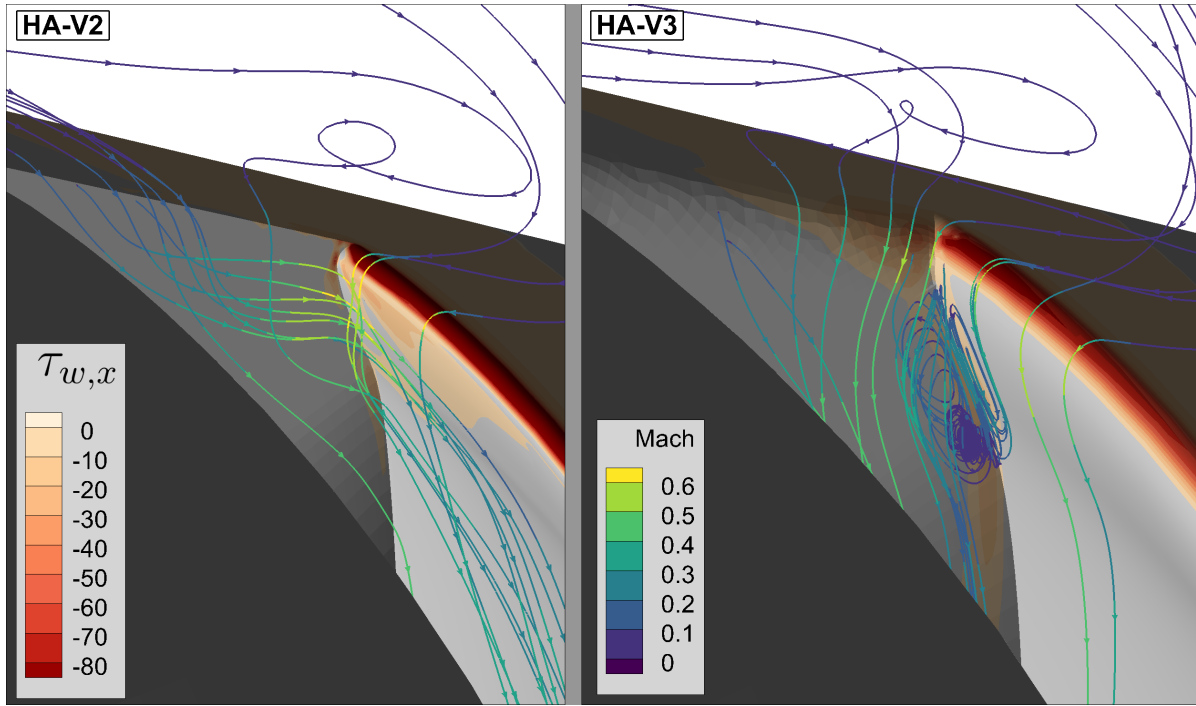


Figure 5.17: Effect of a blended corner on the flow field at SLS.

Figure 5.17 shows that the effect of a filleted corner is opposite at SLS: a large vortex is formed for the HA-V3 design. The difference between the two iterations lies in the nature of the generated vortex; for a sharp corner, the velocities induced by the vortex cause the streamlines that enter close to the sidewall to move towards the lip, and also roll away from the sidewall surface. In the case of a rounded corner, the air is able to enter from higher side-angles but due to this, interference effects at the junction between sidewall and outer duct surface trigger the flow to separate earlier, creating a vortex in this region. This vortex pulls the flow closer to the sidewall, which explains why the *DC60* of HA-V3 depicts a remarkable reduction of 65% compared to HA-V2. Moreover, the outer duct surface also appears concave, which further causes the flow to separate at the sidewall-duct edge.

5.3.5. Lip Shape

Finally, the effect of lip shape on the flow field is discussed. Note that at cruise, in all three cases no separation took place downstream of the lip along the entire azimuthal extent. Therefore, it is much more interesting to inspect the designs at SLS instead. The results are presented in Figure 5.18. The initial lip, on the left, shows a reasonably satisfactory performance. For the second lip design, it is therefore decided to reduce the lip radius, in order to investigate its feasibility and explore viable limits of lip radii. As it was expected to perceive a larger separation zone, a smoother & more continuous transition or blend with the duct surface was maintained to counteract this. Figure 5.18 shows that the adapted lip negatively affects the intake performance. Due to the high mass-flow requirement of the engine at SLS flight condition, the MFR is large. Hence, the stagnation line is located at the outside of the lip. A sharp lip in this case results in extensive accelerations induced by the strong pressure gradient, which causes the flow to separate downstream of the lip where the recovery takes place. It seems that a smoother transition with the duct surface did not sufficiently address this issue. Consequently, the original lip radius was reverted for the last lip design, whilst maintaining a higher

amount of continuity with respect to the outer duct surface. The curvatures of all three lips are shown in Appendix D. Figure 5.18 shows that the improvements were successful: the separated region is completely eliminated.

However, it must be noted that the ramp angle between the comparisons is not constant, which suggests that the turning angle is not the same for all designs. For instance, V2 shows a more horizontally aligned entrance than V1, which is a side effect of a longer intake.

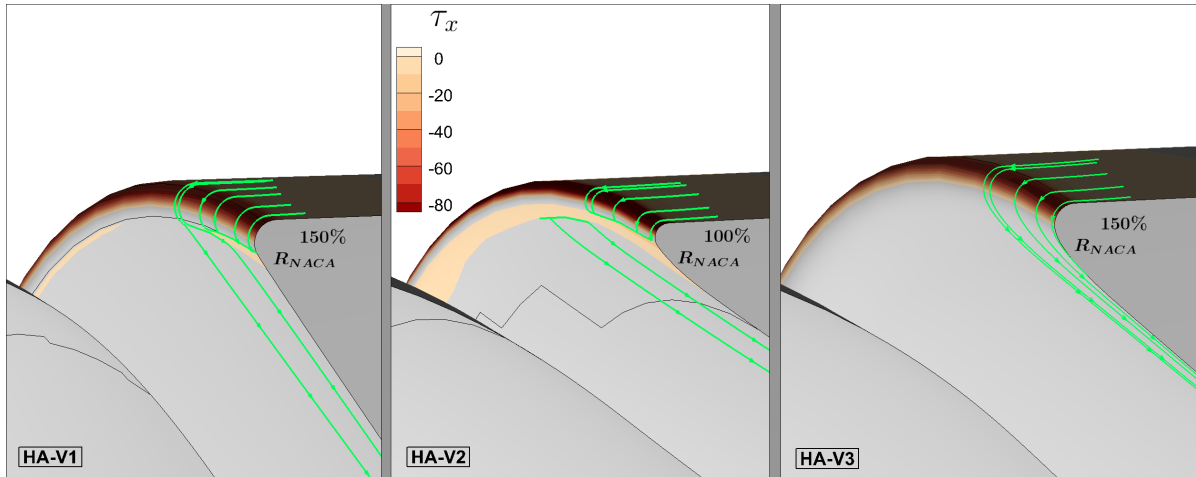


Figure 5.18: Contours of negative wall shear stress showing the effect of lip shape at SLS.

5.4. Geometry Definition

It was realized during the geometry design of HA-V1 and HA-V2 that the utilization of b-spline curves gives the user flexibility in forming the shape, but at the same time lacks to provide proper geometric constraints, since splines can be shaped at a high degree of freedom. Additionally, due to this adjustments for next iterations took a long time. Therefore, for HA-V3, more use had been made of circle-shaped elements, where the cross-sections but also the ramp curve were constructed using circular arcs. This helps the user to give a more consistent and robust geometry in cases where the geometry model consists of a complex 3D shape with a vast amount of design freedom. In this manner, the duct (cross-sectional) thickness can be maintained constant in tangential direction. This in turn can limit the amount of cross-flow that occurs, since a pressure gradient in azimuthal direction in that case is no longer present. Accordingly, the reduced planar flow component in Figure 5.15 may also be (partially) the result of a more consistent geometry definition.

Consequently, it should also be mentioned that part of the deteriorated performance of HA-V1 is caused by the geometry definition that is inconsistent in azimuthal direction, where the cross-section would become narrower. For HA-V1, precedence was given to defining the geometry longitudinally, but cross-sections were not given enough attention. Hence, regardless of whether splines or circular arcs are used, particularly when turning angles are great, cross-sections must be given adequate consideration.

6

Conclusions & Recommendations

In this thesis, the goal was to design a submerged inlet for the engine core of the APPU and thereby evaluate key inlet shape parameters that affect the flow field inside as well as surrounding the intake. Several inlets were designed where the entrance thickness, corner radius, duct shape, lip shape and entrance azimuthal range were varied. The focus was to evaluate the designs with respect to each other based on the distortion coefficient, drag coefficient, total pressure recoveries and lastly inspecting separation zones. A 3D CFD simulation has been adopted as the methodology of this thesis to achieve the goal. A grid convergence study showed that the mesh is too coarse at certain regions which affects the validity of the results, but it has been argued that a comparative analysis is nevertheless useful to conduct, where certain flow phenomena are identified and eliminated.

The results show that duct losses of smaller than 1% are achievable when employing a flush intake with converging duct shape that is integrated on the rear end of the fuselage. Losses lower than 20 % up to the duct entrance are unavoidable, attributed to the low energy content of the boundary layer.

For the full-annulus design, it has been shown that the non-uniform boundary layer that approaches the tailcone causes a large separation zone at the midplane. A reduced inlet thickness shows a great improvement, but even with a δ/D equal to 19.3 the separation zone is clearly visible. The results indicate that the entrance thickness should be further reduced if one wishes to eliminate this phenomenon. Results show a certain trade-off in designing this parameter: reducing the inlet thickness greatly reduces detrimental flow behavior, but a higher entrance thickness increases the ingested total pressure and allows for a more converging duct that evens out the flow. It can be concluded that the optimum area ratio $\frac{A_E}{A_{out}}$ at which clean airflow is desired lies below 2.9, where the resulting boundary layer thickness is $\frac{\delta}{D}$ is higher than 19.3. In case the total pressure recovery is a more decisive factor and some distortion is tolerable, the entrance thickness should be increased conversely.

Switching to a 180 ° intake that spans over the top half of the tailcone eliminated this separation zone with a δ/D of approximately 14. On the other hand, due to considerably stronger bends that induce a high pressure gradient, the distortion and drag were deteriorated. Where the FA design suffered from the large separation zone at the midplane, a great deal of recovery happened inside the duct due to the converging nature of the duct. Although a slightly higher total pressure recovery was achieved by the HA due to more energy being drawn from higher up in the boundary layer, the losses in the duct were roughly 6 % higher. Hence, the HA design performed distinctly worse, but a part of these losses that were observed is associated with the geometry definition: a very unfavorable area distribution caused extensive acceleration and diffusion to take place, eventually causing more losses. As such, improving the area distribution of the HA would very likely decrease the performance gap (of 6% in losses) with respect to a FA design with the same length by some margin, but fundamentally the duct of the FA would still have superior performance: the stronger curvatures of a HA design would be present nevertheless, regardless of the axial area distribution. Therefore, since no conclusion can be drawn on how much of these losses are due to the geometry definition, an updated HA with an improved duct shape must be designed in order to provide a more meaningful comparison with a FA design that is

similar in length.

However, increasing the intake length of the HA from $L/Y = 0.9$ (with 35 %) to $L/Y = 1.2$ greatly diminished the detrimental effects, where a significant separation zone inside the duct was almost completely eliminated. With this improvement, the total pressure recovery σ_t and distortion coefficient $DC60$ even surpassed the FA design. Furthermore, a duct that is fully converging should theoretically aerodynamically be superior, but due to other changes that were applied simultaneously its impact could not be isolated: it is believed that the favorable effects of a fully converging duct were counteracted by the detrimental effects of aligning a larger portion of (the the rear end of) the duct more with the engine, which caused stronger bends upstream and hence eliminated the anticipated favorable effects. In general, the greatest effect of duct shape is increasing its length. Although a slightly higher viscous drag is realized in that case, the favorable effects outweigh this disadvantage as far as the results of the thesis affirm. Therefore, the intake length should be increased if circumstances permit. Nonetheless, it should be noted that increasing h/L from 13 to 21 % resulted in a reduction of the in-plane velocity component on the compressor face, where radial and transverse flow were diminished. This suggests that the compressor faces more favorable conditions. However, a quantitative measure of this benefit (translated onto the blades) is not provided. Overall, it can be concluded that a HA is more favorable than a FA design, but exclusively due to the fact that higher total pressure arrives at the compress face.

With regards to the HA design, a filleted corner of the sidewall with a radius of $C/D = 0.36$ shows a clear favorable impact as compared to a sharp corner with $C = 0\text{mm}$, where the entrance velocity profile is more homogeneous and the weak vortex is eliminated. However, results show an underwhelming .1 % improvement in total pressure recovery at the entrance. A higher radius would likely amplify the gains. At SLS however, a large vortex was formed due to interference effects, but its effect on the total pressure recovery was not distinct. In contrast, the vortex pulled flow close to the sidewall and reduced the distortion coefficient at SLS with 60 %. Therefore, a round corner shows clear advantages over a sharp corner and should be implemented in all cases.

Lastly, compared to a lip with $R_{NACA} = 0.094 D$, a circular lip with a radius of $R = 0.188 D$, equivalent to 150% R_{NACA} , and a smoother transition to the inner duct wall shows the most favorable shape as in that case no separation takes place downstream of the lip at sea-level static conditions. It has also been found that the range of lip radii that were investigated all showed satisfactory performance at cruise at the given entrance thicknesses, but a low MFR was not apparent in this case. Therefore, in case e.g. low-thrust flight was considered the lip shape could also show considerable impact on the flow in this case.

Concerning the external aerodynamics, the addition of an inlet results in air entering the inner 25 % of the propeller with about 1.3% higher total pressure recovery. In case an open rotor configuration is utilized, the propeller thus faces higher quality flow. Overall, the addition of an intake can increase the drag coefficient by roughly 4 counts with respect to the base aircraft.

Moreover, it was discovered that the cross-sectional area distribution plays an important role in designing the intake. Using the area distribution to optimize the shape of the duct has proven successful and should be considered when optimizing the design. In that regard, the rolling-ball method is a useful tool to approximate the cross-sectional area distribution, since the area distribution graph aligned well with observations in the flow field of certain designs.

Lastly, using circular sections for the entrance ramp and cross-sectional sections at the duct facilitates the geometry creation process, providing more consistent and robustly shaped designs and allowing the user to create geometries more efficiently.

Future Work

Below, some relevant and important recommendations are listed:

- Refine the mesh at the regions where the too coarse mesh caused inaccuracies. Doing so will yield more realistic results.
- For the same reason, determine the correct flux type (Roe-FDS or AUSM) and discretization scheme (least-square or Green Gauss) settings in ANSYS Fluent.

-
- Model the main wing. This airframe component is expected to significantly impact the performance of the intakes by way of its down wash.
 - Test the designs at cross-wind conditions. Especially the rounded corner in that case is presumed to show a major advantage over the other designs. Another useful condition to consider is low-thrust cruise, where spillage over the intake will be much more pronounced. The reason these flight conditions are excluded in this thesis is due to time constraints, since these are less pivotal as they cover only a fraction of flight.
 - Vary the intake height, i.e. offset the lip by some amount in perpendicular direction away from the fuselage surface - practically designing a historical scoop-type intake - and evaluate its performance with respect to the submerged inlet type, to assess and determine the magnitude of the increase in drag and reduction in losses. This also gives more data into a comparative analysis of a scoop and submerged intake type in light of BLI, which is currently very limitedly explored in literature.
 - Further decrease the azimuthal extent of the intake to maximize the amount of energy ingested into the engine. This would at the same time result in larger duct losses. Nevertheless, it is relevant to demonstrate in that case which of the two phenomena dominates and where the optimum range lies.
 - Further increase the intake length. The results of this thesis affirm that the downsides to an increased length are negligible and the gains are overwhelming. It is useful to investigate how advantageous a further increase in intake length will be.
 - The area distribution could be further improved by shaping the duct such that the area stays moderately low for a larger section, i.e. where the flow has lower Mach number throughout a larger portion of the duct before accelerating towards the compressor face. Doing so promises a reduction in losses.

References

- [1] Airbus. Global market forecast | 2022-2041, July 2022. URL <https://www.airbus.com/en/products-services/commercial-aircraft/market/global-market-forecast>.
- [2] Industry High Level Group (IHLG). Aviation Benefits Report. Technical report, ICAO, 2019. URL <https://www.icao.int/sustainability/Documents/AVIATION-BENEFITS-2019-web.pdf>.
- [3] D. K. Hall, A. C. Huang, Al. Uranga, E. M. Greitzer, M. Drela, and S. Sato. Boundary layer ingestion propulsion benefit for transport aircraft. *Journal of Propulsion and Power*, 33(5):1118–1129, 2017. doi: 10.2514/1.B36321. URL <https://doi.org/10.2514/1.B36321>.
- [4] H. Steiner, A. Seitz, K. Plötner, A. Isikveren, and M. Hornung. Multi-disciplinary design and feasibility study of distributed propulsion systems. In *28th Congress of the International Council of the Aeronautical Sciences 2012, ICAS 2012*, volume 1, September 2012. URL https://www.icas.org/ICAS_ARCHIVE/ICAS2012/PAPERS/803.PDF.
- [5] M. Drela. Development of the d8 transport configuration. In *29th AIAA Applied Aerodynamics Conference*, 2011. URL https://web.mit.edu/drela/Public/papers/Hawaii_11/Drela_AIAA2011_3970.pdf.
- [6] M. Drela. Power balance in aerodynamic flows. *AIAA Journal*, 47(7):1761–1771, 2009. doi: 10.2514/1.42409. URL <https://doi.org/10.2514/1.42409>.
- [7] A. L. Habermann, J. Bijewitz, A. Seitz, and M. Hornung. Performance bookkeeping for aircraft configurations with fuselage wake-filling propulsion integration. *CEAS Aeronautical Journal*, 11(2): 529–551, 2020. ISSN 1869-5582. doi: 10.1007/s13272-019-00434-w.
- [8] Joachim Kurzke and Ian Halliwell. *Inlet Flow Distortion*, pages 249–267. Springer International Publishing, Cham, 2018. ISBN 978-3-319-75979-1. doi: 10.1007/978-3-319-75979-1_6. URL https://doi.org/10.1007/978-3-319-75979-1_6.
- [9] E. Taskinoglu and D. Knight. Numerical analysis of submerged inlets. In *20th AIAA Applied Aerodynamics Conference*. AIAA, June 2012. doi: 10.2514/6.2002-3147. URL <https://arc.aiaa.org/doi/abs/10.2514/6.2002-3147>.
- [10] S. Farokhi. *Aircraft Propulsion*. Wiley, 2th edition, May 2014. ISBN 9781118806777. pp. 338-348.
- [11] A. Sóbester. Tradeoffs in jet inlet design: A historical perspective. *Journal of Aircraft*, 44(3):705–717, 2007. doi: 10.2514/1.26830. URL <https://doi.org/10.2514/1.26830>.
- [12] P. Alves, M. Silvestre, and P. Gamboa. Propulsive efficiency comparison for various gas turbine engine configurations, June 2020. URL https://en.wikipedia.org/wiki/Propfan#/media/File:Propulsive_efficiency_for_different_engine_types_and_Mach_numbers.png.
- [13] S. Kazula and K. Höschler. Review of variable leading-edge patents for aircraft wings and engine inlets and their relevance for variable pitot inlets in future supersonic transport. *CEAS Aeronautical Journal*, 12(3):685–700, 2021. ISSN 1869-5582. doi: <https://doi.org/10.1007/s13272-021-00520-y>.
- [14] A. Heidebrecht. WP1 | Project review Oct 2022, October 2022.
- [15] A. Sharma. Design of Inlet for Boundary Layer Ingestion in a Blended Wing Body Aircraft, 2015. URL <http://resolver.tudelft.nl/uuid:2ae08e95-438a-4b6e-acdf-b74629855924>.
- [16] A.G. Rao, A. Sharma, and R. v. Dijk. A CFD Based Parametric Analysis of S-shaped Inlet for a Novel Blended Wing Body Aircraft. *International Conference on Advances in Thermal Systems, Materials and Design Engineering (ATSMDE2017)*, February 2018. doi: 10.2139/ssrn.3101299. URL <https://ssrn-com.tudelft.idm.oclc.org/abstract=3101299>.

- [17] J.S. Dennard. A transonic investigation of the mass-flow and pressure recovery characteristics of several types of auxiliary air inlets. Technical report, NACA, April 1957. URL https://digital.library.unt.edu/ark:/67531/metadc63083/m2/1/high_res_d/19930089560.pdf.
- [18] C.W. Frick. An Experimental Investigation of NACA Submerged-Duct Entrances - NASA Technical Reports Server (NTRS), October 1945. URL <https://ntrs.nasa.gov/citations/20050061115>.
- [19] T. Reynolds. Flow control application in a submerged inlet characterized by three-component ldv, 2010. URL <https://ui.adsabs.harvard.edu/abs/2010PhDT.....134R/abstract>.
- [20] L.R. Owens, B.G. Allan, and S.A. Gorton. Boundary-Layer-Ingesting Inlet Flow Control. Technical Report 23681, NASA, n.d. URL <https://ntrs.nasa.gov/api/citations/20060004990/downloads/20060004990.pdf>.
- [21] A. Sacks. Theoretical Investigation of Submerged Inlets at Low Speeds - NASA Technical Reports Server (NTRS), August 1951. URL <https://ntrs.nasa.gov/citations/19890067876>.
- [22] C.W. Frick, W.F. Davis, L. Randall, and E.A. Mossman. An Experimental Investigation of NACA Submerged-Duct Entrances. Technical report, NACA, May 1945. URL <https://ntrs.nasa.gov/citations/20090012113>.
- [23] Leticia Hime, Cesar CELIS, Luís Fernando Figueira da Silva, Sandro Ferreira, Antonio Batista de Jesus, Viviam Takase, and Harry Vinagre. A review of the characteristics of submerged air intakes. In *18th International Congress of Mechanical Engineering*, November 2005. URL https://www.researchgate.net/publication/280249375_A_Review_of_the_Characteristics_of_Submerged_Air_Intakes.
- [24] J.L. Frank and R.A. Taylor. Comparison of drag, pressure recovery and surface pressure of a scoop-type inlet and NACA submerged inlet at transonic speeds. Technical report, NACA, October 1954. URL https://digital.library.unt.edu/ark:/67531/metadc58998/m2/1/high_res_d/19930086824.pdf.
- [25] J.S. Dennard. The Total-Pressure Recovery and Drag Characteristics of Several Auxiliary Inlets at Transonic Speeds. Technical report, NACA, March 1959. URL <https://ntrs.nasa.gov/citations/19980231994>.
- [26] E. Mossman, L. Randall, NATIONAL AERONAUTICS, and SPACE ADMINISTRATION MOFFETT FIELD CA AMES RESEARCH CENTER. An Experimental Investigation of the Design Variables for NACA Submerged Duct Entrances, 1948. URL <https://apps.dtic.mil/sti/citations/ADA800887>.
- [27] Mehdi Miansari, Sajad Ghezelsofloo, and Davood Toghraie. Numerical investigation of geometrical design effect on the submerged inlet aerodynamics characteristics. *International Journal of Aeronautical and Space Sciences*, 21(1):25–38, 2020. ISSN 2093-274X. doi: 10.1007/s42405-019-00211-3. URL https://www.researchgate.net/publication/335725939_Numerical_Investigation_of_Geometrical_Design_Effect_on_the_Submerged_Inlet_Aerodynamics_Characteristics.
- [28] Wenzhong Xie, Cheng Zeng, Zhenyu Wang, and Shengmin Guo. Flow Control for a Submerged Inlet. *Journal of Fluids Engineering*, 144(12), 08 2022. ISSN 0098-2202. doi: 10.1115/1.4055073. URL <https://doi.org/10.1115/1.4055073>. 121202.
- [29] O. de Almeida, P.C. Souza, and E. Cunha. A numerical approach for implementing air intakes in a canard type aircraft for engine cooling purposes. *Journal of Aerospace Technology and Management*, 13, 2021. ISSN 2175-9146. doi: 10.1590/jatm.v13.1192. URL <https://www.scielo.br/j/jatm/a/TnXSNpGLSwKjw4dYR58WfKq/>.
- [30] S.F. Rolls. Flight evaluation and comparison of a NACA submerged inlet and a scoop inlet on the YF-93A., October 1951. URL <https://digital.library.unt.edu/ark:/67531/metadc59511/>.
- [31] Markus Rütten, Lars Krenkel, and Malte Freund. Parametric design, comparison and evaluation of air intake types for bleedless aircraft. In *39th AIAA Fluid Dynamics Conference*, June 2009. doi: 10.2514/6.2009-3902. URL <https://arc-aiaa-org.tudelft.idm.oclc.org/doi/10.2514/6.2009-3902>.

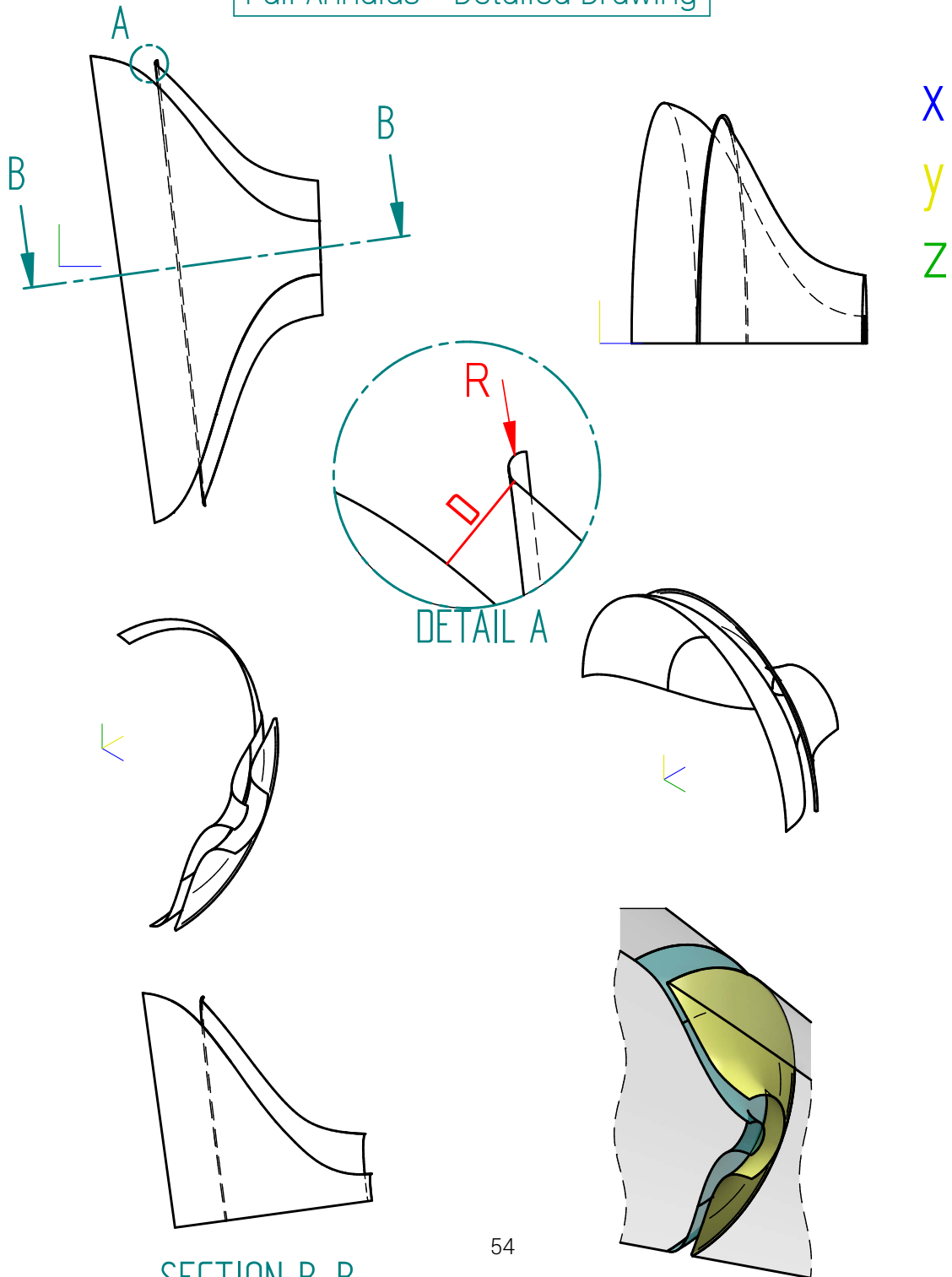
- [32] DisPURSAL. DisPURSAL, 2015. URL http://www.dispursal.eu/doc/DisPURSAL_Overview_aerodays2015_modWebsite.pdf.
- [33] Wenzhong Xie, Cheng Zeng, Zhenyu Wang, and Shengmin Guo. Flow Control for a Submerged Inlet. *Journal of Fluids Engineering*, 144(12), 08 2022. ISSN 0098-2202. doi: 10.1115/1.4055073. URL <https://doi.org/10.1115/1.4055073>. 121202.
- [34] N. J. Pignier, C. J. O'Reilly, and S. Boij. Aerodynamic and aeroacoustic analyses of a submerged air inlet in a low-mach-number flow. *Computers & Fluids*, 133:15–31, 2016. ISSN 0045-7930. doi: <https://doi.org/10.1016/j.compfluid.2016.04.010>. URL <https://www.sciencedirect.com/science/article/pii/S004579301630113X>.
- [35] H.K. Versteeg and W. Malalasekera. *An Introduction to Computational Fluid Dynamics*. Pearson, 2 edition, 2007.
- [36] InternacionalWeb. Advantages of CFD | FEA services and consultancy. CFD and FEA company, n.d. URL <http://www.pretechnologies.com/services/computational-fluid-dynamics/advantage>.
- [37] NASA. Navier-Stokes Equations, n.d. URL <https://www.grc.nasa.gov/www/k-12/airplane/nseqs.html>.
- [38] S. N. Pachpute. Basics of CFD Modeling for Beginners ., n.d. URL <https://cfdflowengineering.com/basics-of-cfd-modeling-for-beginners/>.
- [39] P. Dutta, S. Kumar Saha, N. Nandi, and N. Pal. Numerical study on flow separation in 90° pipe bend under high reynolds number by $k - \epsilon$ modelling. *Engineering Science and Technology, an International Journal*, 19(2):904–910, 2016. ISSN 2215-0986. doi: <https://doi.org/10.1016/j.jestch.2015.12.005>. URL <https://www.sciencedirect.com/science/article/pii/S2215098615301610>.
- [40] C Stijn. File:Geometric continuity.png - Wikipedia, 10 2022. URL https://en.wikipedia.org/wiki/File:Geometric_continuity.png.
- [41] Siemens Digital Industries Software. Solid Edge | Siemens | 3D Design, Simulation, Manufacturing, 2021. URL <https://solidedge.siemens.com/en/>. Computer Software.
- [42] A. Bayón. Wall functions | Introduction to CFD, n.d. URL <https://cfd.blogs.upv.es/turbulence/wall-functions/>.
- [43] F.M. White. *Fluid Mechanics*. McGraw-Hill, 5th edition, January 2002. ISBN 978-0071199117.
- [44] Cadence. Fidelity pointwise for cfd meshing, 2022.2. URL https://www.cadence.com/en_US/home/tools/system-analysis/computational-fluid-dynamics/pointwise.html. Computer Software.
- [45] ANSYS Inc. Ansys fluent fluid simulation software, 2022R2. URL <https://www.ansys.com/products/fluids/ansys-fluent>. Computer Software.
- [46] Ideal Simulations. Turbulence models in CFD, n.d. URL <https://www.idealsimulations.com/resources/turbulence-models-in-cfd/>.
- [47] F. Menter. Zonal two equation k-w turbulence models for aerodynamic flows. *23rd Fluid Dynamics, Plasmadynamics, and Lasers Conference*, August 2012. doi: 10.2514/6.1993-2906. URL <https://arc.aiaa.org/doi/abs/10.2514/6.1993-2906>.
- [48] Eiman B. Saheby, Xing Shen, Guoping Huang, and Anthony P. Hays. Flow structure of the ridge integrated submerged inlet. *Aerospace Science and Technology*, 119:107136, December 2021. ISSN 1270-9638. doi: <https://doi.org/10.1016/j.ast.2021.107136>. URL <https://www.sciencedirect.com/science/article/pii/S1270963821006465>.
- [49] W.Z. Xie, S.Z. Yang, C. Zeng, K. Liao, R.H. Ding, L. Zhang, and S. Guo. Effects of forebody boundary layer on the performance of a submerged inlet. *The Aeronautical Journal*, 125(1289):1260–1281, 2021. doi: 10.1017/aer.2021.8.

- [50] Tecplot Inc. Tecplot 360, 2022. URL <https://tecplot.com/products/tecplot-360/>. Computer Software.
- [51] L. Eça and M. Hoekstra. On the influence of the iterative error in the numerical uncertainty of ship viscous flow calculations. January 2006. URL https://www.researchgate.net/publication/268300044_On_the_Influence_of_the_Iterative_Error_in_the_Numerical_Uncertainty_of_Ship_Viscous_Flow_Calculations.
- [52] Pointwise, T. Carrigan, and sarahhope swaim. pointwise/GridRefine, n.d. URL <https://github.com/pointwise/GridRefine>.
- [53] I.B. Celik, U. Ghia, P.J. Roache, C.J. Freitas, H. Coleman, and P.E. Raad. Procedure for Estimation and Reporting of Uncertainty Due to Discretization in CFD Applications. *Journal of Fluids Engineering*, 130(7):078001, 07 2008. ISSN 0098-2202. doi: 10.1115/1.2960953. URL <https://doi.org/10.1115/1.2960953>.
- [54] I.B. Celik, U. Ghia, P.J. Roache, C.J. Freitas, H. Coleman, and P.E. Raad. Procedure for Estimation and Reporting of Uncertainty Due to Discretization in CFD Applications. *Journal of Fluids Engineering*, 130(7):078001, 07 2008. ISSN 0098-2202. doi: 10.1115/1.2960953. URL <https://doi.org/10.1115/1.2960953>.
- [55] J.W. Slater. Examining spatial (Grid) convergence, February 2021. URL <https://www.grc.nasa.gov/www/wind/valid/tutorial/spatconv.html>.
- [56] AGARD (Advisory Group for Aerospace Research & Development). Guide to in-flight thrust measurement of turbojets and fan engines. Technical report, 2000. URL <https://apps.dtic.mil/sti/tr/pdf/ADA065939.pdf>.

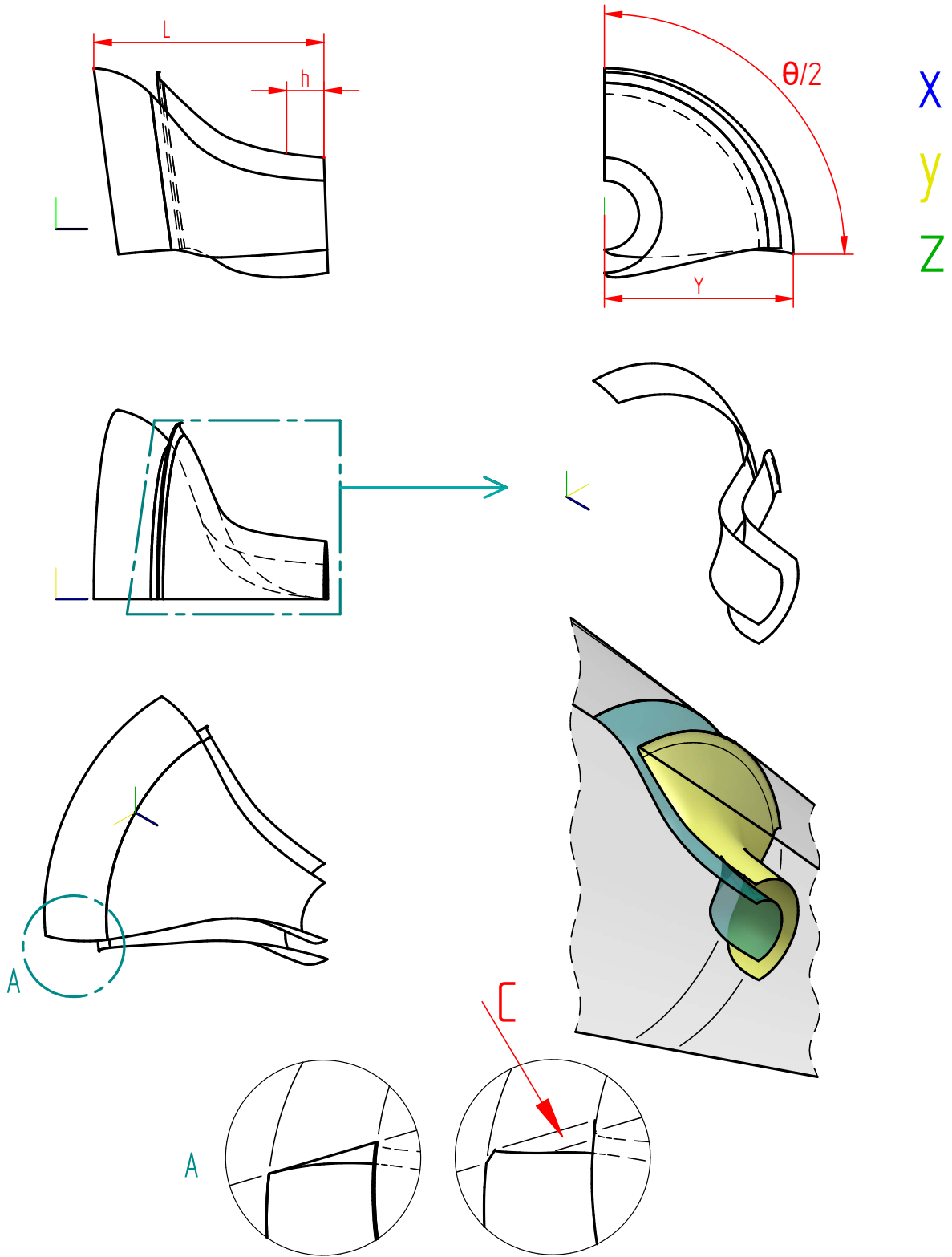
A Geometry

A.1. Geometry Close-up

Full Annulus - Detailed Drawing



Half Annulus - Detailed Drawing



CORNER TYPE

Figure A.1: Close-up view on geometries

A.2. Axial Development of Shape

Figure A.2 shows cross-sectional surfaces inside the duct. Note that because the intake is built at an angle with respect to the Y-axis (due to the orientation of the firewall), the lower side of the sections at the front appear thinner.

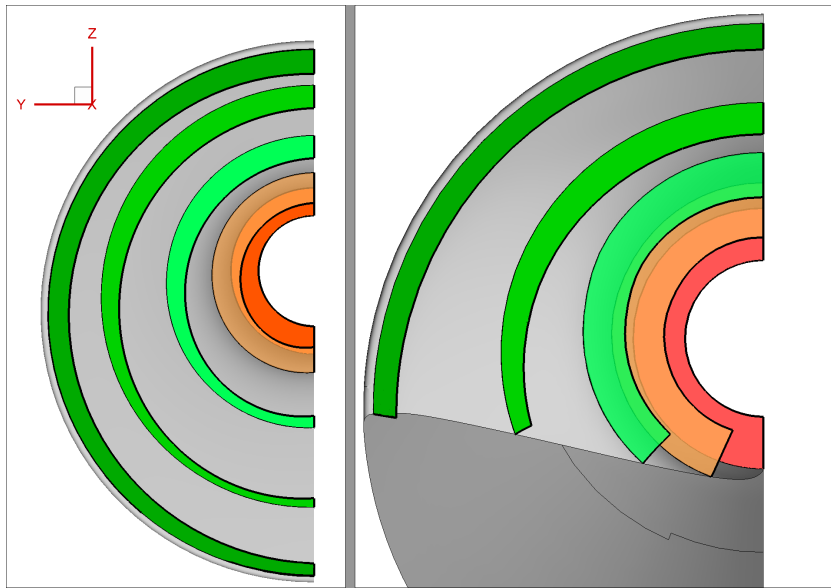


Figure A.2: Axial development of duct towards compressor surface. Left: FA, right: HA.

A.3. Measurement of Engine Alignment

The fraction h of the total length L is defined as: the extent of the most aft part of the duct that is aligned tangentially with respect to the engine surface. This is illustrated in Figure A.3. h is defined as the distance between the compressor and a certain point on the duct, where the duct makes a maximum angle of 5° angle with respect to the engine outer face.

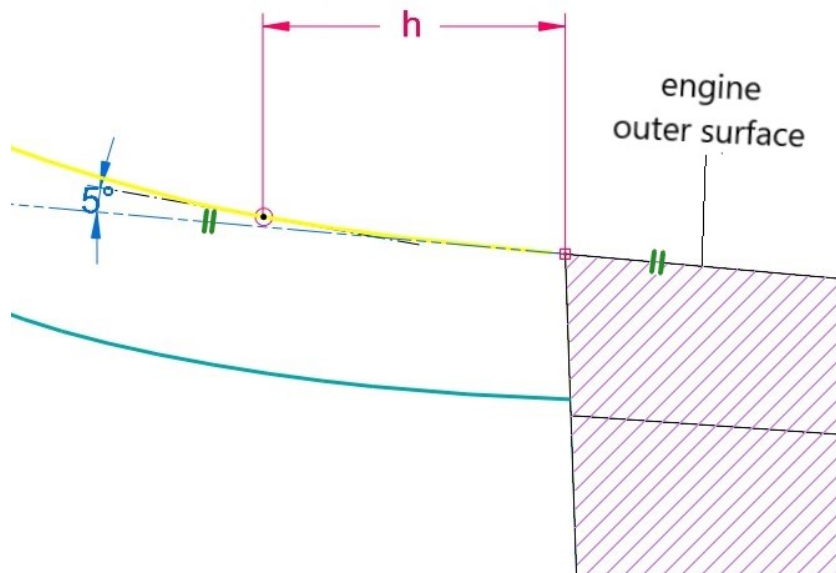


Figure A.3: Estimation of engine alignment h . The region filled in purple represents the engine. Although the engine is not modeled in this thesis, it has been used to determine the connectivity of the duct with the compressor.

B

Mesh

B.1. Overview of Mesh

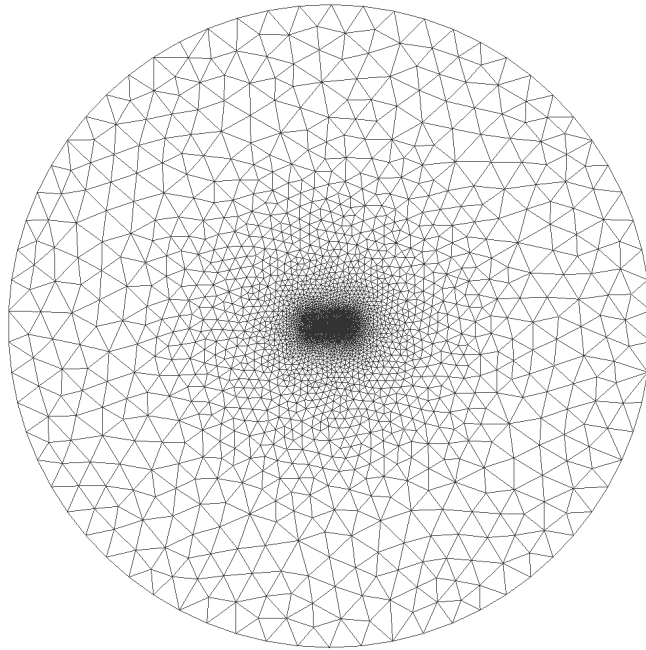


Figure B.1: Mesh of the entire domain

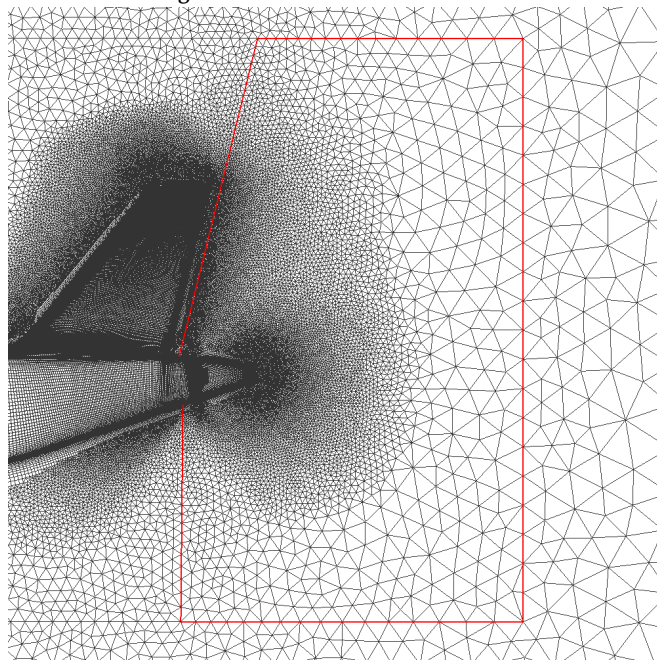
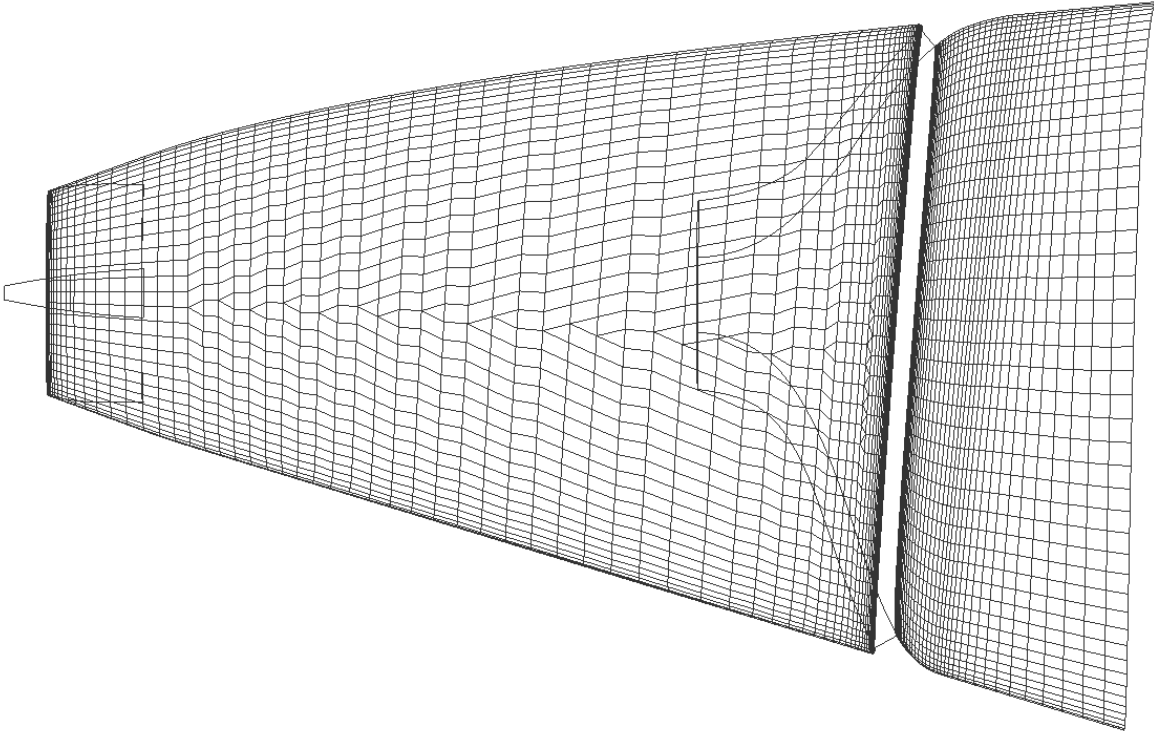
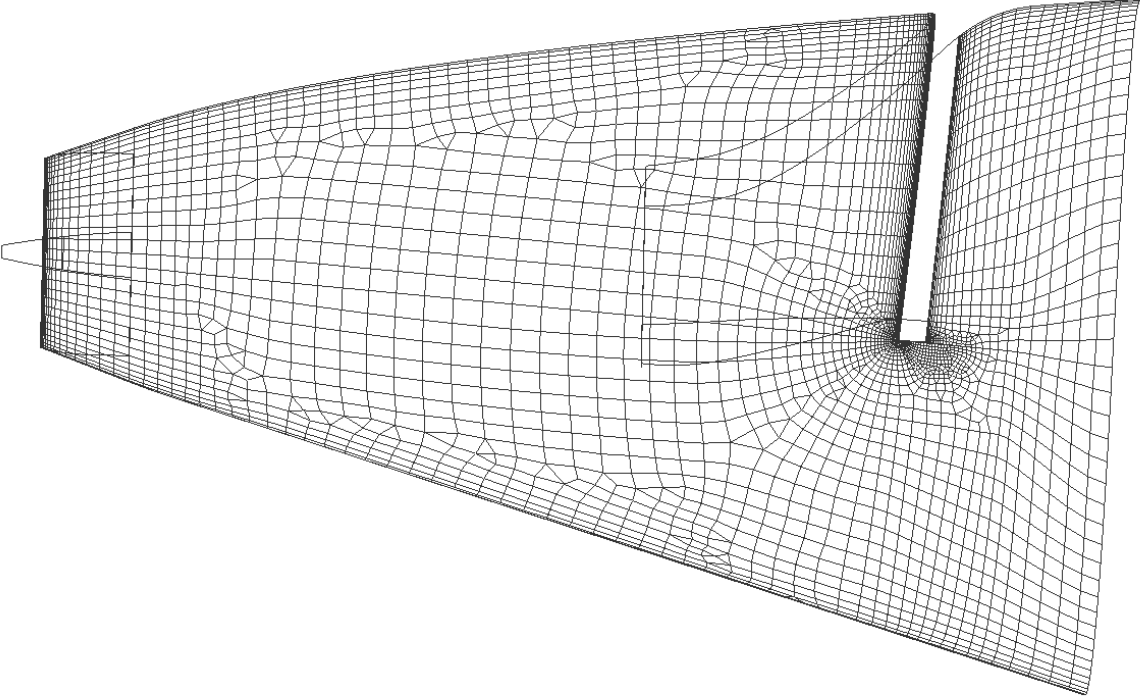


Figure B.2: Mesh of tailcone region. The nearfield borders are highlighted in red

B.2. Mesh Comparison



(a) Full-annulus



(b) Half-annulus

Figure B.3: Surface mesh comparison between FA and HA.

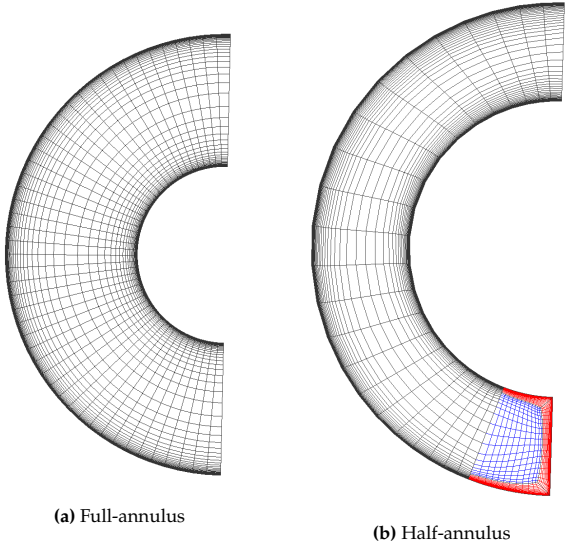
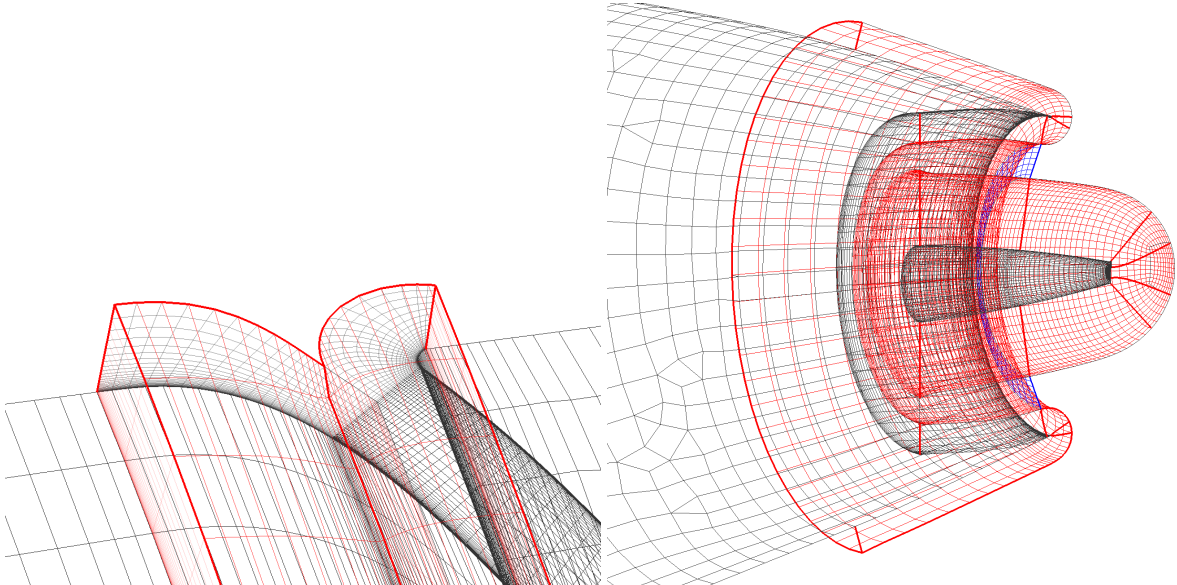


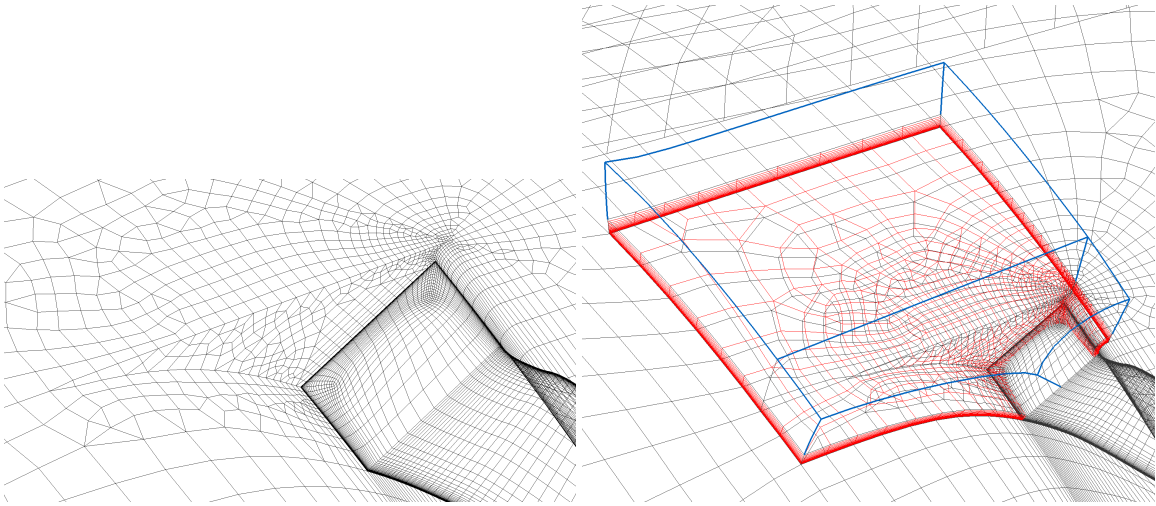
Figure B.4: Mesh comparison at compressor face

B.3. Boundary Layer Assembly



(a) BL at intake of full-annulus. (b) Mesh around tailcone trailing edge. The space at the interior of the nozzle (blue) is filled in using a structured block.

Figure B.5: BL mesh of FA & nozzle mesh topology



(a) BL of sidewall inside of the duct. Display of OH-mesh.

(b) BL at ramp corner. The mesh is extruded first for 40 cells (red). Afterwards, a regular unstructured block is initialized on top of that using the adjacent domains of the surrounding blocks as boundaries (blue).

Figure B.6: Construction of boundary layer mesh of half-annulus design.

C.1. Convergence

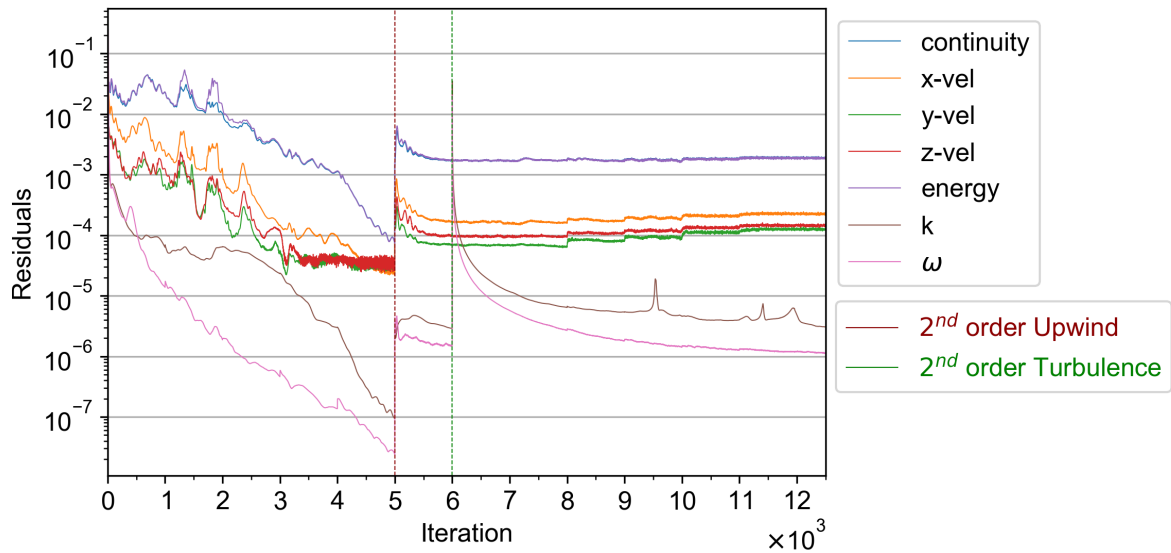


Figure C.1: Plot of the residuals until the simulation is concluded at 12,500 iterations.

The vertical lines in Figure C.1 indicate a transition from first to second order. The simulation was initiated in first order to facilitate convergence. The small jumps in residuals at certain points display an increase in Courant number which is increased to accelerate convergence.

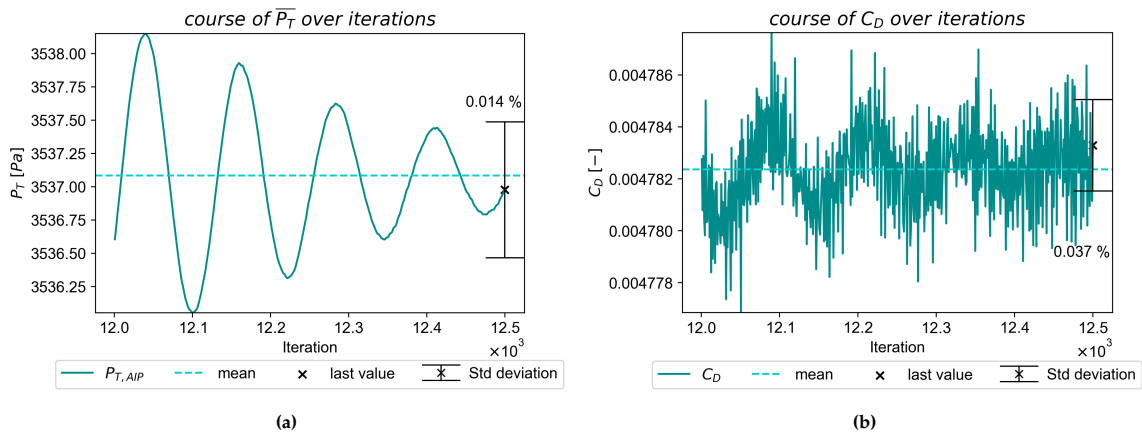


Figure C.2: Standard deviation of P_t (a) and C_D (b) at the compressor surface.

Figure C.2 show that the simulation is converged as the residuals fluctuate with a sufficiently low amplitude (std. deviation < 1%) around the mean value.

C.2. Extra Contours of Mesh Resolution Differences

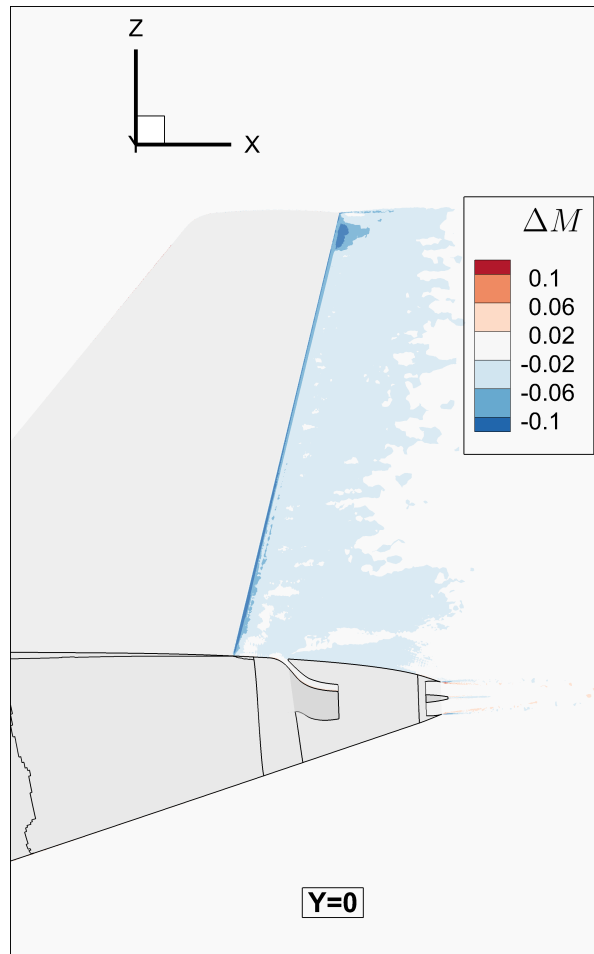


Figure C.3: Difference in Mach contour at the wake of the vertical tail plane.

C.3. Clarification of Error Estimation Method

The interpolation described in Chapter 4 may not be entirely accurate, as it was noted that the interpolation of the coarse on the fine mesh resulted in extremely large differences at certain spots, where in fact no difference was expected. E.g., Figure C.4 shows a notable difference at the furthestmost part of the tailcone, which is believed to be caused by inaccuracies in the interpolation, since a side-by-side comparison of the two meshes did not reveal any significant changes. Another example is demonstrated in Figure C.5. The imprecise interpolation occurs due to a slight difference in geometry; a finer mesh more closely represents a circle, whereas a coarse mesh has more distinct sharp angles between the cells.

Therefore, the error estimation method is limited by the inaccuracies of the interpolation. Even though an attempt was made to filter out this data, by removing data points beyond a certain minimum & maximum from the dataset, it would not ensure a precise solution.

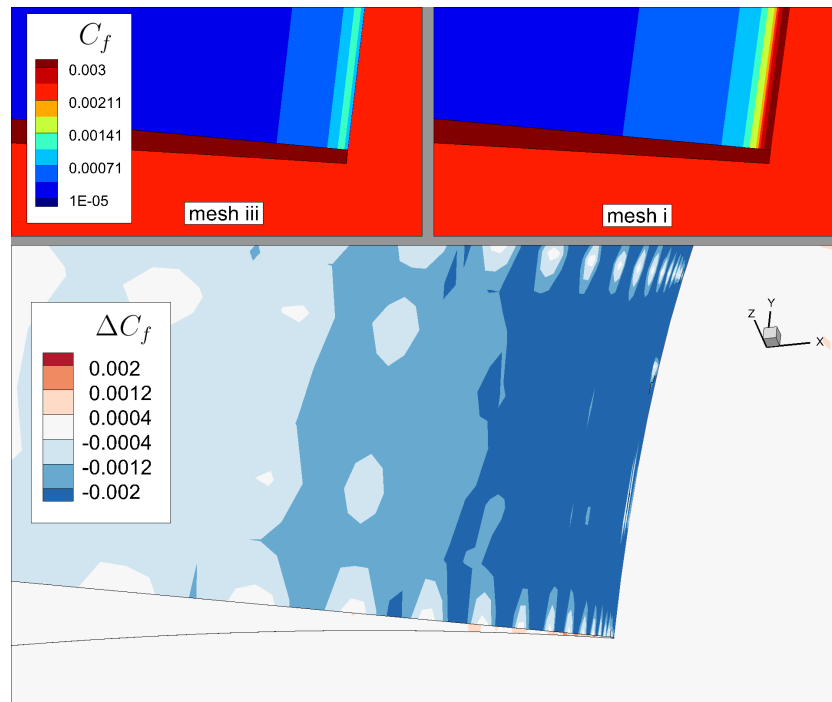


Figure C.4: Difference in skin friction coefficient at the nozzle region between fine and coarse mesh. The figure is a close-up of the box in Figure 4.7

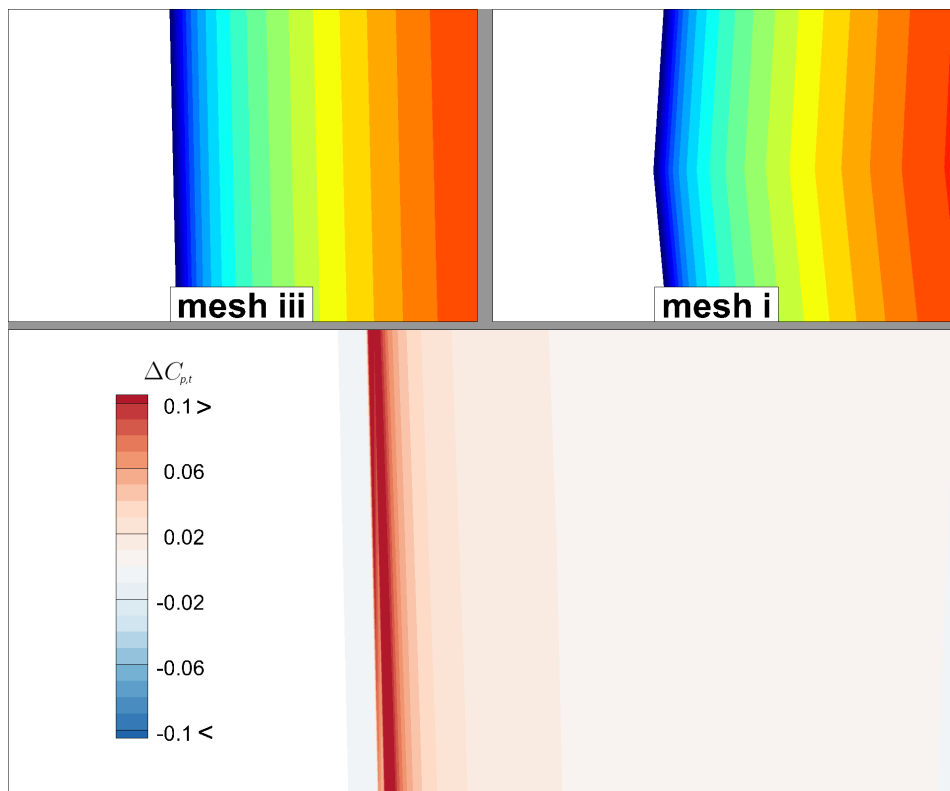


Figure C.5: Close-up view of outer edge of the compressor, see red box in Figure 4.6a.

C.4. GCI of Alternative Settings

Below, the GCI parameters are provided for the AUSM flux type and Green-Gauss cell-based differential scheme. Table C.1 shows that the GCI is now in the order of tens. So, it is concluded that in both cases the grid convergence study has been unsuccessful.

	C_D	σ_t
Theoretical order p	2	
Apparent order p	0.49	0.32
exact value (h=0)	41.47	0.761
approx. error [%]	3.13	0.3
exact error [%]	16.5	2.2
GCI_{fine} [%]	17.73	2.7
GCI_{coarse} [%]	14.08	3.07
ratio of GCIs	0.97	1.29

Table C.1: Grid Convergence Parameters.

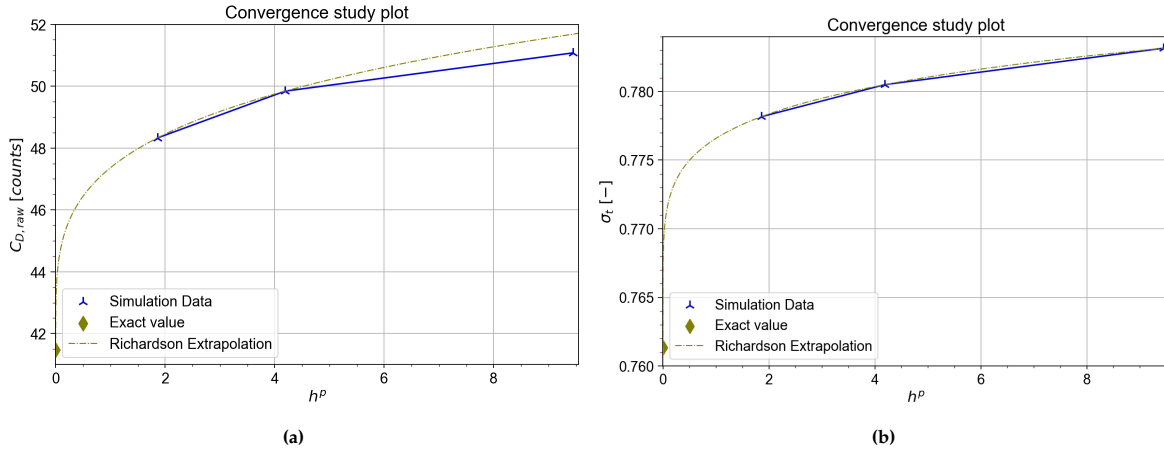


Figure C.6: Plots of mesh convergence with Richardson extrapolation. As before, the calculations are performed using the apparent order, but the plots employ the theoretical order on the x-axis.

Table C.2 shows that depending on the simulation settings the results can significantly vary.

	HA-V2		HA-V3	
	Roe-FDS	AUSM	Roe-FDS	AUSM
$P_{gauge,E}$	3759	3705	3790	3757
$P_{gauge,out}$	3522	3575	3537	3567
Difference:	237	130	253	190

Table C.2: Gauge pressure values at the entrance and compressor where two designs have been compared with respect to the mentioned solver settings.

D

Explanatory Figures

D.1. Propeller Surface

Figure D.1 shows the definition of the propeller surface. 25 % of the propeller surface is considered for the contours & calculations in Chapter 5.

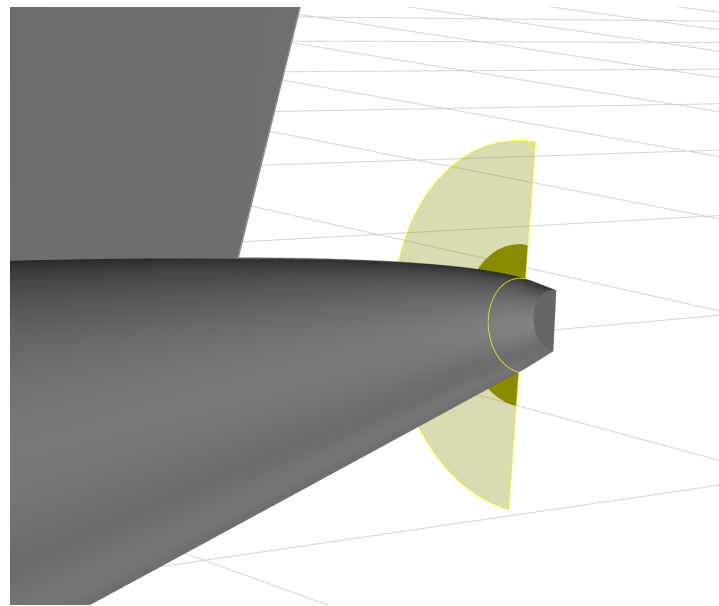


Figure D.1: The light yellow region is the actual size of the propeller (assuming that the APPU propeller size has not been adjusted during the course of the thesis), whereas the dark yellow region is the surface that is considered in this study.

D.2. Sign Convention

At the domain inlet, the flow experiences a pressure and momentum term in downstream direction (positive X) as energy is exerted by the engine on the flow, whereas at the domain outlet (or: compressor face), the pressure and momentum terms point in upstream direction. Note that the figure below shows the forces that act **on the air**. Therefore, the forces acting on the aircraft components are equal to but opposite in sign. In this case, where the vector points out of the domain, the normal vector causes the sign switch.

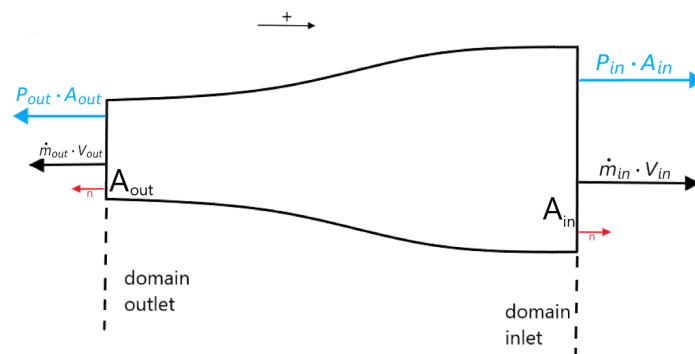


Figure D.2: Adapted from [56]

D.3. Boundary Layer Thickness

Figure D.3 shows the edge of the boundary layer at $X = 43m$, which is slightly upstream of the intake, where the local total pressure is equal to 99% of the freestream total pressure. The thickness of the boundary layer was calculated by averaging the distance of this edge to the fuselage surface. To do so, the data points inside the wake of the vertical tailplane were first removed. Figure D.3 also shows the line at which the Mach number is 99% of freestream. The boundary layer thickness is commonly defined at 99% of the free-stream velocity, but the figure illustrates a vast difference compared to P_t , because a pressure recovery takes place at the tailcone. Therefore, it is more sound to use P_t instead.

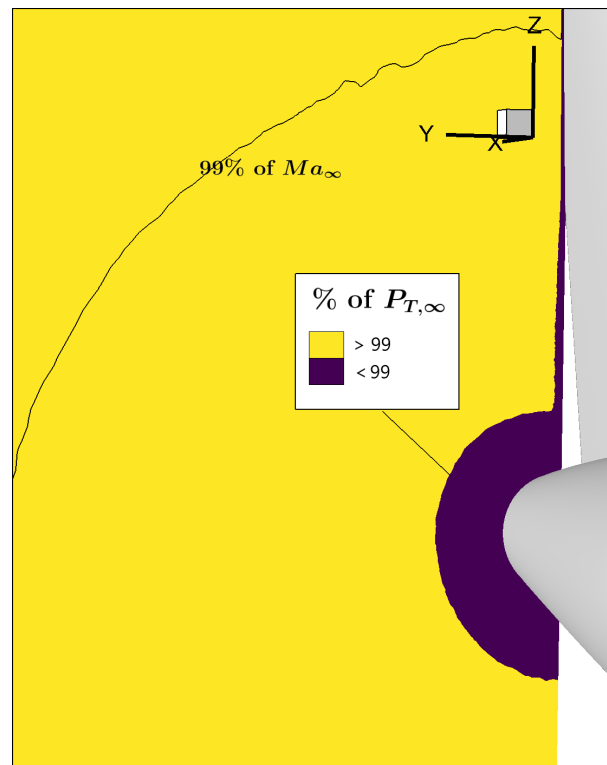


Figure D.3: Boundary layer edge

D.4. Lip Shape

Figure D.4 shows the curvature combs of the different lip shapes. The red comb represents the lip itself, whereas the blue combs depict the duct splines.

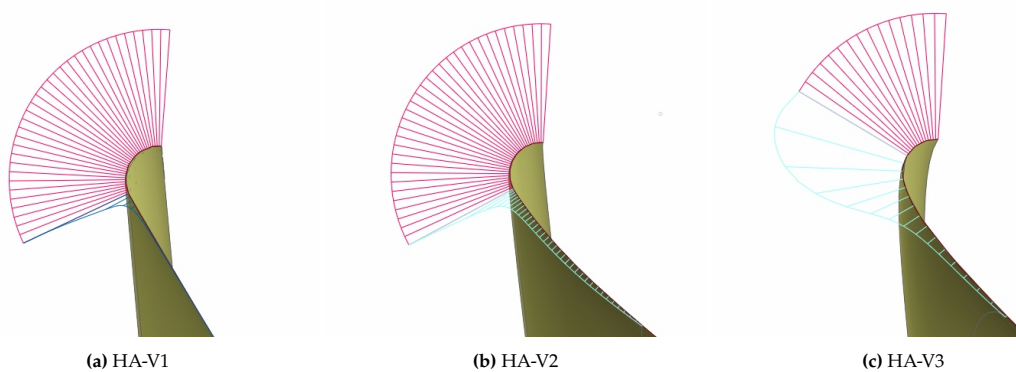


Figure D.4: Figures are out-of-scale with respect to each other.

E

Supplementary Contours

E.1. Contours at Cruise Boundary Layer Profile

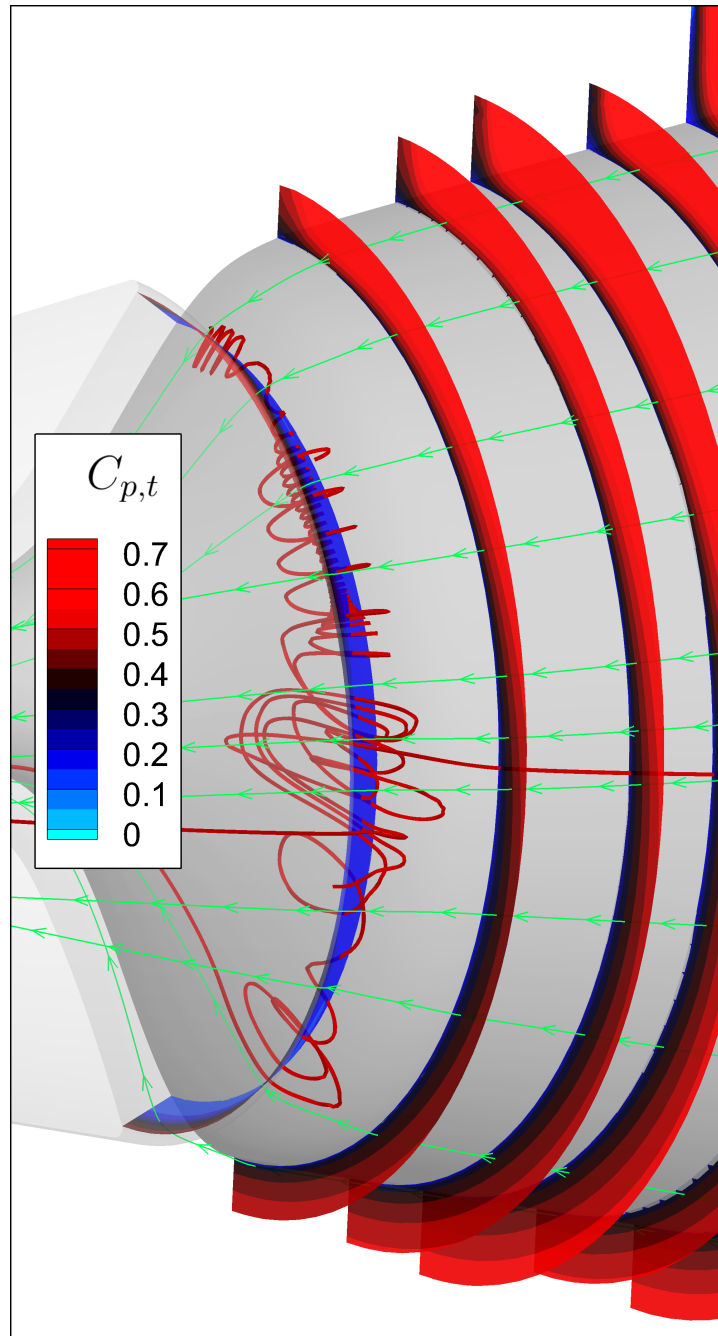


Figure E.1: $C_{p,t}$ contours for FA-V1.

vertical tail

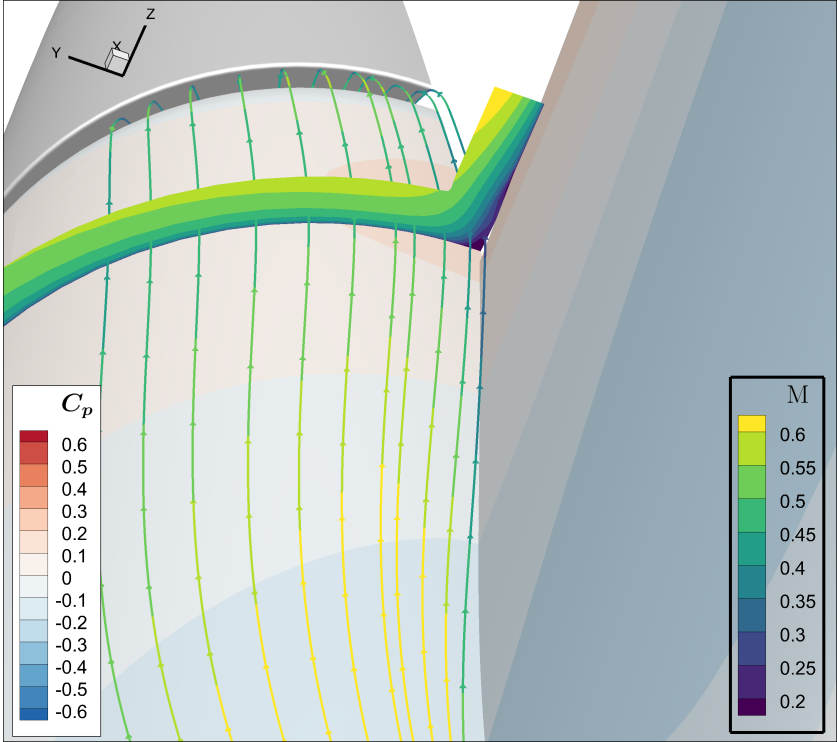


Figure E.2: Solution file of FA-V3.

Corner

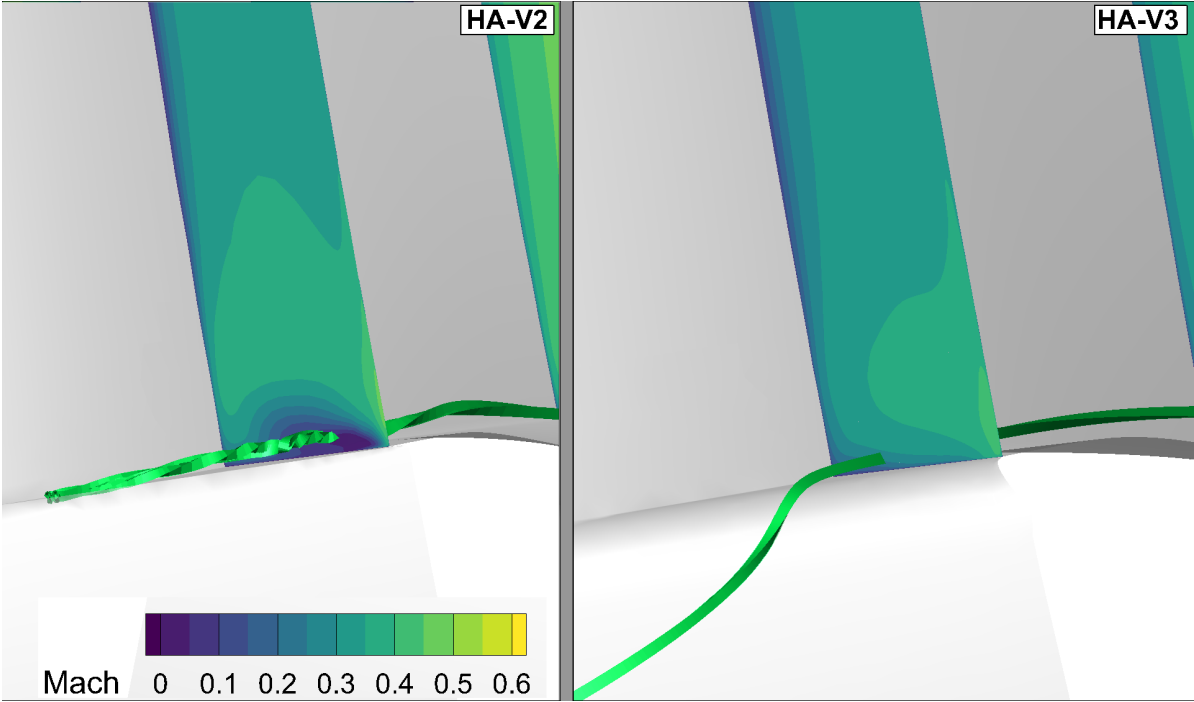


Figure E.3: Vortex formation at corner

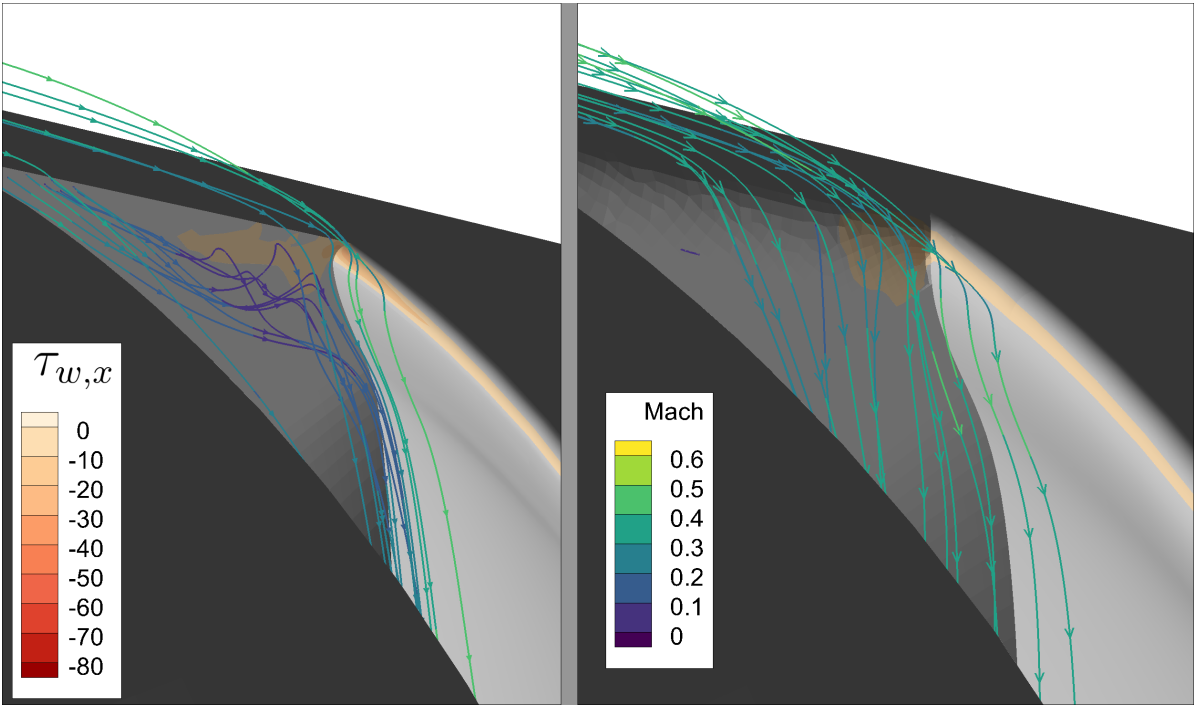


Figure E.4: Vortex formation at corner view II

E.2. Contours at SLS

Corner

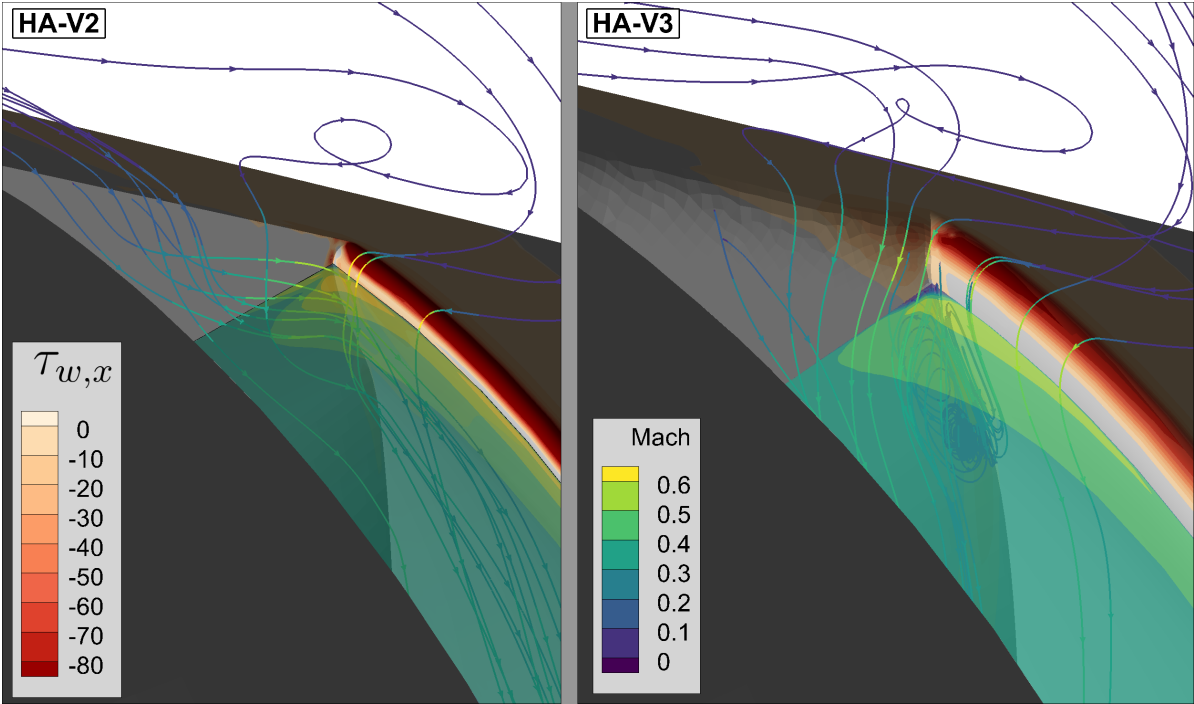


Figure E.5: Vortex formation at corner at SLS

Azimuthal Extent

Figure E.6 confirms that the total pressure ingestion is higher for the HA design.

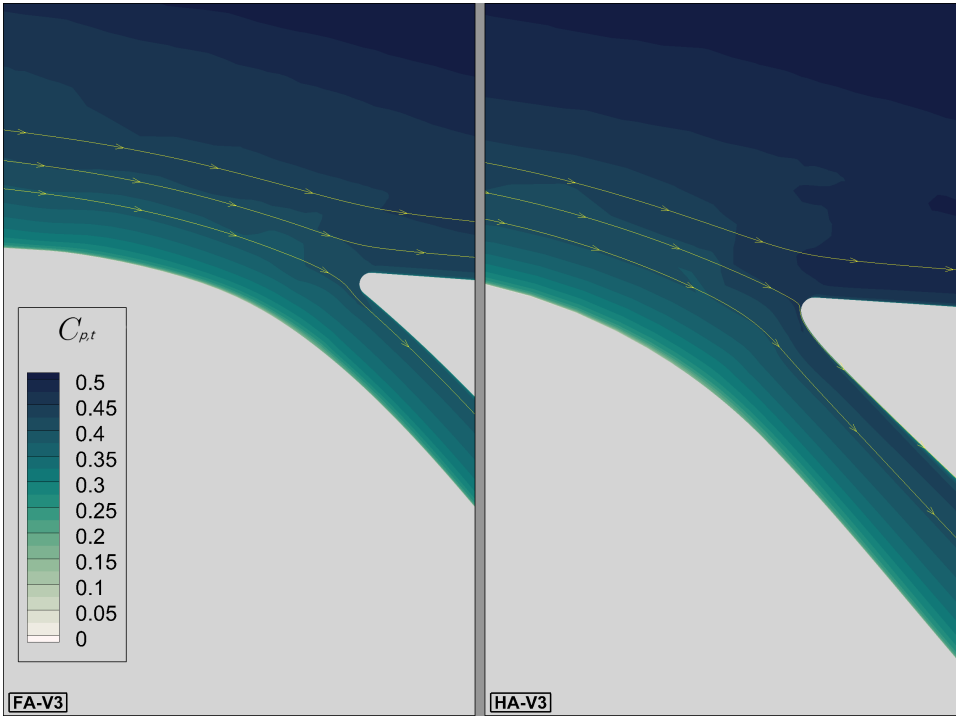


Figure E.6

Figure E.7 shows a comparison with HA-V1, where the intake length is similar to that of FA-V3.

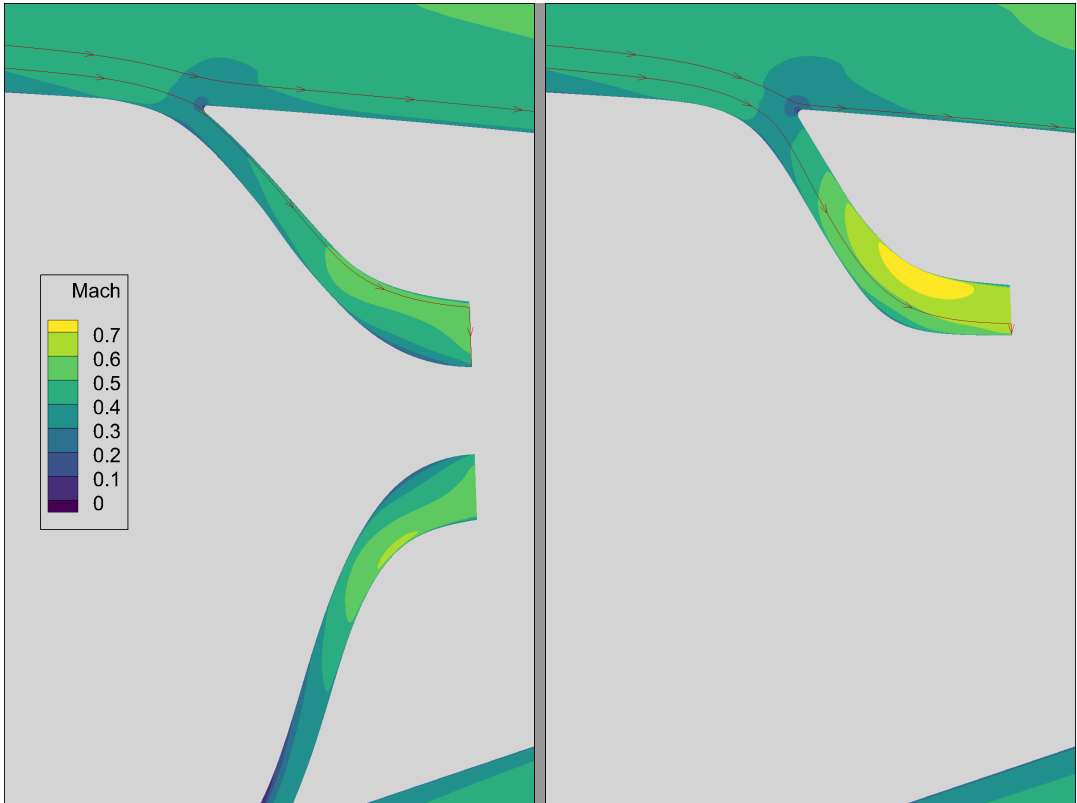


Figure E.7

Duct

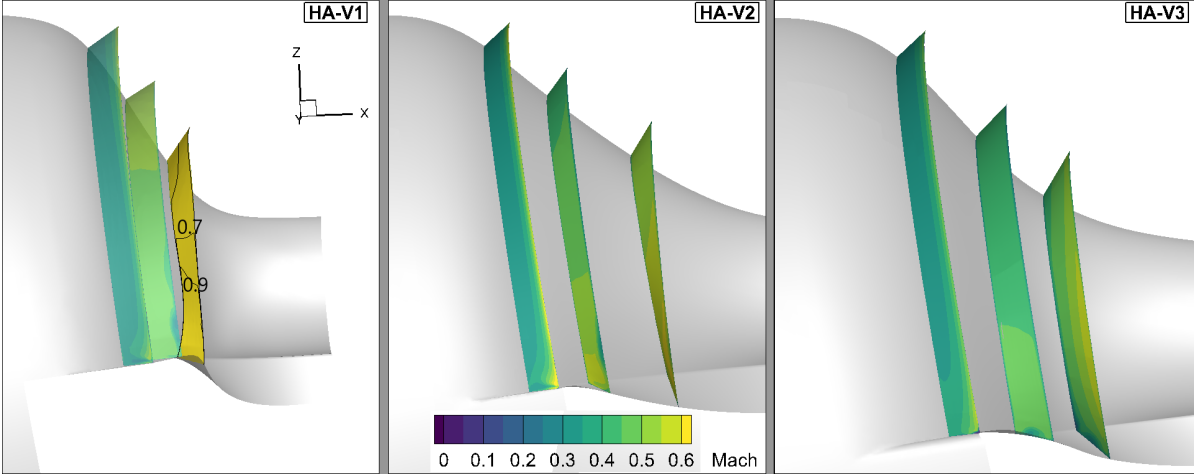


Figure E.8

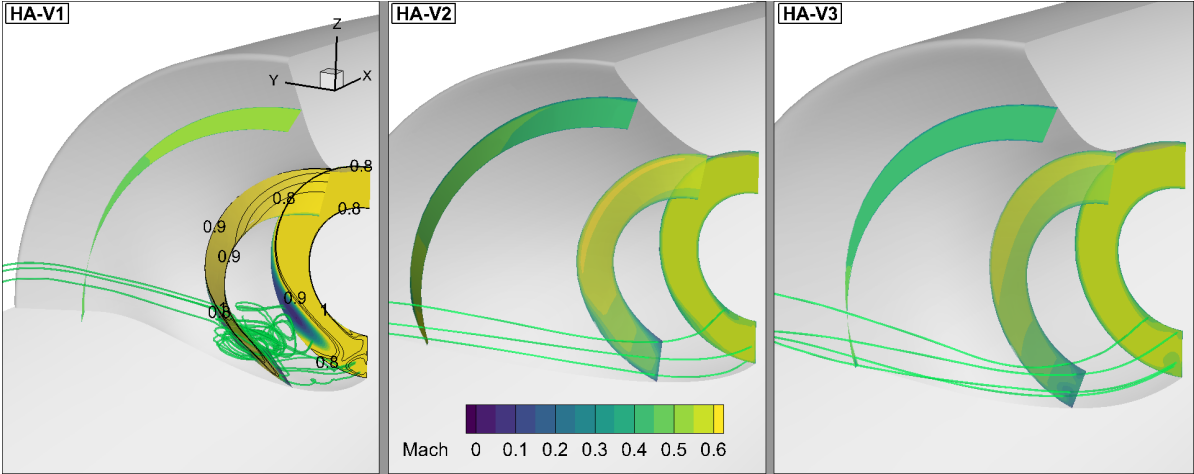


Figure E.9

Compressor face

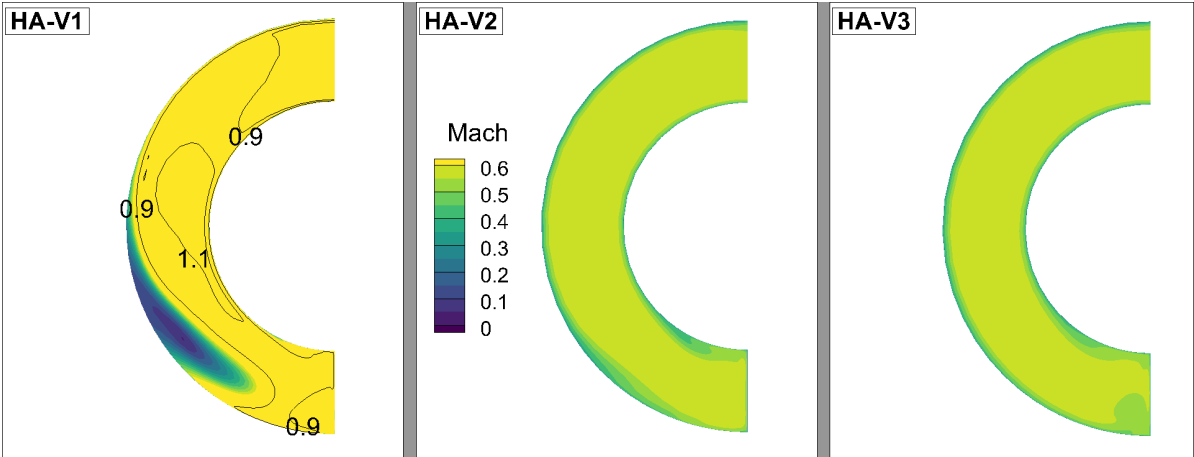


Figure E.10: Total pressure contours at the compressor surface